UNIVERSITAT DE BARCELONA

# Dynamics and Effective Connectivity in Bi- and Three–dimensional Neuronal Cultures: from Self–organization to Engineering

Estefanía Estévez Priego

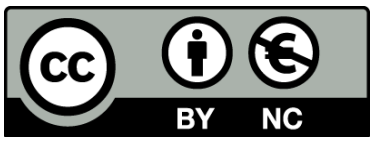

# Dynamics and Effective Connectivity in Bi- and Three–dimensional Neuronal Cultures: from Self–organization to Engineering


UNIVERSITAT DE BARCELONA

**Estefanía Estévez Priego**

Departament de Física de la Matèria Condensada

PhD Advisors

**Jordi Soriano, Daniel Tornero**

Tutor

**Giancarlo Franzese**

*Programa de Doctorat en Física*

Facultat de Física October 2019

A mis padres, que son maravillosos.

*”Don’t let anyone rob you of your imagination,*
*your creativity, or your curiosity.”*
Mae Jemison

# Acknowledgements

The last three years have been so intense that I hardly believe this Thesis is coming to an end. First of all, I would like to thank my supervisors for their immense patience and support. Gracias, Jordi, por confiar en mi, por ser un referente como profesional que se implica al 100% en todo lo que se propone y por contagiarme de tu inagotable positividad. Necesitaría un libro solo para agradecerte todo lo que me has ayudado con este trabajo y todo lo que me has enseñado. Me quedo con ese mensaje de Whatsapp en un momento de mucho agobio 'OK, pero tranquila, también descansa y sé feliz'. Y gracias a ti, Dani, por haberte volcado en este proyecto sin pensártelo dos veces. Me has enseñado más de lo que me creía capaz de hacer en el laboratorio y me has corregido siempre con una sonrisa. Estoy tremendamente agradecida de haber podido trabajar con vosotros. ¡Tendremos que repetir!

Tampoco hubiera sido lo mismo sin mis compañeros, que no sólo me han ayudado a mantener el laboratorio a flote si no que se han convertido en grandes amigos. Sara, me ayudaste desde el principio ya fuese en el ámbito laboral o personal. Recuerdo nuestros debates tanto filosóficos como de redes con inmenso cariño. Te admiro por tu constancia, por cómo buscas sobrepasar tus límites y por tu buen corazón.

Lluís, eres un máquina. Gracias por esas conversaciones sobre cualquier tema por aleatorio que fuese. Me dejaste leer tus historias de ciencia ficción y me ayudaste con cada pregunta de funciones y estadística. No te agradezco que me asustaras para que se me cayeran los *coverslips* pero sí por las risas.

Marc, este último año y medio me has salvado de la soledad en el laboratorio. Gracias por todas tus divertidas anécdotas, por el *super teamwork* que hemos tenido y los mensajes de buenos días en la pizarra. Eres tan buena persona y tan luchador incluso en los momentos más difíciles, que no tengo ninguna duda de que conseguirás todo lo que te propongas.

Giulia, eres un ejemplo de trabajo duro y simpatía, en qué parte del mundo nos encontraremos la próxima vez? Adriaan, I hope the best for you in Sweden, keep that insatiable curiosity of yours. También a Elisenda, que aunque hayamos coincidido durante menos tiempo siempre nos quedarán las cenas en casa de Jordi. A Javier Orlandi por toda tu ayuda con *netcal* y siempre hacer un huequito para echar una mano. Sin olvidar a aquellos que han pasado más brevemente por el lab como Ana, Clara, Gemma, Marc Duque, Silvia y Paul.

Gracias a los miembros de *El Oasis de Planta 7*, que con su buen humor y las comidas de verano en la terraza consiguen que la planta 7 sea un lugar más acogedor. Ojalá haber tenido más tiempo para acompañaros a tomar el vermut. Nico you are my best vecino, Núria que siempre tienes la solución a todos los problemas, Dani (del Ser), Alfred, Jose, Roger, Edgar... Pero quiero hacer una mención especial a Dani Pacheco, que durante todos estos años me ha provisto de buenos consejos, café y chocolate. Gracias por estar ahí y sacarme de vez en cuando del laboratorio, por decirme siempre lo bueno y lo malo. Wishing you and Angelica the best for this new stage and that we pay many visits to each other!

A todas las personas del Hospital Clínic que me han echado un cable durante estos años, especialmente a Mercè con tus buenos consejos y sinceridad, a Mireia por ayudarnos con los pedidos difíciles, eres la eficiencia personificada. Andrea, sufriste conmigo las primeras peleas con los *scaffolds* y la casualidad nos juntó en la SfN de San Diego, de donde guardo muchas buenas anécdotas. Espero que disfrutes mucho en Lund y que volvamos a echar una cerveza pronto. Gracias Sara (Fernandez) no solo por tus lecciones sobre

disecciones, si no sobretodo por los ánimos y la buena compañía. Desbordas energía allá donde vas, eres una crack.

Pero mi aventura en el mundo de las redes neuronales realmente comenzó cuando fui al CTB de Madrid buscando un trabajo de fin de máster centrado en neurociencia. La suerte quiso que me topara con vosotras, Irene e Imma. Me llevé un cachito de vuestra motivación, metodología de trabajo y la curiosidad de profundizar en este campo de las redes complejas. Recuerdo con cariño aquellos meses y me alegro de que nos hayamos podido reencontrar durante estos años. Álex, hemos coincidido pocas veces en el mismo sitio del mundo, pero hemos compartido el estrés de la última étapa y eso siempre une, espero que la próxima vez que nos reencontremos sea con más tiempo libre.

Y en esta red compleja destacáis Álex y Clara, con vuestra forma tan especial de ver los problemas desde nuevos puntos de vista. Las reuniones intensas pero llenas de buen rollo me dieron ese empujón cuando estaba atascada. Nos queda pendiente un paseo en lancha.

This Ph.D Thesis was part of the MESO BRAIN consortium, and I would like to thank all the members that have struggled with us trying our bests these years. Even though we knew the objective was quite ambitious, we never gave up and kept proposing new designs, new materials, new methods. Specially, Anastasia, when I was lost searching for these hydrogels stuff you gave me the starting piece and always tried to help me since then. I will add another special mention to you, James. You are such a hard worker, full of new ideas and above all a kind person. I hope the best for you and that you guys come visit Spain more often!

También forman parte de MESO BRAIN el grupo de ICFO: Ha hecho falta mucha coordinación para ajustar los experimentos al setup, ir optimizándolo paso a paso, y nunca habéis perdido la positividad ni las ganas. Pablo, te agradezco de corazón todos tus conejos, tu naturalidad y profesionalidad. Gustavo, cuántas horas habremos echado haciendo experimentos! Ha sido muy fácil trabajar contigo. Y gracias al resto del equipo: Laurent, Jesús,

Marina... que habéis aportado vuestro granito de arena. No sé si he hecho más viajes desde Física al Hospital Clínic o a ICFO, pero debe estar muy igualado.

No pueden faltar en esta lista ni en ninguna otra, porque ellos son los FCPM: David Carmona, David Díez, Álex, Gustavo, Adri, Dani (Forte), Germán y Xavi. Gracias por todos esos momentos en el Lens (que en paz descanse) que eran como vivir dentro de una *sitcom* americana. Germán, te fuiste a Canadá y me quedé sin *coach* para cantar, pero espero que algún día coincidamos para un dueto. Xavi, te conocí como Zell hace muchos años en aquel blog de relatos, pero en ese momento no sabía que llegaríamos a ser tan buenos amigos ni que vendría a tu ciudad para quedarme una larga temporada. Recuerdo aquella conversación cuando te dije que me mudaba a Barcelona. Gracias por haberme apoyado desde hace casi una década, por todas las risas, tienes un corazón enorme que no te cabe en el pecho. Gracias también a Josa, Martí, Sara, Massons, Sofi, Vera, Antón y Queralt. Gracias porque sin vosotros hubiera sido mucho más tedioso el camino.

He dejado un hueco para *La Piña*, que a pesar de habernos desperdigado por el mundo como las bolas de dragón al final encontramos la manera de juntarnos. Especialmente a mis piñones Almu, Irene y Paloma, gracias por venir a visitarme y apuntaros a cualquier plan aunque sea en medio del Atlántico.

A mis Telecos: Luis, Álvaro, Carmen, Juan, Mikel, Almu y Juanlu. Juanlu, tú has sufrido en mayor medida mis desahogos y mis alegrías. No ha sido una época fácil para ninguno en algunos momentos, y estoy muy agradecida de tenerte cerca. Almu, minina, estoy super orgullosa de ti. Gracias por arrancarme siempre una sonrisa y animarme. Te echo de menos.

Gracias a los que desde siempre estáis ahí por muy difícil que sea la campaña: Fer, Luis y Richi. Puede que sin vosotros no hubiera llegado a estar aquí y me hubiera atascado por el camino. También a ti, Vane, que eres otro gran ejemplo de trabajo duro y optimismo. A Alberto y Dani, mis

queridos hobbits con los que pronto empieza una pequeña gran aventura, gracias porque sois dos pilares imprescindibles y grandísimas personas. Y a mi querida Mariángeles, que es la que más veces ha venido a visitarme a Barcelona. Sabes que eres una persona super especial, la persona más encantadora y brutalmente sincera que conozco, y fuiste quien me enseñó a pedir ayuda cuando lo necesitaba. Han pasado más de diez años y aun no nos acordamos de nuestros cumples, pero eso no es lo importante.

Guille, necesitaría otro libro para resumir todo lo que representas. Para empezar, me enviaste por sorpresa una Nesspreso nada más llegué a Barcelona porque 'la vas a necesitar'. En serio, eres de lo mejor que tengo.

Tengo que agradecer a muchísimas personas todo el cariño, el apoyo y los buenos momentos que han acompañado este trabajo (lo siento por los nombres que se me hayan olvidado!), pero si hay alguien que ha estado siempre al pie del cañón, eres tú, Gerard. Tu confianza y amor me han ayudado a llegar hasta el final con la cabeza sana. Me has escuchado ensayar una decena de veces, me esperabas despierto cuando mi avión llegaba tarde de un congreso y me has hecho ver el lado bueno de las cosas aun cuando todo parecía muy negro. Gracias por ser tan increíble. Me siento muy afortunada de haberte tenido a mi lado todo este tiempo.

Por último, quiero dar las gracias a mi familia. ¡Vaya temporada! Gracias por permanecer simpre unidos, por ser cariñosos, divertidos y atentos en los momentos buenos y en los no tan buenos. Tengo los mejores hermanos y hermana y unos sobrinos que quiero con locura. Papá, mamá, siempre me habéis apoyado en todo lo que hago y os habéis preocupado por mi, me habéis llevado a comer zamburiñas, me habéis recibido en cada visita con tortilla y despedido con un tupper de croquetas, si eso no es amor nada lo es. Sois mi ejemplo a seguir, porque sois increíblemente trabajadores, honestos y desprendéis luz. Sois hogar.

Gracias a todos por estar ahí.

# Table of contents

*"Sinuhe, my friend, we have been born into strange times. Everything is melting –changing its shape– like clay on a potter's wheel. Dress is changing, words, customs are changing, and people no longer believe in the gods –though they may fear them. Sinuhe, my friend, perhaps we were born to see the sunset of the world, for the world is already old."*

–Mika Waltari, *The Egyptian* (1954).

# Chapter 1

# Introduction

## 1.1 The Amazing Brain

The brain is considered the most complex system in nature. Like a coordinated orchestra playing sophisticated symphonies, neurons —the fundamental constituents of the brain— perform intricate compositions that result in our consciousness and movement. They are responsible for processing the information extracted from sensory receptors and encoded in rhythmic activity. Some of the main tasks shaped by neuronal activity include the storage, retrieval and updating of coded information to comprehend the world, evoke memory, and drive actions. However, the rules governing these processes and their underlying dynamical organization are yet not fully understood.

Historically, humankind has been fascinated and inspired to unveil the complex functionality of the brain. This curiosity eventually led to the conception of neuroscience. The birth of modern neuroscience can be ascribed to a Spanish neuroanatomist born in the 1800s, whose discoveries proved that neurons were the building blocks of the central nervous system (CNS). Santiago Ramon y Cajal loved drawing, and at a time when microscopes did not include cameras (Figure 1.1), his freehand sketches of individual nerve

cells (Figure 1.2), observed through a silver staining technique developed by Camilo Golgi, gave them the Nobel Price of medicine in 1906.

Neuroscience has advanced insatiably along the last century. Now we have high performance scientific cameras adapted to super resolution microscopes, combined with bioengineering techniques that could be considered fiction not so long ago, and yet we still know so little about the machinery that drives our every move and thought. The reason is that neuroscience is a broad and entangled field with some essential gaps of knowledge, which sometimes imply working with loose ends and flimsy assumptions.

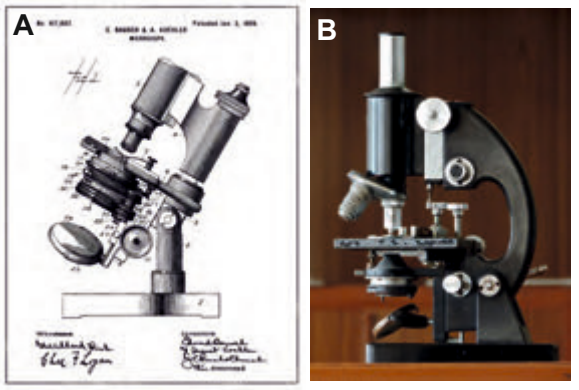


**Fig. 1.1 A piece of cell microscopy history.** (**A**) Bausch and Koehler's microscope patent from 1899. Koehler advances in sample illumination techniques are still considered the foundation of some modern methods such as confocal and phase–contrast microscopy. (**B**) Picture of an old microscope. The image is under the Universal Public Domain.

The cautious characterization of neuronal networks, functionally active, aims to fill in the blanks with respect to the development of effective connectivity, the plasticity mechanisms that emerge in response to perturbations, and the observable differences between cultures on bidimensional flat surfaces and tridimensional tissue, among others. These studies are helping us to build a solid foundation to establish models of neurodegenerative diseases, to better understand the effects of drug screening, and lately to grow reliable cell populations that could be systematically applied in clinical therapies.


**Fig. 1.2 S. Ramón y Cajal drawing of cortical neurons.** Some of the original drawings, known as *The Cajal Legacy*, are housed at the Cajal Institute (CSIC) in Madrid, Spain. Other examples with full descriptions can be consulted in Ramón y Cajal books (Ramon y Cajal, 1899)

### 1.1.1 The mammalian cerebral cortex

The cerebral cortex corresponds to the outer layer of the cerebrum, formed of folded and wrinkled gray matter $2-4$ mm thick. In humans and other mammals, the cortex is separated into two hemispheres by the longitudinal fissure, and the cranial suture lines divide it into lobes with distinct functionality: frontal, parietal, occipital and temporal. The cortex broadly operates as a data collector and interpreter of sensory information, being responsible of high–order functions such as cognition and motor output control.

The cortex contains $10-20$ billion neurons (S. von Bartheld et al., 2016) neatly organized in six–layered columns, enumerated I–IV from the outside inwards, with histological differences and characteristic connectivity paths among layers and other regions (Greig et al., 2013; Mountcastle, 1997). Through evolution, neuronal circuitry have grown remarkably in size and complexity, generating such diversity of cellular types in the neocortex that their full profiling and classification remains incomplete. Roughly, neurons are essentially sorted by excitatory pyramidal (or projection) neurons, being those the vast majority, and inhibitory cortical interneurons locally connected within the neocortex (Lodato and Arlotta, 2015).

During development, the brain builds a connectivity realm ruled by sophisticated dynamics that ensure proper overall performance. The malfunction or deterioration of these connections fosters the emergence of neurological disorders (Palop and Mucke, 2016). Incidentally, many diseases are closely related to abnormalities in the cerebral cortex that translate into cognitive or motor deficits, hence the importance of comprehending how cortical neuronal circuits shape healthy functionality, active regulatory mechanisms and, even more importantly, how a cascade of damage leads to system failure.

In this regard, animal models are fundamental to study neuronal dynamics during development, maturation and disease. In particular, rodents (mice and rats) have been the most examined species in neuroscience research, improving our knowledge of many biological processes, specially given the

lack of accessible human tissue. Rodents have some genetic and physiological similarities to humans and they have been extensively used to phenocopy neuronal diseases both *in vivo* and *in vitro*, to a certain extent, by applying neurotoxins that replicate pathological symptoms (Dawson Ted M., 2018).

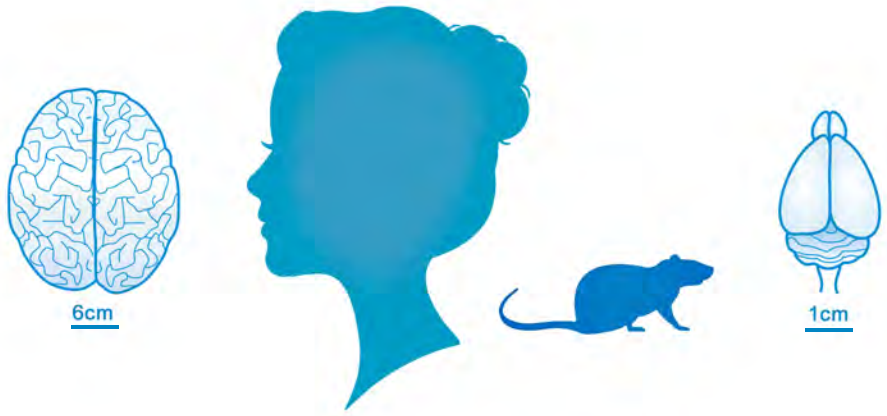


**Fig. 1.3 The mammalian brain: humans and rodents.** Illustration of the human brain and the rat brain, which at glance have differences in respect to size and form. For instance, the rat brain has very developed olfactory bulbs that protrude ahead of the rest of the brain and the cortex surface is smooth unlike the human brain.

As a word of caution, the rat brain is smaller than human's, the cortex is smooth instead of wrinkled (Figure 1.3) and, in spite of being organized in columns, the thickness of the layers and the number of neurons varies considerably (DeFelipe, 2011). Although during corticogenesis key events seem consistent between humans and rodents, the timing of cell expansion and neuronal maturation also differ across species, being the generation of induced cortical neurons *in vitro* at least forty times slower in humans than in rodents (Espuny-Camacho et al., 2013; Semple et al., 2013). Human pyramidal cells are also anatomically different from rodents, as they have unique membrane properties and larger number of dendritic spines —synapses— per cell (Deitcher et al., 2017; Eyal et al., 2016). Thus, despite the utility of

animal models, clear differences prevent the direct extrapolation of results between humans and rodents.

### 1.1.2 Neuronal activity and connectivity

Activity in the brain is characterized by rich spatiotemporal patterns that comprise diverse neuronal populations (from a few dozen to millions of neurons) and timescales (Blankenship and Feller, 2009; Deco et al., 2008). These patterns range from localized discharges in response to stimuli to brain–spanning spontaneous activations (Blankenship and Feller, 2009). Interestingly, spontaneous activity is very broad and much more structured than evoked activity. Widespread evidence points out that these activations do not correspond just to 'basal noise', but instead represent a fundamental mechanism for brain functioning. Spontaneous activity in the brain is often called *resting state* (Deco and Jirsa, 2012; Deco et al., 2010), and it is is believed to facilitate swift communication among brain areas, provide alertness, quick response to stimuli, continuous refinement and maintenance of neuronal circuits (Cohen and D'Esposito, 2016; Deco et al., 2010). Spontaneous activity is so important that its deterioration, for instance due to circuit damage (Fornito et al., 2015), causes broad motor and cognitive alterations, as occurs in Parkinson's, Alzheimer's and other diseases (Deco et al., 2010; Fox and Greicius, 2010; Seeley et al., 2009).

From a microscopic perspective, spontaneous activity is grounded on calcium transients. It has been observed in the neocortex since young embryonic stages (Corlew et al., 2004) and some studies argue that synchronized spontaneous activity precedes the onset of sensory experience (Kirwan et al., 2015). Precisely, neuronal activity influences important processes in early states of development such as differentiation, the establishment of short– and long–range connections, cell migration and synaptic plasticity (Gonzalez-Islas and Wenner, 2006; Luhmann et al., 2016; Shatz, 1990). An accepted intuition is that activity starts highly synchronized due to overconnectivity,

then undergoes a pruning or fine–tuning period (Martin M. Riccomagno, 2015; Peter R. Huttenlocher, 1997) and finally evolves towards more complex patterns with far–reaching propagation waves. Abnormalities during this period may cause chronic deficits.

In terms of energy consumption, every spike has a high biochemical cost (Lennie, 2003), and thus dynamical patterns have to be optimized to balance energy and function. This means for instance that there is no need for the brain to have all its circuits permanently active. When necessary, the brain is able to operate as a whole unit (*integration*) or as a set of localized communities carrying out specialized tasks (*segregation*) interconnected by hubs (Sporns, 2013). This segregation–integration balance (Deco et al., 2015) is available at different scales, and it is believed that fast switching between integration and segregation regimes is central for optimal brain function. Additionally, the community assignment or *modularity* is often implied in network efficiency and allows faster adaptation to changes in environmental conditions (Meunier et al., 2010).

The diversity of activity patterns is also constrained by the anatomical wiring between neurons and the density of cells (Messé et al., 2014). The latter is an influencing factor that alters the degree of connectivity (Ivenshitz and Segal, 2010) and is an undeviating repercussion of the connectivity blueprint that sustains functionality. The mapping of structural circuitry, the *connectome*, does not suffice to define the nonlinear, context–sensitive interactions in neuronal systems (Friston, 2011), but set up topological constraints that affect activity propagation (Haimovici et al., 2013; Messé et al., 2014; Sporns, 2011).

## 1.2 Neuronal Cultures Toolkit

About a century ago, neuroscientists proposed the idea of growing brain cells outside the body (Harrison, 1959) by dissociating neurons (typically from

rodents or invertebrates) and plate them on sterile surfaces where they could be maintained for weeks or even months, giving rise to the concept of *neuronal cultures*. Protocols for animal primary neuronal cultures have improved remarkably since then (Millet and Gillette, 2012), and recently this approach has been extended to human induced pluripotent stem cells, a biomedical technology that is revolutionizing our understanding of human brain circuits, neuronal development and disease (Kim and Vellis, 2009). In either case, the capacity of neurons to reconnect and, in a matter of days, exhibit robust spontaneous activity patterns, has fascinated both the neuroscience and the complex system communities (Mazzoni et al., 2007; Rolston et al., 2007). As such, neuronal cultures offer the possibility to explore the activity and connectivity of specific populations in a controlled environment.

### 1.2.1 Activity and effective connectivity in cultured networks

Although the detailed mechanisms that shape the initiation and maintenance of spontaneous activity are still unclear, there is a general consensus that it is driven by variations in the excitation–inhibition balance, neuronal noise, and an amplification effect through specific network pathways (Mazzoni et al., 2007; Orlandi et al., 2013), where every spike from a presynaptic neuron increases the firing probability of its neighbors, generating propagation waves (Wu et al., 2008).

In cultured networks, neuronal activity appears as discrete time series of action potentials on the millisecond timescale spaced by extended quiescent intervals. These repetitive activations emerge autonomously from self–organized neurons and conform spike trains or *bursts*. The interaction of individual spikes eventually gives rise to coordinated neuronal activations in the form of avalanches (Beggs and Plenz, 2003) or highly synchronous *network bursts* (Orlandi et al., 2013; Rolston et al., 2007). Indeed, these events of high neuronal participation or synchronization have been observed not only in culture (Orlandi et al., 2013; Rolston et al., 2007) but also in slide

preparations (Corlew et al., 2004) and *in vivo* (Leinekugel et al., 2002) at multiple frequency regimes.

Since it is clear that spontaneous activity and its diverse activity patterns are crucial for the operation of the brain, and by extension all living neuronal circuits, the uncovering of this activity characteristics and their changes along development or upon perturbation is an ongoing crusade holding the attention of the neuroscience community. An interesting way to define and represent spontaneous activity is to compute the *the functional* or *effective connectivity* (Friston, 2011), i.e. the map of interactions among firing neurons. Functional connectivity refers to a statistical relationships between the activity patterns of firing neurons ('who co–activated with who'), while effective connectivity refers to a casual relationship among firing neurons ('who activated who') (Friston, 2011; Vicente et al., 2011).

It must be noted that a rigorous analysis of spontaneous activity, functional/effective connectivity, and its intimate relation to brain's adequate functioning, started not long ago (Deco et al., 2008; Honey et al., 2009). Initially, spontaneous activity was thought to be a set of uncorrelated signals with no meaningful impact in brain's data processing, but during the past years we have seen how it has been recognized as a series of complex correlated spatiotemporal patterns that are absolutely crucial in self–organization of neuronal circuits (Lonardoni et al., 2017; Luhmann et al., 2016).

The relation between neuronal wiring structure and intrinsic neuronal dynamics is extremely tricky because of the complex interplay between cellular variability, noise and plasticity. However, recent advances have shown that, independently of the structure wiring, functional/effective connectivity in the brain maintains a series of key features, for instance well established communities (Power et al., 2011; Sporns and Betzel, 2015) and hubs (Sporns et al., 2007), and that their alteration reveal damage at a circuit level due to disease (Fornito et al., 2015).

In short, the different dynamics of cultures and brain proved that the functional/effective connectivity in neuronal networks, derived from activity patterns, is neither simple to compute nor totally identical among circuits (Muldoon et al., 2011). To comprehend it accurately, is necessary to analyze it from different perspectives and conditions. Neuronal cultures offer a perfect scenario for that, since one can explore different structural blueprints or actions (noise level, perturbations, physical damage) and their impact in the spontaneous activity and effective connectivity.

Nowadays, cultures are a complementary tool for brain research in multiple fields such as physics, computational neuroscience, biology and medicine. Neuronal cultures served to model the important role of noise (Orlandi et al., 2013) and network architecture (Okujeni and Egert, 2019) in shaping spontaneous dynamics, allowed to identify key molecular actors in diseases (Belle et al., 2018), and helped devising analytical tools to quantify functional and effective connectivity (Poli et al., 2015; Stetter et al., 2012). However, they failed to mimic some distinctive features that are lost in the absence of a tissue–like extracellular matrix (ECM). Thus, the next generation of cultures that we will witness this century will attempt to reconstruct the architecture of the brain by combining bi–dimensional (2D) and tri–dimensional (3D) organization through neuroengineering and advanced imaging techniques (D'Aiuto et al., 2018; Frega et al., 2014; Ko and Frampton, 2016).

## 1.3 Bioengineering in Neuroscience

Bioengineering is a merge of diverse *modus operandi* and expertise from different disciplines, betting on multidisciplinary approaches to address otherwise out–of–reach questions in fundamental biology. As stated before, neuroscience has been slowed down by the lack of specific technological resources, but in the last two decades we have witnessed breakthroughs as novel 3D printing techniques, advanced microscopy, innovative material science

and game–changing biological achievements. To name a few: genetically encoded calcium indicators (Chen et al., 2013) are replacing noxious fluorescence probes, neurons from human–derived pluripotent stem cells are now commercially available with well–establish protocols (Shi et al., 2012) and CRISP/Cas9 (Hsu et al., 2014) genetic editor which, despite being beyond the scope of this Thesis, is biotechnology's latest favorite toy.

In the present Thesis we delved into tissue engineering (Langer and Vacanti, 1993; Lanza et al., 2014), a concept defined since 1988 that refers to the restoration and maintenance of tissues damaged by disease, trauma or congenital disabilities (Eltom et al., 2019; Gregor et al., 2017). The term is sometimes interchangeable with 'regenerative medicine' because its most common application is tissue repair. However, the capability to mimic the natural extracellular matrix, combined with connectivity guidance to achieve higher–order structures, also serves as an improved *in vitro* model to develop explosive advances towards understanding network activity patterns in healthy and disease.

### 1.3.1 Neuronal tissue engineering

A major obstacle for the understanding of functional interactions in large neuronal populations is the inaccessibility of deep neuronal circuits inside the brain. In recent years, advances in tissue engineering has arose in response to this shortage, with the promise of creating new routines for the study of cell physiology and pathophysiology *in vitro*. In particular, 3D cell cultures provided the opportunity to study systems made from thousands of individuals inside a native–like environment, under controlled conditions. 3D neuronal cultures are a unique non–invasive tool for drug delivery (Ashley et al., 2013; Song et al., 2015), screening and resilience testing, with the possibility to seed different cell types to model both healthy and disease networks that resemble the *in vivo* natural behavior.

Some efforts making 3D models led to *organoids*, self–organized multicellular assemblies generated from stem cells, but the circuitry of these assemblies does not resemble the neuronal *in vivo* connectivity (de Souza, 2017). Other obstacles are the uncontrolled development of the organoids and the variability in cell types, which entails poor reproducibility (Silva et al., 2019). Also, same imaging limitations are found as *in vivo*, being necessary the use of slides to record functional activity (Pașca et al., 2015) or electrophysiology approaches (Quadrato et al., 2017) with less spatial resolution than calcium imaging techniques.

To achieve a homogeneously distributed 3D neuronal network, hydrogels appeared as a convenient solution. The brain is a soft, porous tissue composed of cells, fluids and extracellular matrix (ECM), and hydrogels are highly hydrated polymers that mimic that mixture. Common requirements consist of acquiring control over cell adhesion, viscoelasticity of the matrix, microporosity, the effect of growth factors and the degradation of the matrix (Griffith and Swartz, 2006). Some of the *in vivo* nerve ECM components are collagen, fibrin, hyaluronic acid and fibronectin. All have been tested and combined in several studies depending on their physical, biological and mass transport properties (Drury and Mooney, 2003). And that is not the end of the story. Natural hydrogels are also built in combination with synthetic materials including polymers, peptides or bioactive glasses, forming a semi-synthetic ECM where the mechanical properties of the biocompatible environment are meticulously adjusted.

Thus, brain tissue engineering serves to develop *in vitro* 3D neuronal cultures that achieve higher complexity levels and awake innovative applications in regenerative medicine, specially when allied with human–induced pluripotent stem cells (hiPSCs).

### 1.3.2 Guided self-organized neuronal circuits

As introduced before, neuroscience is still intrigued by the interplay between structural and effective connectivity (Schröter et al., 2017) as well as interested in the study of how the spatial arrangement of neurons influences activity patterns. To advance in these quests, the idea of imposing a neuronal circuitry layout through guidance of neurons and connections came under the spotlight and opened a new playground to evaluate changes in activity patterns in custom–made scenarios (Wheeler and Brewer, 2010). The customization of neuronal networks mainly requires control over cell adhesion and morphogenesis, which is achieved by coating substrates with proper biochemistry as PLL (Poly-L-lysine) or laminin, proteins that promote anchorage of neurons on a variety of surfaces (Sun et al., 2012).

In studies centered on the effect of cell distribution through coating substrates, it was observed that spatial inhomogeneity enhances connectivity and metric correlations among nearby neurons (Hernández-Navarro et al., 2017; Tibau Martorell et al., 2018); and that neuronal aggregates, formed in the absence of adhesive proteins, show distinctive modularity traits in comparison with homogeneously distributed cells (Teller et al., 2014). Chemical substrates have also been widely used to guide cellular attachment through different methodologies, mostly based on soft lithography (Kleinfeld et al., 1988) or microfluidics (Chiu et al., 2000). Experiments in patterned *in vitro* platforms demonstrated that micro–fabricated patterns were able to alter the integration–segregation balance in a modular neuronal network (Yamamoto et al., 2018). Microfabrication was also successful in establishing neuronal density gradients and even provided promising resources for modeling neurological disorders on–a–chip (Yi et al., 2015). Even though we are far from reaching finely tuned activity customization, these results showed that activity regimes can be altered by imposing specific geometries to the neuronal network. Hence, why not try it in an environment more similar to *in vivo*, such as in 3D?

Unlike other tissues as bone, brain's capability to self–repair is highly limited. Recreating specific configurations of human neurons on sophisticated 3D nano– and micro–structures, termed *scaffolds*, may serve as both a template for tissue repair and a biologically relevant model. The 'scaffold' concept as a supportive structure must fulfill a long list of requirements, which include cell compatibility, high porosity, good adhesion and sufficient mechanical support (Eltom et al., 2019; O'Brien, 2011). Latest biofabrication techniques allow precise control of pore size and geometry complexity through rapid prototyping, a process to generate layered structures using computer–aided design (CAD) and equipment (Lam et al., 2002). Some examples are 2–photon Polymerization (2PP) (Koroleva et al., 2012), a technique that sculpts the photosensitive material with laser pulses, and 3D bioprinting (3DP) (An et al., 2015) that can be direct (Hutmacher et al., 2001) or indirect using negative molds (Tan et al., 2013). The optimal technique balances precision, automatic manufacturing and adequate process times, as the fabrication of nanometric objects may take from hours to days. The availability of shaping 3D solid, biodegradable structures designed by computer software draws the imagination of researches in the field. We, in particular, aimed to advance towards the construction of 3D human cortical columns *in vitro*.

## 1.4 Outlook of the Present Thesis

This thesis was part of the European consortium MESOBRAIN, a team of 5 organizations that joined efforts in nanofabrication, cell culturing, imaging and data analysis to build tailored human 3D networks. The thesis timing was limited to 3 years, and several of the resources needed for its development were built from scratch. Despite the excitement of challenging such a tall order, the time limitation of the project carried enormous pressure and implied the search for original and quick solutions to solve non–trivial problems. The exploration of contingency plans was a constant, and several beautiful but

overambitious ideas simply did not work out. This thesis presents a good number of successes and 'plan B' rewards, but many efforts that unfortunately reached a dead end have been left behind.

The main objective of this Ph.D. thesis was to explore complex characteristics of cortical neuronal cultures in terms of effective connectivity and exhaustive network analyses. This objective comprised four research lines: (*i*) The evaluation of neuronal network resilience and emerging plasticity mechanisms, (*ii*) the characterization of functional development to underline crucial timepoints in healthy neuronal networks, (*iii*) the study of 3D network interactions of neurons embedded inside an ECM–like environment, and (*iv*) the design, construction and viability inspection of neurons seeded on tiny 3D nanoprinted solid scaffold structures as a first step towards recreating cortical columns *in vitro*.

For these multiple lines, we used either primary rat cultures (*i, iii, iv*) or human–derived neurons (*ii*). The former group corresponds to cultures with long established protocols that have been thoroughly studied in the field. The latter group corresponds to human neurons derived from iPSCs, a relatively novel model with promising and thrilling applications in regenerative medicine. Despite the increasing use of stem cells in neuroscience, complex systems and medicine, they still lack a thorough exploration in terms of neuronal and circuit formation as well as the properties of the emergent activity patterns.

With either primary or stem cells, we explored the formation of neuronal circuits in 2D and 3D, characterized the effective connectivity and rendered a number of network traits. This Thesis combines experiments of highly difficult implementation with detailed data analysis. For this reason, the exposition of the achievements in the different research lines is preceded by a description of the different protocols and tools used, both experimentally and numerically.

The Thesis is organized as follows. Chapter 2 describes all experimental protocols for culturing rat primary or human stem cells (hiPSCs) in 2D or 3D environments. Chapter 3 describes the numerical protocols for data analysis and network characterization. Chapter 4 describes the resilience experiments on primary clustered neuronal cultures perturbed through chemical action. This study represents an inspiring numerical–experimental model to comprehend the impact of plasticity mechanisms in the spontaneous activity of neuronal circuits. Chapter 5 outlines the engineering efforts within the MESOBRAIN consortium, the European adventure to build 3D neuronal cultures embedded in hydrogels and with the presence of scaffolds. Chapter 6 describes our successes with neuronal networks derived from hiPSCs, in which we were able to follow —and characterize through network theory— 8 different networks along 2 months, shaping one of the most detailed analysis of hiPSCs up to date. Chapter 7 describes some of the successes in our engineering efforts, focusing on the dynamics of 3D primary neurons in hydrogels, and visualized through either wide–field fluorescence microscopy our light–sheet microscopy. Finally, Chapter 8 elaborates the main conclusions and take–home messages.

This project was supported by MESOBRAIN, a FET-OPEN program funded under H2020 of the European Commission, with grant agreement 713140. The project aimed to forward–looking collaborations between advanced multidisciplinary science and cutting–edge engineering for new future technologies.

# Chapter 2

# Experimental Procedures

Neuronal cultures are a celebrated experimental model system that facilitates the study of neuronal circuit dynamics at the mesoscale. Their applicability has been historically associated to the Physics of Complex Systems and Neuroscience, but in recent years neuronal cultures have also jumped into toxicology, drug screening and the investigation of central nervous system (CNS) disorders. Neuronal cultures, seen as *in vitro* models, provide a controlled, scaled–down and reproducible platform for the analysis of complex brain functions. The key asset of neuronal cultures is that they can be prepared in a wide spectrum of physical designs and biochemical environments, thus dictating their physiological development and effective configuration.

This Chapter aims to provide a detailed description of the methodologies and resources used in this Thesis, to facilitate the understanding of the lines of action along the research and corresponding results. The Chapter is organized as follows: First, we present the procedures for the preparation of *in vitro* neuronal cultures from rat primary cells (Section 2.1) and human cell lines (Section 2.2). Next, we describe the strategies for the construction of three–dimensional (3D) cultures (Section 2.3), and finally introduces the different imaging systems used to monitor neuronal activity (Section 2.5).

## 2.1 Rat Primary Cultures

Animal models, or *in vitro* preparations of their neurons, have been extensively used for the study of neurodegenerative diseases (Dawson Ted M., 2018) and neuronal functional development (Orlandi et al., 2013). Rodents' brain cells (typically mouse or rat) are the most common resort for cells in *in vitro* experiments given their low price, easy manipulation, fast formation of neuronal networks and quick maturation.

In this thesis we have considered primary neuronal cultures derived from rat embryonic cells. In brief, cortical tissue is extracted, brain cells mechanically dissociated by pipetting and finally seeded under controlled environmental conditions. Neurons at embryonic stages display relatively poor connectivity compared to adults. Neural projections (dendrites or axons) are not extensively developed, thereby the mechanical disruption onto single cells is relatively easy and less harmful. Additionally, embryonic cells are not fully differentiated and still maintain a limited capacity for proliferation, which enhances survival upon plating.

It is important to properly select the developmental stage of the embryos. Neurogenesis in rats commences around embryonic day 12 (E12), peaks around E15 when the formation of the cortex starts, and by E17 most cerebral cortical neurons are generated (Qian et al., 2000), although it will still develop during the first postnatal month. Given that the gestation period lasts 22 days, the optimal dissection is performed by E18–21. In our experiments we considered E19 embryos from Sprague–Dawley rats.

All procedures were approved by the Animal Experimentation Ethics Committee (CEEA) of the University of Barcelona, under order DMAH-5461, in accordance to the regulations of the Generalitat de Catalunya (Spain). The protocols for the preparation of these cultures are described in (Soriano et al., 2008; Teller et al., 2014) and detailed below.

### 2.1.1 Culture procedure

For the experiments, gestating female rats were bred at the animal farm at Pharmacy Faculty of the University of Barcelona. After being deceased with $CO_2$, the animal was rapidly transported to Soriano's Lab. As described in previous studies (Teller et al., 2015; Tibau et al., 2013) dissection was carried out in ice–cold L–15 medium (Gibco), enriched with 0.6% glucose and 0.5% gentamicin (Sigma–Aldrich) to prevent contamination and maintain a physiologically controlled pH during the dissection process.

The extracted brain cortices were isolated from the meninges, transferred to plating media (see Table 2.1) and dissociated mechanically by pipetting, first with a 1000 ml pipette until tissue was no longer visible, and second with a glass flame–polished Pasteur pipette of $\approx 50$ $\mu$m tip diameter. The cell suspension was diluted to reach a nominal density of $\approx 100,000$ cells/ml. Final suspension was plated on ø13 mm glass coverslips placed on a 24–well plate. Each well contained 1 ml of cell–suspended solution. The density after seeding was around $200-400$ neurons/mm$^2$, and indicates a survival rate of $25-50$% of plated neurons.

**Table 2.1 Primary cultures media**

| Medium | Products |
|---|---|
| MEM+3G | MEM, 1% glutamax, 4% glucose, 0.4% gentamicine |
| Plating Media | MEM+3G, 5% Fetal Bovine Serum 5% Horse Serum, 0.1% B27 |
| Changing Media | MEM+3G, 0.5% Uridine 0.5% FUDR, 10% Horse Serum |
| Final Media | MEM+3G, 10% Horse Serum |
| Recording Solution | 500mL DDW, 128mM NaCl 45mM sucrose, 10mM glucose 1mM CaCl2, 0.01M Hepes |

Glass coverslips (Marienfeld-Superior) were cleaned one day prior to dissection. Coverslips were submerged in nitric acid for 2h to eliminate any possible organic residues, then washed twice with double distilled water to recover a neutral pH, and submerged in 70% alcohol in an ultrasonic cleaner for 20 minutes to remove residual particles and bacteria. Once cleaned, covers were dried out by gentle flame application with a Bunsen and deposited in sterile 24 well plates.

Once neurons were ready for plating, one had to take into consideration the chemical properties of the substrate since they define the capacity of the neurons to move or to remain anchored at the surface. In this thesis we considered two types of cultures, namely *homogeneous* and *aggregated*, which are sketched in Figure 2.1B.

**HOMOGENEOUS PRIMARY CULTURES. —** They were characterized by a uniform spatial distribution of neuronal bodies (somas), which relies on the attachment capability of the cells. The glycoproteins and glycolipids of the nerve cell membrane are fundamental for cell–to–cell recognition and interaction, but are also responsible for their negative surface charge. Given that coverslips are also negatively charged, to obtain cultures with a uniform distribution of neurons, glass covers were previously treated with a coating protein layer to enhance adhesion. Thus, we used Poly–L–Lysine (PLL, Sigma-Aldrich), a positively charged polymer, diluted at a 1:6 ratio in Borate Buffer (1M, pH 8.4).

**AGGREGATED PRIMARY CULTURES. —** They were characterized by highly clustered packs of neurons. Even *in vitro*, neurons exhibit complex migration mechanisms and may move few $\mu$m per hour (Cooper, 2013). We observed that, in the absence of adhesive proteins, neurons prefer to avoid contact with the non-coated surface and attach to each other, consequently forming aggregates of neurons and glia, named *clusters*, that remained size–stable from day *in vitro* (DIV) 4 onwards.

Within the first 24 hours after seeding, cells started to extend neural projections, and throughout the following days *in vitro* neurons rebuilt structural and functional connections, ultimately forming a complex network around DIV7. Cultures were incubated under the following conditions: 37ºC temperature, 5% $CO_2$ and 95% humidity in plating cell medium. At DIV5, cultures were treated with 0.5% FUDR for 3 days to restrict glial proliferation. Afterwards, the cells were maintained with periodic medium renewal every three days, using MEM supplemented with 10% Horse Serum. All culture media were filtered and prepared in sterile conditions.

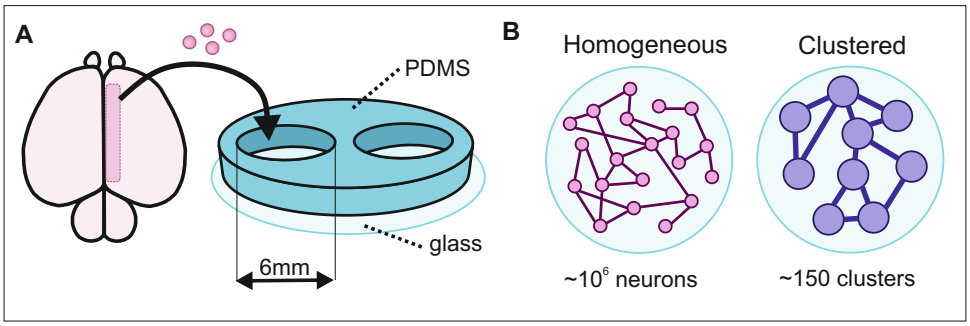


**Fig. 2.1 Rat primary culture** (**A**) Cortical neurons were suspended in plating medium and seeded on only-glass or PDMS-glass previously prepared PDMS–glass surfaces. Glass coverslips are 13 mm in diameter, PDMS molds contain 2 cavities of 6 mm in diameter each. (**B**) If coverslips were coated with and adhesive protein neurons remain homogeneously distributed through the surface (left), otherwise neurons tend to form aggregates of neurons and glia named *clusters* (right).

Exceptionally, for one study designed to evaluate the whole neuronal population under the limitations of our field of view (see Chapter 4), we attached a PDMS layer with two perforated cavities of 6 mm diameter onto the glass surface. The cavities effectually limited the area where neurons develop, providing two isolated cultures (see Figure 2.1) adjusted neatly in the field of view of our imaging system. Thus, the final setup provided two twin cultures, one for testing and the for control. Each culture contained

between 150 and 200 clusters that that remained size–stable from day *in vitro* 4 (DIV4) onwards.

### 2.1.2 Primary culture progress

During development, progenitor cells for neurons (neuroblasts) differentiate into neurons with mature morphology, extend axons and dendrites, establish synaptic connections and show functional activity. These cells naturally form cortical circuits that give rise to a population of combined excitatory (E) and inhibitory (I) neurons. This classification depends on the prevalent action on the charge of connected neurons, i.e. whether their membrane potential is increased (excitation) or decreased (inhibition). This capacity to carry out one action or the other is associated with the type of neurotransmitter the neurons release. It is a well–established statement that one neuron may co–release different neurotransmitters (Tritsch et al., 2016), refuting the ambiguous *Dale's principle* from 1954, so the truth is that E/I neuron categorization alone should be addressed carefully.

The main inhibitory transmitter in the brain, $\gamma$-aminobutyric acid (GABA), exhibits an excitatory action at early developmental stages, until there is a transition to its later inhibition role, known as *GABA-switch* (Bernard et al., 1989). Anomalies in the GABA switch timing are associated with cognitive impairments as functional maturation can be delayed. The switch of GABAergic–signaling is one of the drivers that modify the spontaneous activity in early neuronal development (Hayder Amin et al., 2017). Indeed, the balance between excitation and inhibition is extremely important during development and is an indicative of proper maturation. As stated in previous studies (Soriano et al., 2008), primary cortical cultures maintained a constant ratio of excitatory ($\simeq 80\%$) and inhibitory ($\simeq 20\%$) inputs, which arise respectively from pyramidal neurons and interneurons. We have observed that GABA switch occurs by DIV $5-6$ (Ganguly et al., 2001; Soriano et al., 2008; Tibau et al., 2013; Tibau Martorell et al., 2018). Provided that we performed

experiments at DIV $7-21$, we expected to solely observe a mature inhibitory action from interneurons.

The extracted cortical tissue also contains glioblasts, precursors of astrocytes and oligodendrocytes, also known as glial cells. The term glia derives from the Greek word for 'glue', and as the name suggests, these not electrically excitable cells embrace the neurons providing support and protection, enhancing culture viability (Dugan et al., 1995). Nowadays, glial cells have gained importance in also neuronal development, maturation and synaptic function (Durkee and Araque, 2019; Perea et al., 2009). Despite their many positive traits, there must be an appropriate balance between neurons and glia populations. As glia proliferates extensively for longer periods of time, we apply a DNA replication inhibitor (FUDR) after 5 days of incubation to limit glial growth. Otherwise they would consume all nutrients in the culture and compromise neuronal viability.

Henceforth, after glial control, half of the culture media was renewed every three days with just MEM (Minimum Essential Medium) and Horse Serum, a supplement that contains nutrients and growth factors for supporting neuronal health. Interconnected mature neurons displayed functional activity patterns by DIV7, the minimum time-point for our experiments, and their lifespan was around 3–4 weeks.

## 2.2 Human Cell Lines

The capacity to generate human neuronal cultures has attracted the scientific community for decades, since it would allow the study neuronal behavior, dynamics and network characteristics in conditions that approach those of the human brain. Ethical issues have prevented using human primary cells and embryonic stem cells. However, the establishment in 2006 of protocols for inducing pluripotent stem cells (PSCs) from mature tissue (Takahashi and Yamanaka, 2006) paved the way towards the preparation of human cultures,

both healthy and diseased, and boosted their study under a large number of conditions.

Stem cells are unspecialized cells capable of replicating themselves through cell division. The process consists on nuclear and cytoplasm division, followed by the formation of a new cell membrane. Additionally, PSCs have the ability to become any cell type of the body regardless of their origin. Well–established protocols to reprogram human somatic cells into PSCs have been set since the pioneering work of Yamanaka (Takahashi et al., 2007). Typically, four transcription factors are introduced into adult human fibroblast obtained from skin tissue, resulting in human–derived induced pluripotent stem cells (hiPSCs).

Despite their striking potential, the process of differentiating hiPSCs into specific cells, such as cortical neurons, is very delicate and time consuming. Here, we took advantage of commercially available human neural precursor cells (hNPC), which are hiPSCs partially differentiated into a neuronal phenotype, to speed up the experimental timeline and ensure comparable replicates.

### 2.2.1 Coating protocols

The best coating for cell–surface adhesion depends on substrate's material, the type of cells and the time scope of the experiments. For expansion, when the hNPCs are proliferating, we used 6–well plastic plates pre–coated overnight with 20 $\mu$l/ml Surebond solution (ax0041, Axol Bioscience). Once cleaned with PBS, the coated plates can be stored at 4°C for a few weeks. The size of each well is ø35mm and the working volume is in the range $1.5 - 3$ ml.

The final differentiation was performed in 'grid–glass' bottom petri dishes (ibidi, 81168). The size of the dish is ø35mm, the observation area is ø21mm and the working volume $1 - 2$ ml. The grid has 400 squares with an edge length of 500 $\mu$m, the lines of the grid have a $\leq 5\mu$m depth, which is undetectable for the neurons. Glass optical properties are better than plastic and

the grid allowed to track the same region of the culture, and practically the same cells, during their final stages of maturation.

The dishes for final differentiation were first treated overnight, at room temperature, with 0.1 mg/ml Poly-L-ornithine (Sigma P4957) diluted 1:5 in DDW. After one wash with PBS, we coated them with 5 $\mu$g/ml pH 4 laminin overnight at 37°C. To adjust the pH, laminin (Sigma, L2020) was previously diluted to a concentration of 50 $\mu$g/ml in a solution of 20 mM sodium acetate and 1 mM calcium chloride. Then, the excess of laminin was removed and the surface cleaned rapidly through 3 washes of PBS with pH 7, otherwise the acidity would damage the neurons. The coated surface covered with PBS can be stored at 4°C for one month. It is important to never let the laminin coated surface dry to avoid the lose of effectiveness.

### 2.2.2 Expansion and differentiation

Human iPSC–derived NPCs from healthy male newborn (ax0015, Axol Bioscience) were kept in liquid nitrogen at the Hospital Clinic for long–term storage. Vials containing $\sim$ 1.5 million neurons in 1 ml of freezing media were transferred in dry ice to the Faculty of Physics for culturing.

Cells were quickly thawed in warm Neuronal Expansion Media (ax0030, Axol Bioscience) and centrifuged during 5 minutes at 200xG. The cell pellet was resuspended in 4 ml of Neuronal Expansion Media, supplemented with 1:100 Penicillin-Streptomycin (100X, Gibco) to prevent contamination and 1:50 B27 (50X, Gibco) for survival support. To preserve the proliferative state, epidermal growth factor (SBEGF EGF beads, StemCultures) and fibroblast growth factor type 2 (SB500 FGF2 beads, StemCultures) were incorporated to the media. These agents are delivered as beads, with concentrations of 20 $\mu$l/ml of EGF and 8 $\mu$l/ml of FGF2. The beads guarantee a sustained release of both factors at a concentration of 10 ng/ml for 3 days. Cells were then seeded into wells (2ml/well) containing $\sim$ 750.000 cells each, incubated at 37°C, with 95% humidity and 5% $CO_2$.

After 3–4 days, depending on the proliferation speed, cells were detached with Unlock Solution (ax0044, Axol Bioscience) using 1ml/well by slow pipetting, transferred again to a centrifuge tube and spun during 5 minutes at 200xG. Unlock solution was removed without altering the pellet deposited at the bottom of the tube. Cells were then resuspended in 8 ml of fresh media and seeded in the remaining pre–coated wells (2 ml/well). This process is known as 'passaging'. We usually started the differentiation process at the second passage.

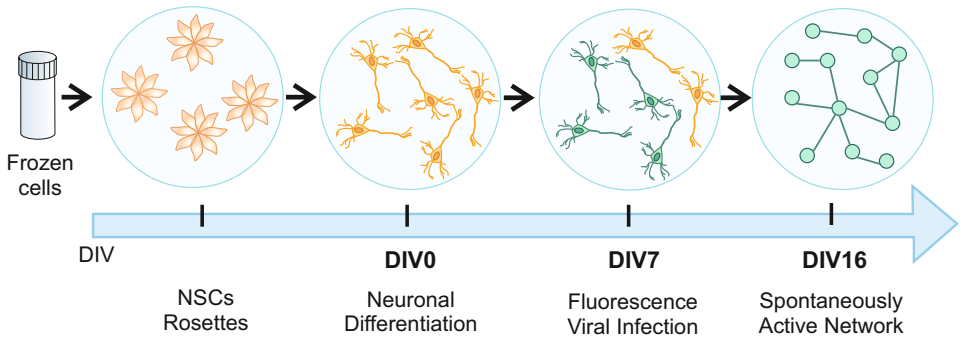


**Fig. 2.2 Human iPDC–derived NSCs culture steps** Culture protocol summarized from the unfreezing of hNSCs (rossettes) that are kept in proliferation during 1–2 weeks. Then the differentiation process starts and cells are specialized into cortical neurons (DIV0). At DIV7 cells are infected with AAV-GCaMP6s (neurons marked in green). Finally, around DIV16 the neuronal network displays spontaneous activity. Passaging steps were omitted.

Before the last passaging, cells were washed once with PBS to remove the remaining expansion beads with growth factors. Then cells were detached as described previously and seeded for final differentiation on bottom–glass coated petri dishes. One day later (DIV 1), media was switched to Neural Differentiation XF (ax0034, Axol Bioscience), and at DIV 4 to BrainPhys (StemCell, 05791), supplemented with 2% B27 and 1% penicillin-streptomycin, which was renewed every 3–4 days onwards.

One week after starting differentiation (DIV 7) cells were infected with the adeno-associated virus (AAV) containing the fluorescence indicator GCaMP6s

(1$\mu$l/ml), described in Section 2.5.2. Neurons started showing spontaneous activity around DIV 16. For the study of neuronal development and synchronization, identical areas of the cultures were followed up to DIV 57, which is the maximum timepoint that we were able to achieve. The culture timeline is summarized in Figure 2.2.

## 2.3 3D Cultures

The preparation of three–dimensional (3D) neuronal cultures provide physiological conditions closer to the brain and give the opportunity to design much complex architectures. In this set of experiments, we worked with our colleagues from the MESOBRAIN consortium in Laser–Zentrum Hannover, to build biocompatible layered scaffolds as a platform for our 3D cultures. We also handled hydrogels, loose scaffolds highly hydrophilic, and adapted an established protocol (Koroleva et al., 2016) to neuronal cells.

### 2.3.1 Hydrogels

Hydrogels are elastic, gelatinous structures made from cross–linked polymer chains. These biomaterials mimic the native extracellular matrix (ECM) of the brain, where cells are encapsulated. Hydrogel culturing maintain the advantages of *in vitro* cultures while advancing towards *in vivo* models. Overall, as shown in Chapter 7, we obtained a true 3D homogeneous distribution of self–organized cells. Incidentally, we must note that thin hydrogel layers are also used as a coating substrate for 2D cultures instead of glass or plastic surfaces due to the mentioned features (Caliari and Burdick, 2016).

There is a wide variety of hydrogels available for cell culturing, which can be classified as natural or synthetic depending on the source of their components. The common drawback of fully natural hydrogels is their low stiffness and limited long–term stability (Caliari and Burdick, 2016). Synthetic options allow for tunable stiffness, but display less compatibility, and unpredicted

physiological interactions with cells may alter experimental results. In this regard, we chose a semi–synthetic hydrogel, named *PEGylated fibrin*, to ensure biocompatibility while facilitating custom mechanical properties.

The 'PEGylated' part of the hydrogel derives from the concept of 'PEGylation', a bioconjugation process that consists on attaching polyethylene glycol (PEG) chains to other molecules, modifying their physiochemical properties. PEGylated molecules are more stable than their non-pegylated counterparts, with slower degradation and clearance rates. PEG is also biocompatible, non-toxic, inertness and soluble (Gianfranco and Francesco, 2005; J.M., 1992; Roberts et al., 2002). All these features are fundamental to ensure long–term culturing and physical manipulation (e.g. for transplantation), making PEG a truly wonder for bioengineering.

The 'fibrin' part of the hydrogel corresponds to an ECM protein that plays an important role during blood clotting after a vascular injury (Weisel and Litvinov, 2013). Two major end products of the coagulation cascade are fibrinogen and thrombin, a plasma glycoprotein synthesised in the liver and a serine protease, respectively. Crucially, the presence of thrombin enzymes converts the *soluble* monomer fibrinogen into the *insoluble* monomer fibrin by polypeptide cleavage. Along this process, fibrin strands are covalently crosslinked to create a mesh, an insoluble gel (Arulmoli et al., 2016).

The combination of PEG and fibrin provides a stable, jelly–like hydrogel media where neurons grow. This final hydrogel is prepared as follows. The main reagents are prepared in advance in sterile conditions. Fibrinogen (F8630-1G Sigma) is gradually dissolved to a concentration of 25 mg/ml in warm PBS. The process must be progressive to avoid bubbles and lumps, and therefore may take several hours. Thrombin solution (T4648-1KU SIGMA) is dissolved in 10 ml of warm PBS to a concentration of 5U/ml. PEG–NHS solution (713783 SIGMA) is dissolved in PBS at 6 mg/ml and must be used within the following 24h to ensure its efficiency.

PEGylated Fibrinogen solution was prepared by combining 121 $\mu$l of PEG–NHS solution with 1ml Fibrinogen solution to obtain a molar ratio 5:1. This cocktail was then stored in the incubator at 37°C for 2h. Molar ratio can be increased to 10:1 for better stability but may difficult cell migration and connectivity.

Once the cells were dissociated, 400$\mu$l of cell media per well ($\sim$ 200.000 cells/ml) were mixed with 200$\mu$l of PEGylated Fibrinogen. For 0.2U/mg, equal quantities of PEGylated Fibrinogen (25 mg/ml) and Thrombin solution (5U/ml) were used. Gently pipetting of the final solution was required to ensure a homogeneous distribution of the cells within the volume. The jellification process was perceivable after a few minutes and was completed in less than 20 minutes. Hydrogels were placed on 24-well plates upon clean glass cover–slips, to provide structural support and facilitate handling.

For the study of functional connectivity in 3D cultured neuronal networks, the neurons were infected with GCaMP6s-AAV when dissociated and prior to jellify (Figure 2.3), procuring excellent results. Otherwise a perfusion system would be required to introduce the virus into the gel. Recordings of neuronal activity with hydrogels were performed between DIV7–DIV21. After 3–4 weeks, the hydrogel started to degrade, detaching from the walls of the well that contained it. When this occurred, neurons formed dense aggregates (clusters) connected to one another with thin straight connections and remained active for few more weeks. Therefore, long–term detailed development experiments were not possible, but neurons were healthy and highly active as shown in Chapter 7, and the morphology of both individual neurons and clusters was different from the sister 2D cultures.

### 2.3.2 2PP scaffolds

Two photon polymerization is a technology to fabricate precise 3D structures from a photosensitive material with a resolution of 100 nm. 2PP scaffold production was carried out in Laser Zentrum Hannover (Germany) (Koroleva

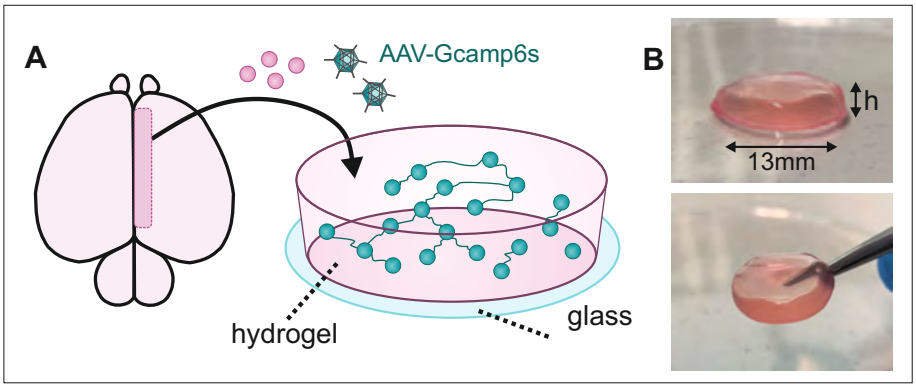


**Fig. 2.3 PEGylated Fibrinogen Hydrogel culture.** (**A**) Cortical neurons from rat embryo were suspended in cell medium, mixed with PEGylated Fibrinogen and GCaMP6s-AAV, and seeded on top of a ø13mm diameter coverslips on a well-plate. Then thrombin was quickly added, pipetted carefully a few times and left to jellify. (**B**) Picture of a hydrogel, stable after 3 weeks in culture. For 400µl of cell media, 200µl of PEGylated Fibrinogen and 200µl of Thrombin, the total volume once jellified is $V = 4mm^3$ and the height h=2.6mm. The glass facilitates its manipulation without damaging the cells embedded inside bottom image.

et al., 2012). There, a near–infrared femtosecond laser beam was focused on a volume of liquid material, previously treated with a photo initiator. The beam can be moved in three dimensions, following computer–generated designs, and curing the liquid in its path to shape a solid structure without affecting off–focus areas. Once the design was finished, it was washed with 4-methyl-2-pnetanone and 2-propanol to remove unpolymerized material.

A proper scaffold must fulfill some prerequisites regarding biocompatibility, optical properties for 3D imaging and usefulness for neuronal/axonal guidance.

Along the first year of the MESOBRAIN project, a substantial amount of time was invested in selecting the best material fulfilling these conditions. The first material selected was Polyethylene Glycol Diacrylate (PEG-DA). Although transparent, PEG-DA samples showed remarkable auto–fluorescence that made difficult the assessment of neuronal calcium levels. Photo–bleaching attempts to silence the fluorophore resulted in a transparency loss of the material and caused structural damage that lead to brittleness. The

solution was to change the photo initiator during the curing procedure to reduce this effect, using Irgacure 651 instead of Irgacure D-2959, but the outcome was still not optimal.

PEG-DA served for testing designs during the first part of the project. However, it was dethroned by a new material, Dental LT Clear, never used before for tissue engineering. This material is a commercially available photopolymer resin with good biocompatibility, very low or inexistent autofluorescence, and high cell–attachment efficacy.

Scaffolds were securely sent to the University of Barcelona, where they were sterilized by immersion in 2–propanol and exposed to ultraviolet germicidal irradiation for 20 minutes. Samples were then washed twice with PBS and coated with a positive charged protein. Successful coating solutions for long term attachment were Surebond (Axol Bioscience), Geltrex (Thermofischer), PLL-Matrigel (Sigma Aldrich) and PLO-Laminin (Sigma Aldrich).

Different designs were proposed and described in Chapter 5, with the aim to shape the best construction where neurons could developed in a tunable 3D network, and with the long–term vision of designing implants that could mimic an *in vivo* cortical column. The first approach in this endeavor consisted in periodic structures made of cylinders or squares, balancing the amount of attachable surface with the available space for media to flow easily, as well as ensuring that connections could grow through layers. Two designs with this premise gave promising results, namely a 3D mesh (*tower*) of periodic square shapes and a *honeycomb*-like assemblage of cylindrical arrays. The second approach was centered on stackable scaffolds, in such a way that neurons were cultured in separate scaffolds before attaching them together. A third approach, based on three–level stairs, was used to test the ability of neurons to be grown in different layers and connect vertically.

### 2.3.3 PDMS atterns

Silicone–based PDMS (Polydimethylsiloxane, Sylgard 184, Dow Corning) is a colorless, non–toxic synthetic polymer commonly used for biomedical applications. It is composed of a base liquid elastomer and a curing agent, that are mixed and whipped manually at a ratio 10(base):1(curing agent), then poured in plastic petri dishes. For actual curing, it can be left at room temperature overnight, or placed in an oven at 80°C during 90 minutes.

PDMS can be pierced easily for making molds, and allow fine patterning with a resolution between 30 nm and 500$\mu$m (Collins, 2012). In Soriano's Lab, patterns of PDMS were made from gold–printed topographical configurations on fiberglass, and using technology from electronics printed circuits (Circuitos Impresos 2CI, Barcelona), shaping top–bottom designs with a height of either 35 $\mu$m or 70 $\mu$m height. PDMS is also suitable for high–pressure sterilization (autoclave, 105°C). If placed on top of a clean glass, the high temperature will trigger a strong bond between glass and PDMS. Additionally, PDMS is appropriate for culturing and imaging due to its excellent thermal and light stability (Koroleva et al., 2012).

When preparing PDMS one has to be aware of the thickness of the material, and adjust it to the needs. The optimal thickness of the PDMS mold depends on the experimental conditions. In the context of PDMS molds used to restrict culture size, smaller and independent cultures are located into pierced holes. Therefore, the thickness of the polymer has to be enough to ensure the isolation of neurons from each culture, but thin enough to facilitate attachment and avoid floating. Typical experiments procured heights in the range $1 \leq h \leq 2$ mm. In contrast, in patterned molds where the culture is visualized with an inverted microscope, through the polymer, it is convenient to make the PDMS as thin as possible, in the range $80 \leq h \leq 500\mu$m.

## 2.4 Experimental Pharmacology

### 2.4.1 Receptor antagonists

Neurons communicate through the release of neurotransmitters, that can contribute to increase (excitation) or decrease (inhibition) the membrane potential. Each type of neurotransmitter freed from pre–synaptic neurons binds to specific receptors located in the plasmatic membrane of post–synaptic neurons, a process known as a key–lock mechanism. Receptor antagonists are chemicals that block those receptors by competing with natural ligands, and tune neuronal activity.

Bicuculline is an antagonist for GABA receptors, being GABA the main inhibitory neurotransmitter in the CNS, associated with muscle contraction. Conversely, glutamate is the most abundant excitatory neurotransmitter, related to many cognitive functions such as memory and learning, whose main receptors are NMDA, AMPA and kainate. APV (A5282 Sigma–Aldrich) is a competitive antagonist for NMDA receptors and CNQX (C127 Sigma–Aldrich) is a competitive antagonist for AMPA/kainate receptors.

For resilience experiments in Chapter 4, the cultures under study were treated with inhibitory blockers (20 $\mu$l bicuculline, 40$\mu$M) to reduce activity modulations, then NMDA–mediated synapses were blocked with 16 $\mu$l APV to simplify excitation parameters, and AMPA/kainate receptors were systematically blocked to gradually weaken excitation in preset steps of CNQX.

### 2.4.2 Immunostaining

Immunocytochemistry (ICC) is a technique employed in biological research that utilizes antibodies for identifying specific proteins or antigens in cellular populations. Primary antibodies from non–repeated species bind to specific target proteins. Specie-matched secondary antibodies are conjugated to a flu-

orophore that emits at a chosen wavelength $\lambda$, and bind to primary antibodies, consequently amplifying the fluorescence intensity to allow detection.

Previous to the staining, it is necessary to fix the cells to preserve their morphology and architecture, and permeabilize them so antibodies can penetrate the plasmatic membrane and reach sub–cellular compartments. Therefore, ICC is limited to the study of dead cells.

ICC was performed at Hospital Clinic's facility. Cultured samples were fixed in 4% PFA (F8775 Sigma-Aldrich) for 2 hours at 4°C. After two washes with PBS cells were stored at 4°C. For the staining, samples were permeabilized with a blocking solution of PBS containing 0.025% Triton and 5% BSA/NDS for 45 minutes at room temperature (RT). Primary antibodies were applied diluted in blocking solution at ratios 1:100-1:1000, and incubated overnight at 4°C. Hereafter, samples were washed three times with PBS and incubated for 90 minutes with secondary antibodies.

Before imaging, cultures were washed again three times in PBS, submerged in milli-Q water to remove salts, and mounted on glass microscope slides (Superfrost Plus, Fisher Scientific) with a drop of fluoromount–G with DAPI incorporated. In the case of hydrogels, they were transferred to bottom–glass petri dishes and fluoromount–G was applied on top. Finally, images were taken at Hospital Clinic with a confocal microscope.

For cell characterization, we used the following antibodies: MAP2, a specific marker for neuronal phenotype (Izant and McIntosh, 1980) that appears in cell soma and dendrites; cortical layer markers as Cux1 (layers II-III), SATB2 (layers III-IV), Ctip2 (layer V) and Tbr1 (layer V, VI); GFAP, a filament protein localized in reactive astrocytes (Eng et al., 2000); and DAPI, a family of blue fluorescent dyes ($\lambda$ = 461nm) that stains DNA, i.e. every nucleus in the culture. Typical fluorophore emission for the secondary antibodies may correspond to any of these wavelengths: $\lambda$ = {488 nm (green), 570 nm (red), or 670 nm (far red)}. The tables 2.2 and 2.3 summarize the different immunostaining combinations applied within the present research.

**Table 2.2** Immunostaining for hiPSCs.

| *Culture* | *Primary Ab* | *Host* | *Ratio* | *Fluoroph* |
|---|---|---|---|---|
| Sample 1 | MAP2 | Mouse | 1:500 | Cy5 |
| | Tbr1 | Rabbit | 1:500 | Cy3 |
| | GPF | Goat | 1:500 | Cy2 |
| Sample 2 | MAP2 | Mouse | 1:500 | Cy5 |
| | Ctip2 | Rabbit | 1:500 | Cy3 |
| | GPF | Goat | 1:500 | Cy2 |
| Sample 3 | MAP2 | Mouse | 1:500 | Cy5 |
| | GFAP | Rabbit | 1:500 | Cy3 |
| | GFP | Goat | 1:500 | Cy2 |
| Sample 4 | MAP2 | Mouse | 1:500 | Cy5 |
| | Ctip2 | Rat | 1:500 | Cy3 |
| | Cux1 | Rabbit | 1:500 | Cy2 |
| Sample 5 | MAP2 | Mouse | 1:500 | Cy5 |
| | Ctip2 | Rat | 1:500 | Cy3 |
| | SATB2 | Rabbit | 1:500 | Cy2 |
| Samples 6–11 | MAP2 | Mouse | 1:500 | Cy5 |
| | GFAP-Cy3 | *Direct* | 1:400 | Cy3 |
| | Tbr1 | Rabbit | 1:500 | Cy2 |

**Table 2.3** Immunostaining for primary cultures.

| *Culture* | *Primary Ab* | *Host* | *Ratio* | *Fluorophore* |
|---|---|---|---|---|
| Sample 1 | MAP2 / $\beta$3tub | Mouse | 1:500 | Cy5 |
| | NeuN | Rabbit | 1:500 | Cy3 |
| | Ctip2 | Rat | 1:500 | Cy2 |
| Sample 2 | MAP2 / $\beta$3tub | Mouse | 1:500 | Cy5 |
| | Calret | Goat | 1:1000 | Cy3 |
| | Calbin | Rat | 1:10000 | Cy2 |
| Sample 3 | MAP2 / $\beta$3tub | Mouse | 1:500 | Cy5 |
| | GFAP-Cy3 | *Direct* | 1:400 | Cy3 |
| | NeuN | Rabbit | 1:500 | Cy2 |
| Sample 4 | MAP2 / $\beta$3tub | Mouse | 1:500 | Cy5 |
| | GAD67 | Chicken | 1:500 | Cy3 |
| | GLU (1,2b) | Rabbit | 1:500 | Cy2 |
| Hydrogels | MAP2 / $\beta$3tub | Mouse | 1:500 | Cy5 |
| | Ctip2 | Rat | 1:1000 | Cy3 |
| | SATB2 | Rabbit | 1:500 | Cy2 |

## 2.5 Data Acquisition

Neuronal activity was monitored by calcium fluorescence imaging, a set of techniques that provide high signal to noise ratio and single cell resolution. Continuous improvements of fluorescent dyes (Chen et al., 2013; Grienberger and Konnerth, 2012; Yang et al., 2018) in combination with state–of–the art imaging technologies allowed for real–time tracking of neuronal activity, culture characterization and 3D reconstruction.

### 2.5.1 Neuronal action potential

The membrane potential of a neuron is the voltage difference between the extracellular environment and the cytoplasm of the cell. In the resting state, an imbalance in ionic concentrations of $Na^+$, $Cl^-$, $K^+$ (among others) across the neuron membrane leads to a potential difference of typically -70 mV, a condition in which the neuron is considered polarized. A chain of events triggered by received neurotransmitters increases the incoming flow of charged particles through specific ion channels, mostly $Na^+$, rapidly increasing the membrane potential (depolarization). When a given threshold is reached, voltage–gated ion channels activate the propagation of an action potential (nerve impulse) along the axon (Figure 2.4).

Calcium ions play a fundamental role during this process. When the action potential reaches the pre–synaptic terminal, it then activates voltage–dependent calcium channels producing a high intake of calcium ions ($Ca^{2+}$), which triggers the release of neurotransmitters that would stimulate other neurons, into the synapse cleft (Figure 2.4). Therefore, calcium indicators can be used to reveal the occurrence of neuronal activations just by selecting a proper binding fluorophore and setting an adequate optical system for imaging.

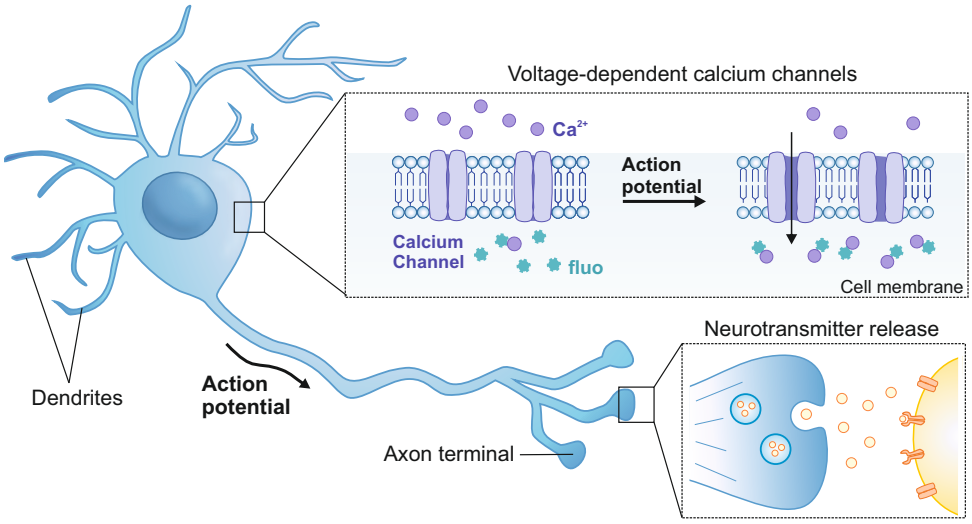


**Fig. 2.4 Schematic depiction of a chemical synapse.** The action potential transmission causes voltage-dependent calcium channels in the membrane to open. The fluorescence indicator previously applied, either Fluo–8th or GCaMP6s, reacts to the incoming intracellular calcium ions increasing the intensity of the fluorescence signal. These positive calcium ions push the synaptic vesicles containing neurotransmitters to the cell membrane and free them into the synaptic cleft, where they are detected by the receptors of post–synaptic neurons.

### 2.5.2 Wide-field calcium fluorescence imaging

This technique was used to record spontaneous activity through calcium imaging in Soriano's Lab. Fluorescence microscopy is a technique to visualize the light emitted by a fluorophore that has been excited by an adequate energy (and therefore radiation of a specific wavelength). Typically, we use GFP–like proteins that emit green light ($\lambda = 514$ nm) when excited by blue light ($\lambda = 490$ nm). Polarized neurons present a very low intracellular calcium concentration ($\approx 100$ nM) that increases by two orders of magnitude upon firing (Berridge et al., 2000). Thus, calcium–binding fluorescent proteins allow us to trace calcium transients during neuronal activations, which are revealed in the optical system as a sharp increase in the fluorescence signal.

Two types of calcium indicators are commonly used, namely chemical probes and genetically–encoded indicators. On the one hand, chemical probes are easily attainable, with nonexistent biological risk and sufficiently good signal to noise ratio to detect rapid depolarization spikes. They are toxic at long term since they need to be loaded into the cells through membrane–permeable agents, and thus they are inappropriate for long–term imaging. Conversely, genetically–encoded calcium indicators (GECIs) are proteins encoded into the DNA that remain stable along weeks. They are expensive, must be stored at -80°C, and have to be delivered by viral gene transfer, therefore requiring at least Biosafety Level 1.

For experiments lasting a few hours, we used chemical calcium dyes. They are simple molecules that become fluorescent upon calcium binding, usually modified by acetoxymethyl (AM) esters to facilitate permeability. In Soriano's Lab, we used the green indicator Fluo-8-AM (ATT Bioquest) due to its improved intensity and loading properties in respect to its predecessors. It was reconstituted in DMSO solvent at a ratio 1:5. Prior to recording, the culture of interest was incubated in darkness for 20 minutes, at room temperature, in a pH-stable recording solution (RS) that contained 1.5 $\mu$g/ml of Fluo-8-AM. The culture was then transferred to a bottom–glass petri dish filled with 2 ml of fresh RS to remove remnant dye in the medium.

For experiments that follow the same culture during weeks, we chose GCaMP6s (Addgene), a vector driven by synapsin promoter (Syn I) that is only expressed in mature neurons. It belongs to a group of ultrasensitive GECIs that includes the fluorophore sensor GCaMP (Chen et al., 2013). The indicator was incorporated into the cells through an adeno-associated virus (AAV), a safe replication–incompetent virus that is known not to cause disease in humans. The GCaMP6s probes come as ready to use AAV9 vials (Titer $\geq 1 \times 10^{13}$ vg/mL) which were applied at a ratio 1:1000, preferable 24h after plating the cells, and media is renewed 24-48h later.

Recordings were conducted on a Zeiss Axiovert inverted microscope equipped with a high–speed camera (Hamamtsu Orca Flash 4.0) in combination with a fluorescence light source (mercury–vapor lamp) (Figure 2.5 A). This technique is named wide–field because the fluorescence illuminates the entire sample. Images were acquired with the camera software Hokawo 2.10 at a minimum of 30 frames per second (fps) and up to 100fps, depending on the analysis requirements. Image size was $1024 \times 1024$ pixels with a spatial resolution of 5.76 $\mu$m/pixel when using a x2.5 lens.

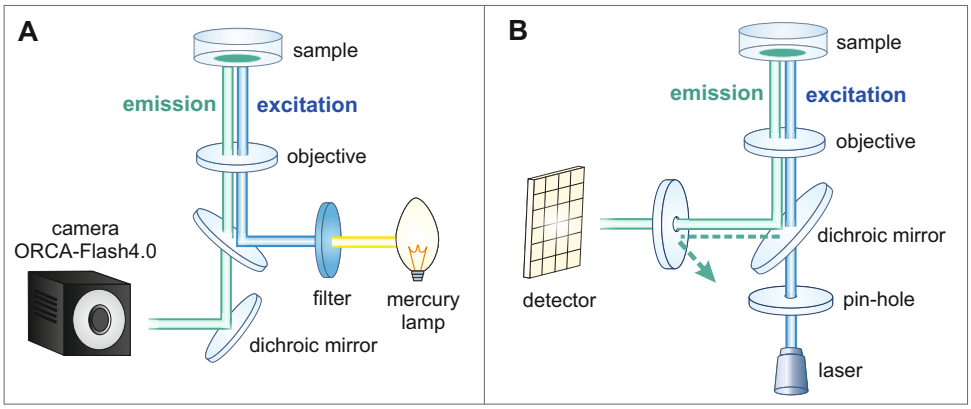


**Fig. 2.5 Fluorescence microscopy** (**A**) Illustration of Wide-Field fluorescence microscopy where a mercury lamp is the source of the fluorescence light. A color filter modifies the wavelength of the incoming white light. The dichroic mirrors guide the beam into the objective targeting the sample and backwards to the camera sensor. The camera is connected to a computer and programmed with the software HOKAWO. (**B**) Illustration of confocal microscopy where a high–intensity laser is the source of the fluorescence light. There are several lasers within the same set up because each laser has a particular wavelength, but work one at a time. The light crosses a pin–hole making the beam extremely accurate. Then the dichroic mirrors guide the beam into the objective targeting the sample and backwards to a sensor, passing the information directly to the computer.

### 2.5.3 Confocal microscopy

This technique was used to obtain immunostaining images. Confocal laser scanning microscopy (LSM) is a type of wide–field fluorescence microscopy that scans sample points sequentially. High–intensity monochromatic lasers emit the excitation light, whose power and gain is adjusted individually based on a preliminar image, as every fluorophore has a different intrinsic intensity. The emitted light from the sample goes back through a pinhole, a tiny aperture that only let pass the beam from the focal point. The pinhole serves to eliminate the background caused by out–of–focus light and scattering, obtaining sharp images with great contrast. The beam reaches a dichroic mirror, an optical bifurcation that reflects forward the light to the alignment path and into the camera sensor (Figure 2.5B).

The reduction of the pinhole aperture provides higher resolution but the detector recollects fewer photons, so the exposure time is increased to obtain images with enough brightness. The pinhole aperture also affects the depth of field (DoF), that is, the distance between the nearest and the furthest focused planes. Single images had DoF = $4\mu$m.

Once the optical sections from different focal planes have been collected, they are compiled into a 3D reconstruction or z-projection. Given that a neuron's size is around 20 $\mu$m, that is the minimum height for a complete scanned volume, so we captured 5 sections of $4\mu m$. Clusters of neurons may double that height up to 40 $\mu$m, and neurons grown on top of PDMS patterns may increase the height up to 80 $\mu$m. Lastly, 3D hydrogels require about 400 $\mu$m heights.

Images were taken at Hospital Clinic in Barcelona with the laser scanning confocal microscope ZEISS LSM 880, controlled by the software ZEN 2.3. The whole system stands on top of an optical table to prevent vibrations while scanning. Image resolution was $1024 \times 1024$ pixels in uncompressed TIF format.

### 2.5.4 Light-sheet microscopy

This technique was used to record activity in 3D networks at ICFO. Light–sheet fluorescence microscopy (LSFM) is a technique that provides good spatiotemporal resolution with low fluorescence intensity. In contrast to wide–field fluorescence microscopy, LSFM only illuminates a thin section (sheet) of a volume without affecting out–of–focus areas. This avoids optical aberrations and minimizes photobleaching and phototoxic effects (Olarte et al., 2018), essential to keep samples healthy and steady in long experiments. Another advantage is that LSFM setup is suited for fast three–dimensional (3D) imaging. It allows the scanning of 3D neuronal cultures with single cell resolution at sufficient speed to capture neuronal dynamics and render functional connectivity maps.

Fundamentally, LSFM consists on two water immersion objectives placed orthogonally. A first one emits the illumination sheet and the second one is responsible for the detection path. Illumination and detection focus are coordinated during the scanning through a galvanometric mirror and an electrically tunable lens, respectively (Figure 2.6). Both objectives are equipped with 10x lens of numerical aperture 0.3 (CFI Plan Fuorite Objective, 3.5mm WD, Nikon).

The light source is a diode laser beam of a 488 nm, expanded and guided into a cylindrical lens that modifies the circular beam into a line or sheet. The angular position of the galvanometric mirror is modified as a function of an input voltage, while the tunable lens exhibits a deformation in response to an applied voltage, changing its focal length. The detection objective collects the fluorescence emitted by the sample. Finally, a tube lens forms the image of the refocused plane onto the sensor of a sCMOS camera (Orca 4.0, Hamamatsu).

LSFM setup was assembled at the Institute of Photonic Sciences (ICFO) in Castelldefels, Barcelona. To avoid cell damage during transportation, we carried out dissections of Wistar rat embryos (E-18) at ICFO's Biology Lab following our experimental procedure. Cultures were incubated in their

facilities under proper temperature, humidity and $CO_2$ conditions. Prior to recording, 2D cultures were transferred to a 45 degrees platform filled with recording solution (RS) and 3D cultures moved to an isolated dish. The space between objectives limited the size of the sample to a reduced working distance of 400 $\mu$m in depth. Our 3D neuronal cultures are dynamic living systems where neurons connect in three spatial dimensions, either embedded inside a hydrogel or positioned on a scaffold. For fast acquisitions, we considered 20 fps per layer the minimum requirement to accurately inferred the functional connectivity of the neuronal network. On hydrogels, the scans were performed by acquiring a maximum of 12 layers per volume following a sinusoidal wave. The top and bottom layers were discarded due to the different velocity at the extremes of the sinusoid, leaving a total of 10 layers scanned up–down–up. The recording speed reached 264 fps per cycle, providing 132fps per volume (up–down) and as a result 22fps per layer. Then we performed a slow scanning at a frequency $f = 0.1Hz$ (1 cycle/20 seconds) to pinpoint the position of the cells, by taking 500 frames per cycle in the 400 $\mu$m volume.

The speed was limited by the field of view (FOV), such that the whole FOV will limit the camera speed to 100fps. We used the acquisition software Hokawo v10 synchronized with the camera and voltage-dependent elements through LabView 2017. Images had 2x2 binning and data was stored as multipage TIFF files, an uncompressed video format to avoid quality loss. Due to the huge amount of RAM needed experiments were limited to 10 minutes of duration.

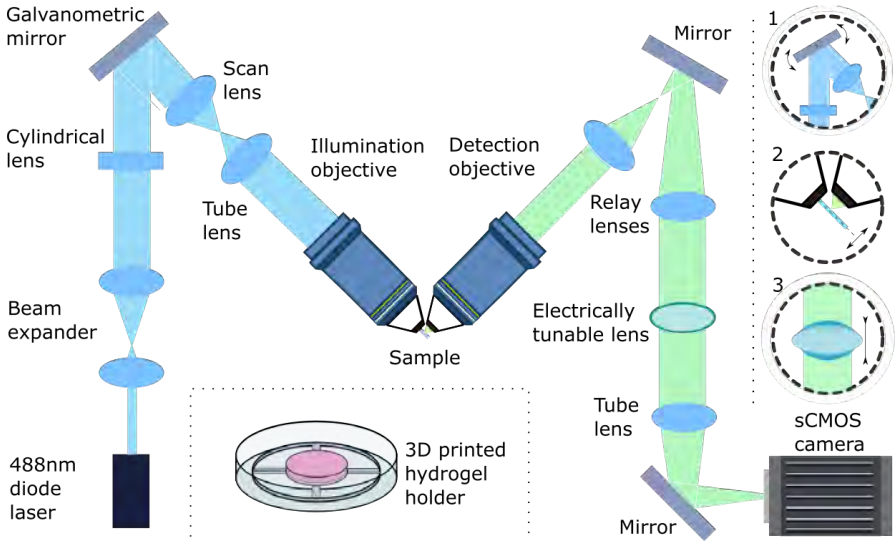


**Fig. 2.6 Light-sheet microscopy optical setup.** Custom-made iSPIM including a galvanometric mirror to scan the light sheet and an electrically tunable lens to focus at any plane without needing to move the sample or the detection objective. Volumes can be scanned at high rates when the galvanometric mirror (1) is rotated synchronously with the deformation of the tunable lens (3). This results in an always-in-focus light sheet acquisition of a still sample (2).

# Chapter 3

# Data Analysis Tools

In this Chapter, we first describe the methodology used to convert the recorded calcium fluorescence images into neuronal spike trains. Then, we introduce the main mathematical and statistical approaches to infer causal relationships among neurons and build effective networks. Next, we review the set of measures used to characterize the fundamental properties of the inferred networks, as well as other quantities of interest. All these data analysis ultimately shaped a series of pipelines and toolboxes that allowed us to elucidate the rich dynamical patterns of our neuronal cultures, both from primary rat cells and hiPSCs, either in the 2D or 3D environments.

## 3.1 From Fluorescence Recordings to Time Series

Recorded movies were analyzed with our software NETCAL (www.itsnetcal.com) in combination with a number of custom–made packages for specific tasks. Conceptually, the goal was to convert TBytes of acquired frames into manageable times series of neuronal activations. All procedures were similar for rat primary and hiPSC–derived cultures. The analysis for 2D cultures was con-

structed on Soriano's Lab expertise along 10 years, and adapted to recordings of a single–focused plane within 3D cultures. However, the scanned data of 3D volumes, obtained from LSM–microscopy (Section 2.5.4), was separated in several layers and required a minor yet crucial modification, consisting in the individual processing of layers as a series of 2D systems that were recombined afterwards.

Basic data processing comprised two aspects, the identification of the neuronal somas and the inference of neuronal spikes from each neuron fluorescence time series. It is worthy to pinpoint the impact of image acquisition rate in the quality of the results. High frame rates facilitate the detection of neuronal spiking events and require lower exposure times, which also lessens the background noise. However, the fluorescence intensity of the neurons is also reduced and weak firing episodes may be missed, unless highly-effective fluorescence dyes and strong excitation light are applied. As intense fluorescence causes photo–damage to neurons in the long term, the recording time becomes another important factor to proper balance image quality, cell viability and data reliability.

### 3.1.1 ROI identification

For each experiment, we obtained a high-contrast fluorescence image as the pixel-to-pixel average matrix of all frames in the recording. Neurons were identified manually or automatically in the resulting images and ascribed as Regions of Interest (ROIs).

The automatic ROI detection was performed by a custom-made program for *image segmentation*, an image processing technique to locate objects and boundaries. Briefly, the code first removed salt-and-pepper noise by applying a median filter, which computes the median value between the closest neighborhood around each pixel. Second, a fast local laplacian filter smoothed the background while enhancing the details (Aubry et al., 2014). Then basic morphological operations corrected mid-histogram and removed

axonal projections. Once the neurons were sufficiently defined and isolated, the image was binarized by converting pixels to 0 or 1 values based on a threshold. Finally, we calculated the Euclidian distance transform, i.e. the distance between every pixel and its nearest nonzero pixel, that correspond to the closest edge. Resulting regions were detected and labeled using a watershed algorithm. Fig. 3.1 illustrates the segmentation result.

The difference in basal intensity between neurons hindered the recognition of cell bodies with dim fluorescence levels. The use of the averaged image reduced this effect so only neurons that never fired during the recording time went unnoticed.

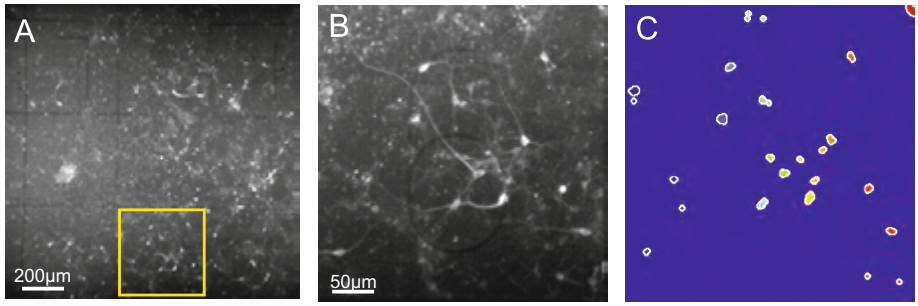


**Fig. 3.1 ROI segmentation A**. Averaged fluorescence image of an hiPSC–derived culture. **B**. Augmented detail of one quadrant. **C**. Watershed result of the segmentation. Most of the neurons were automatically detected and the ROIs follow their shape, including all the pixels within.

### 3.1.2 Spike detection

Once ROIs were mapped, we extracted the average fluorescence (gray scale level) of the pixels within each ROI to obtain the set of *raw fluorescence traces* $F_i(t)$ for each neuron $i$. Each trace was corrected from global drifts and artifacts and normalized as $\mathrm{DFF}_i(\%) \equiv 100 \cdot (F_i(t) - F_{i,0})/F_{i,0}$ where $F_{i,0}$ is the basal fluorescence of each neuron. This normalization was important since the relative change in fluorescence, and not its absolute value, is the

quantity that is biophysically relevant since DFF is proportional to the number of elicited action potentials.

Within this thesis we exclusively observed spontaneous activity, i.e. firing events in the absence of external stimuli. The sudden increase in fluorescence associated with an action potential occurs within a window of $10-50$ ms, while the gradual decay lasts for $1-4$ s (Smetters et al., 1999). Traces shown in Fig. 3.2 were obtained with the GCaMP6s sensor, which has a rise–time of $100-150$ ms, much slower than the GCaMP6f with $50-75$ ms (Chen et al., 2013), but faster kinetics usually comes in exchange of loosing affinity and smaller maximum fluorescence (Rose et al., 2014). It is also worth to mention the non–linearity of GECI sensors with respect to the cellular calcium influx (Rose et al., 2014).

The precise identification of spike trains from fluorescence data requires to introduce a model that captures the 'fast increase and slow decay' characteristic of neuronal activity. Unfortunately, the lack of an universal model to account for high noise and different neuronal firing states (e,g, spiking or bursting) is still an unsolved theoretico–computational problem. Currently, some of the most successful models in the literature are Oasis (Friedrich et al., 2017), MLspike (Deneux et al., 2016) and Peeling (Grewe et al., 2010), but after abundant testing none of them procured sufficiently reliable results for an automatic analysis.

We then considered a simplified strategy, limited to detect the onset time of activations as those events in which the fluorescence trace crossed a preset threshold, set as the mean plus 2 times the standard deviation of the fluorescence trace. We prevent the identification of false positives due to signal fluctuations by applying the Schmitt Trigger method, consisting on a lower second threshold that determines when a burst has finished. In other words, the termination of the firing event is established when the fluorescence intensity decreases to a level comparable to noise, hence the neuron is considered fully polarized.

We tested that this simplification did not compromise the reliability of effective connectivity inference and key network measures. Interestingly, differences among experimental realizations or the age of the culture *in vitro* provided a higher variability than the error introduced by using a friendly spike–inference method instead of a 'sophisticated' one.

An important consideration regarding the fluorescence probe chosen, is that the GCaMP family only infects mature neurons, while fluo-8th will enter also into glial cells. Strictly speaking, in this case detected ROIs could be either neurons or astrocytes. Astrocytes, however, have a characteristic fluorescence trace given a slow increase and a slow decay, and therefore they could be identified and excluded from analysis. Nevertheless, since astrocytes exhibit weak calcium transients as compared to neurons, they could be safely disregarded.

This inference method has been systematically used in previous studies when measuring the influence of a neuron onto another, e.g. for effective connectivity inference (Teller et al., 2014, 2015; Tibau Martorell et al., 2018; Yamamoto et al., 2018). But we note that, for more advanced analysis such as information flow, representation of stimuli or coding, one would need the precise spike trains. All these analyses, however, are beyond the scope of this thesis.

## 3.2 Network Effective Connectivity Inference

As elaborated above, considered the activations associated to the initiation of neuronal activity, and computed the effective networks of neuron–to–neuron interactions according to this data.

Neuronal populations are complex dynamical systems whose collective activity renders a broad landscape of activation patterns. These patterns depend on the network functional configuration, noise and the underlying physical wiring among neurons. Although it is presumed that the anatomy

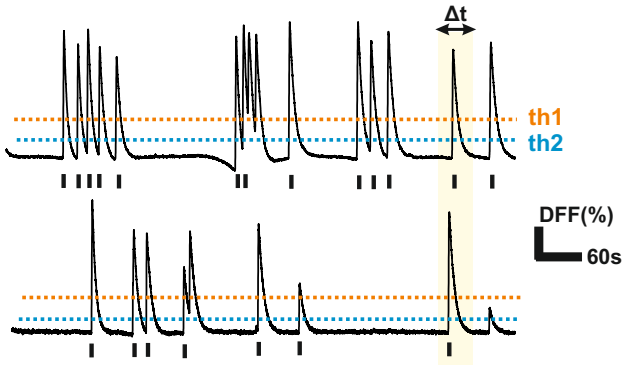


**Fig. 3.2 Smitch method for spike detection**Sample fluorescence signals from two neurons, recorded at 33 fps during 10 minutes. The first threshold (orange) delimits the spike time-point (black bars) while the second threshold (blue) serves as a cleaner of fast consecutive activations of the same neuron. When two spikes are detected within the same time window (less than few ms) they are considered synchronized.

of the neuronal circuit shapes its collective dynamics, is not possible to pinpoint their entangled physical connections from the observation of their dynamics. Thus, when trying to understand how neurons are interacting among themselves in the network, it is adequate to just focus on measures that account for their cross–talk in a *statical* manner, i.e. without trying to ascertain whether the neurons are anatomically linked or not. Indeed, it is important to note that *anatomical connectivity reconstruction* from spontaneous activity data is an unsolved difficult problem that is thoroughly investigated in the context of information theory. Hence, it must be left clear that our goal in the present thesis was not to unveil the anatomical layout of the studied networks, but rather assess the cross–talking among neurons at different experimental conditions and time points.

To evaluate the cross–talking (or *functional interaction*) among neurons, we searched for significant statistical relations between the firing patterns of any two pairs of neurons. For the statistical computation of the influence of one neuron into another, two proposed methods procured directed and

weighted interactions, namely *Time–delays* and *Generalized Tranfer Entropy* (GTE). On the other hand, to ascertain that the influence estimated cannot occur by chance, we established the significance by building surrogates — randomizations of the original time series— and set confidence intervals in the form of z–scores. The overall mathematical implementation procured *effective* (weighted and directed) networks, that represent statistically the dynamical state of the studied cultures. These networks were defined by neurons (nodes) connected by links, with an assigned weight and specified directionality. When directionally was omitted, the networks were simply called *functional*.

Time–delays and GTE are grounded on completely different ideas. Time–delays is a linear method that ascribes the weight of an effective link to the time span in the activation of any pairs of neurons. The shorter the time, the stronger the link. The directionality of the weight is straightforward, based on the temporal order of activation of the studied neurons. GTE is a non–linear method, born from information theory, that unveils causal (and therefore directed) relationships among firing neurons. The strength (*GTE score*) of the relationship is conceptually based on the amount of information that a neuron passed into another neuron.

Based on the experience of our research group and associated publications, for the present thesis we already knew that Time–delays and GTE provided comparable effective connectivity matrices for fluorescence data recorded at high frame rates (50 fps or higher) with strong activity and low noise (Teller et al., 2014). Indeed, for experiments with aggregates of neurons recorded at 50 fps or higher, and with activation rates of at least 4 firings/min, we observed quantitatively similar networks using either methodology. GTE, however, performed better for low frame rates (typically 20 fps), weak activity and high noise (Orlandi et al., 2014; Stetter et al., 2012). Therefore, a compromise had to be made between the reliability of the procured effective networks and the computation time. GTE needs on the order of hours to analyze a typical

recording of 30 min at 20 fps and 100 neurons. Analysis may take days when treating 1000 neurons. Time–delays is at least twenty times faster.

Effective connectivity inference is a growing and quickly evolving research field. By the end of this thesis, a new ultra–fast GTE implementation was introduced in the community, reducing any analysis to few minutes, and we took quick advantage of this implementation to analyze all datasets, particularly the largest ones, with GTE.

Taking all the above considerations, in the thesis we typically used Time–delays in all cultures with clustered networks and in experiments with single cells (both in 2D and 3D) recorded at high speed. For the rest of experiments, in particular those in 2D and 3D recorded at ICFO, we used GTE with its fast implementation.

### 3.2.1 Implementation of the Time–Delays method

The concurrent activations of two or more neurons within a time window is described as a *firing sequence*. This time window is defined in the range $0.01 - 1$ s depending on the speed of the signal propagation, that may vary between cell lines and experimental conditions. Following (Teller et al., 2014), a directed and weighted graph was constructed by analyzing the time–delays of node pairs activations within a sequence.

The directionality of the link between neurons $i, j$ was set according to the temporal order of activation. The weight of the link was established as a decaying function of their time delay. The shorter the delay, the stronger the weight. This construction, extended over all observed sequences, procured the average weight $w_{ij}$ of the effective links. Significance of links' weights was then established through a null model built upon 500 surrogates, procuring a final weight $a_{ij}$ given by

$$a^*_{ij} = \frac{w_{ij} - \langle w^S_{ij} \rangle}{\sigma^S_{ij}}, \tag{3.1}$$

where $\langle w_{ij}^S \rangle$ is the average weight of the surrogate connectivity matrix, and $\sigma_{ij}^S$ its standard deviation. Values $a_{ij}^* < 0$ were reset to zero since rendered effective connections whose weights were less probable than in a random configuration. Finally, the remaining $a_{ij}^*$ values were rescaled as $a_{ij} = a_{ij}^* / \max(a_{ij}^*)$ to procure a connectivity matrix $\mathbf{A} = \{a_{ij}\}$ with weights in the range $[0,1]$.

### 3.2.2 Implementation of Generalized Transfer Entropy

Information theory (Shannon, 1948) is a common resource in neuroscience to unravel the nonlinear interactions between neurons. The Shannon Entropy of a stochastic variable $X$ with values $\{x_1,...,x_n\}$ and probability distribution $p(x)$, defines the average amount of information acquirable from the single variable, as

$$H(X) = \sum_{i=1}^{n} p(x_i) \log \frac{1}{p(x_i)} \tag{3.2}$$

Spontaneous activations of neurons corresponded to stationary stochastic processes. Given two processes $(X,Y)$, with joint probability $p(x,y)$, the error of assuming both processes independent is $p(x,y)/p(x)p(y)$ as reflected in the Mutual Information (MI). This measure is a particular case of Kullback–Leibler divergence (Kullback and Leibler, 1951) and quantifies the reduction of uncertainty about one variable by observing another, i.e. when $\mathrm{MI} = 0$ the two variables are independent:

$$MI(X,Y) = \sum p(x_i,y_i) \log \frac{p(x_i,y_i)}{p(x_i)p(y_i)} \tag{3.3}$$

Mutual Information is symmetric, but the signal transfer between two neurons is not even necessarily bidirectional. To introduce the directionality of the information, a time lag is added to one of the processes. Given the Markov property, the conditional probability of a memoryless system depends only on the present states, such that

$$p(x_{n+1} \mid x_n^k) = p(x_{n+1} \mid x_n^k, y_n^k) \tag{3.4}$$

where $n$ is the discrete time index, and $x_n^k$ is a vector whose entries are the samples of $X$ at the time steps $\{n, n-1, ..., n-k\}$ for Markov order $k$. Hence, the deviation from the Markov condition corresponds to the causality measure between both systems. The *Transfer Entropy* (Schreiber, 2000) is thus an asymmetric measure of the uncertainty between two time–series processes $(X,Y)$,

$$TE_{Y\to X} = \sum p(x_{n+1}, x_n^k, y_n^k) \log \frac{p(x_{n+1}, x_n^k, y_n^k)}{p(x_{n+1} \mid x_n^k)} \tag{3.5}$$

In all analyses we took $k = 2$, and in accordance to extensive studies and simulations of TE by Soriano's research group and collaborators (Orlandi et al., 2014; Stetter et al., 2012).

Generalized Transfer Entropy (GTE) is a slightly modified version of TE that was specifically introduced for neuronal cultures in an effort to balance the contribution of neuron–to–neuron direct spikes and whole–network synchronous events (*network bursts*) (Orlandi et al., 2014; Stetter et al., 2012). This balance is important. Since network bursts encompass the entire culture, TE would render effective networks biased towards an all–to–all connectivity. The balance procured by GTE unmasks the details of neuronal interactions and renders much richer effective networks. GTE is implemented by applying a thresholding condition in the fluorescence signal to minimize the impact of network bursts and remarkably improved the fraction of true positives in respect to false positives in spike detection. GTE was embedded in our Matlab software NETCAL.

To construct the effective networks, the causal relationship between spike trains of every pair of neurons was translated into a functional connectivity map, where high GTE scores corresponded to strong functional connections. To render significant links, a z–score was introduced as

$$z_{ij} = \frac{u_{ij} - \mu}{\sigma}, \tag{3.6}$$

where $u_{ij}$ is a GTE value, $\mu$ is the average of all GTE values, and $\sigma$ their standard deviation. Those links that verified $z_{ij} \geq z_{th}$, with $z_{th} = 2$ were deemed as significant, denoted $a^*_{ij}$ and saved for further analysis. The rest were set to 0. As before, the set of surviving links' values were rescaled as $a_{ij} = a^*_{ij}/\max(a^*_{ij})$ to procure a connectivity matrix $\mathbf{A} = \{a_{ij}\}$ with weights in the range $[0, 1]$.

## 3.3 Network Analysis

In the past decade, network science has aroused great interest due to its numerous applications. The definition of network as a large set of interconnected elements comprehends a wide range of systems, from social networks and distribution chains, to the most complex circuitry in nature: the brain.

Neurons can be defined as nodes connected by *structural* links, the neuronal junctions or synapses, or by *functional / effective* links that correspond to the statistical dependencies between neurons' activations. Within this framework, network theory has proven to be a befitting tool to deeper our understanding upon brain function and neuronal diseases (Bassett and Sporns, 2017), as it provides the mathematical foundation needed to characterize their topological and functional properties.

In this Section we describe the network attributes extracted from our effective networks with $N$ nodes, which can be either clusters or neurons. All networks were weighted and directed (WD). Descriptive properties of network topology were computed using the Brain Connectivity Toolbox of Matlab (Rubinov and Sporns, 2010), while measures of network complexity, i.e. dynamical richness and synchrony, were calculated by custom–made Matlab codes. A schematic WD network is represented in Fig. 3.3.

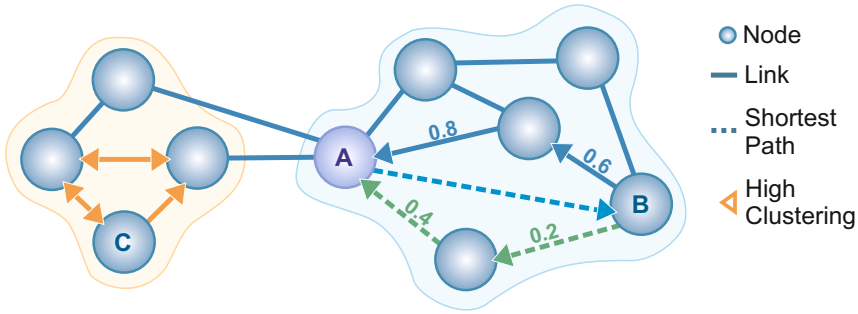


**Fig. 3.3 Scheme of basic topological properties.** In this puppet weighted and directed network most of the weights and the arrows were omitted for simplicity. The dashed blue line corresponds to the shortest path A → B, the dashed green line corresponds to the shortest path B → A, as the network is directed, i.e. asymmetric. Although there are other routes for B → A with the same length, in weighted networks the shortest path also fulfills the minimum cost. Incidentally, the node A is a hub between two modules. The node C is an example of clustering, where the neighbors of a node are acquaintances.

### 3.3.1 Link distribution

The degree of a node ($k_i$) is the number of connections it has with other nodes. For directed networks, it is the sum of the incoming and outgoing connections. Nodes with high degree are very integrated in the system and may serve as hubs.

Accordingly, the degree distribution $P(k)$ is the probability distribution of encounter the degree $k$ over the entire network. Neuronal networks usually exhibit scale-free distributions in which the occurrence of of $k$ values follows a power law $P(k) \sim k^{-\gamma}$ being $2 \leq \gamma \leq 3$ (Barabasi, 2009; Barabasi and Albert, 1999) such that the majority of the links have a low degree. Scale–free networks typically appear in the brain, but in neuronal cultures Gaussian–like distributions have also been reported (Tibau Martorell et al., 2018).

For weighted networks, the degree is complemented with the nodal strength ($s_i$), the sum of the weights of the links connected to that node, that can also be split as in-strength and out-strength. Nodes with low degree may have high strength if those connections participate often in fast activation sequences.

$$s_i^{out} = \sum_{j \in N} w_{ij}, \quad \text{and} \quad s_i^{in} = \sum_{j \in N} w_{ji}, s_i = s_i^{out} + s_i^{in}. \tag{3.7}$$

Another fundamental property is the link density ($D$), the fraction of total existing links in respect to all possible connections, for the current network of size N, such that $D = \sum_{ij} a_{ij}/(N(N-1))$. A network with low link density would be very disconnected, while another with excessively high density may become globally inefficient.

### 3.3.2 Path length and global efficiency

Considering a generic NxN functional matrix $A$ with weighted (i,j)-entries, the *shortest path* ($d_{i,j}$) is the route between two nodes $(i, j)$ that minimizes the sum of weighted links crossed. Its average value between every possible pair of nodes is known as the *characteristic path length* ($L$) and is dependent of the system size $L \propto \ln N$ ((Barabasi, 2009)).

$$L = \frac{1}{N(N-1)} \sum_{i \neq j \in A} d_{i,j} \tag{3.8}$$

The *Global Efficiency* ($E$) is a measure of integration that quantifies how optimal is the spreading of fast transmissions through the system (Latora and Marchiori, 2001). In other words, the network is more efficient if there are shorter paths to facilitate signal transferring between pairs of nodes, and thus it is defined as the inverse of the average shortest path. In disconnected networks where some nodes are totally independent, $d_{i,j} = \infty$ while $E \to 0$.

$$E = \frac{1}{N(N-1)} \sum_{i \neq j \in A} \frac{1}{d_{i,j}} \tag{3.9}$$

### 3.3.3 Clustering and local efficiency

The *Clustering coefficient* (Watts and Strogatz, 1998) is the fraction of pairs of neighbors that are also directly connected, forming a triangle. The geometric mean of triangles involving node $i$, taking into account the directionality of the links, is defined as:

$$t_i = \frac{1}{2}\sum((w_{i,j} + w_{j,i})(w_{i,h} + w_{h,i})(w_{h,j} + w_{j,h}))^{1/3} \tag{3.10}$$

The clustering coefficient depends on the degree of each node, but for weighted networks we have to consider the nodal strength $s_i$ instead. The mean clustering coefficient (C) is a measure of segregation.

$$C = \frac{1}{n}\sum_{i \in N} C_i = \frac{1}{n}\sum_{i \in N} \frac{t_i}{s_i(s_i - 1) - \sum_{j \in N} w_{i,j} w_{j,i}} \tag{3.11}$$

The local efficiency defines how the local connections are distributed in a similar way to the clustering coefficient. It is defined as the average efficiency of local subgraphs $G$ such that $E_{loc} = \frac{1}{N}\sum E(G)$ (Latora and Marchiori, 2001), and for non-sparse subgraphs it can be considered an approximation of $C$.

### 3.3.4 Node centrality

*Betweenness centrality* (Freeman, 1978) measures the number of shortest weighted paths that pass through every node. Nodes that are frequently part of shortest paths display high betweenness centrality scores, as in the case of nodes that bridge distinct subnetworks. Ideally, those nodes will have greater influence and control over information transfer. However, information not always takes the shortest route, hence the importance of complement different measures to describe a networked system.

$$b_i = \frac{1}{(N-1)(N-2)}\sum \frac{\rho_{hj}(i)}{\rho_{hj}} \tag{3.12}$$

where $\rho_{hj}$ is the number of shortest paths between h and j, and $\rho_{hj}(i)$ is the number of shortest paths between h and j that pass through i.

Together with the nodal strength and local efficiency, betweenness centrality is one of the key features commonly used to label network *Hubs*, high-degree nodes placed in a convergence location either connecting nodes within their same module (provincial hubs) or across different modules (connector hubs) (van den Heuvel and Sporns, 2013).

### 3.3.5 Modular organization

The modularity of neuronal networks is an essential property of the integration-segregation balance in the system. It describes the network when it is organized in non-overlapping communities of neurons, also called *modules*, that exhibit much stronger intra-module connections than inter-module connections. From the perspective of effective connectivity, communities are patterns often activated in synchrony.

There are not universal guidelines for community detection. Following previous studies (Teller et al., 2015; Yamamoto et al., 2018), we obtained a pairwise similarity matrix by calculating the Jaccard Similarity Metric over every pair of nodes $0 \leq J(A,B) \leq 1$ as the fraction between concurrent activations and all the occurrences involving at least one of them. This similarity was normalized using a z–score with respect to a null model of 500 surrogates,

$$J(A,B) = \frac{|A \cap B|}{|A \cup B|} \tag{3.13}$$

Neurons were then arranged with hierarchical clustering using the Jaccard Distance $d_J(A,B) = 1 - J(A,B)$. Starting at the singleton condition, neurons were iteratively grouped based on the average linkage $d_{AL}$, the mean distance between nodes of each module. All possible categorizations were ultimately summarized as a hierarchical tree or dendrogram (Statistics and Machine Learning Toolbox, MATLAB).

To establish the sets of communities, we used the threshold that maximizes the variation of information (Karrer et al., 2008), that is, the maximum distance between two community assignments, as illustrated in Fig. 3.4, and given by

$$V(X,Y) = H(X|Y) + H(Y|X) = -\sum p(x,y) \log \frac{p(x,y)}{p(y)} - \sum p(x,y) \log \frac{p(x,y)}{p(x)} \tag{3.14}$$

The minimum variation $(V = 0)$ occurs when two consecutive partitions $(X,Y)$ result in the same number of modules, whereas the maximum variation $(V = logN)$ is the trivial scenario where one partition categorizes all the nodes together in a unique group and the other establishes each node as a singleton community.

Additionally, to qualify the modularity we used *Louvain Modularity* $Q \in [-1,1]$, a parameter that helps us represent the proportion of within-group connections in relation to between-group connections. Specifically, it corresponds to the optimized value found by a greedy algorithm that maximizes the modularity, starting from the singleton situation where every node is independent and stopping when it is not possible to improve modularity anymore (Blondel et al., 2008; Sun et al., 2009). A positive gain in modularity is assumed when the links between nodes A and B are greater than expected by chance. Then, when $Q = 0$ the degree of intra–module connectivity does not differ from a null model, and when $Q$ is negative the network lacks modular structure (Fornito et al., 2016).

This algorithm has two main advantages against others: it is fast enough to be applied in large networks and its iterative escalation makes it less susceptible to the *resolution limit*, a well-known bias that skips detecting small communities even in cases where they are unambiguously defined (Fortunato and Barthélémy, 2007).

In some analysis we considered two different $Q$ values, named $Q_1$ and $Q_2$, as explained in Section 3.5.

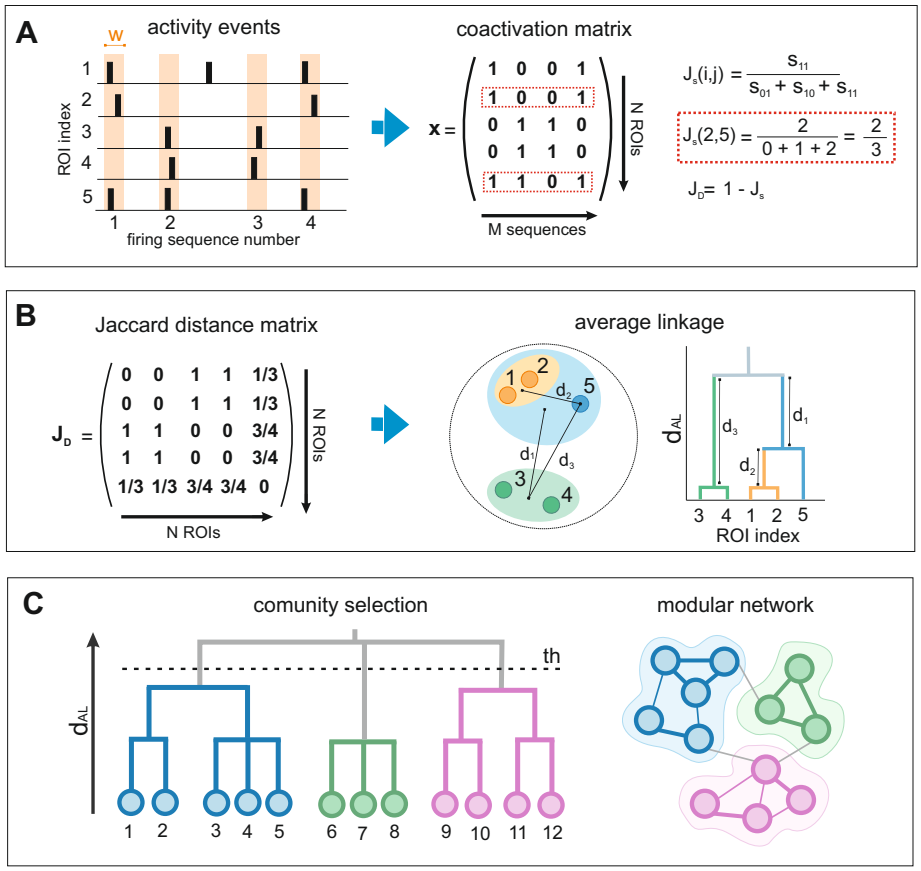


**Fig. 3.4 Schematic representation for module categorization and selection (A)** Activity trains for 5 nodes, either neurons or clusters. All those nodes that are activated concurrently in a short time window (w) are defined as a sequence (orange shadows). Nodes that fire independently are discarded. Then the matrix $x$ is established based on the Jaccard similarity measure between all pairs (i, j). **(B)** For better interpretation, we work instead with the Jaccard distance matrix $J_D = 1 - J_S$, a symmetric matrix that reflects the relative closeness between all pairs. Two or more ROIs with similar activity history are more likely to constitute a community. As ROIs #3 and #4 have identical histories they form a unique community providing $JS(1,2) = 1$. ROIs #1 and #2 are also identical in history, but both are also close to #5, with $JS(1,5) = 2/3$. **(C)** The number of communities is formally set by selecting a threshold that maximizes the average linkage distance. In this example, a network composed of 12 nodes with links of different strength is categorized into three different modules, illustrated in different colors.

### 3.3.6 Dynamical richness

Dynamical richness $\Theta$ quantifies the complexity of the dynamic regimes in a neuronal network (Yamamoto et al., 2018). $\Theta$ depends on the variability among the activity patterns of firing neurons and the variability among the size of modular activations. a situation in which neurons coactivate in groups of varying size and temporal occurrence correspond to large $\Theta$, while invariant states, either random activations or persistent whole–network synchronization, give $\Theta = 0$.

Mathematically, we define the dynamical richness $\Theta$ as a combination of two contributions, $\Theta_{CC}$ and $\Theta_{GNA}$. The first one, $\Theta_{CC}$ takes first into account the pair–wise correlation values $r_{ij}$ among all neurons in the network. These values are then represented as a histogram with $m = 20$ bins, and the histogram normalized to build the probability distribution $p(r_{ij})$. We choose to calculate the variance of that distribution as the difference between $p(r_{ij})$ and the uniform distribution, also estimated in $m$ bins, $p(r_{ij}) = \bar{p}_\mu = \frac{1}{m}$ for all bins $\mu = 1, 2, ..., m$. We quantify functional complexity as the sum of this difference over the bins, i.e.

$$\Theta_{CC} = 1 - \frac{m}{2(m-1)} \sum_{\mu=1}^{m} \left| p_\mu(r_{ij}) - \frac{1}{m} \right|, \tag{3.15}$$

where $|\cdot|$ indicates the absolute value.

The second one, $\Theta_{GNA}$, follows the same construction but using the variability among the size of *global network activations* (GNA). To find this measure, the time-series of GNA occurrences are analyzed, and the corresponding histogram of values and probability distribution $\Gamma_t$ built. We note that coherent network activations provide $p(\Gamma_t) = 1$, and random activations procure $p(\Gamma_t) \simeq 0$. As before, $\Theta_{GNA}$ is the separation from these extreme cases as

$$\Theta_{GNA} = 1 - \frac{m}{2(m-1)} \sum_{\mu=1}^{m} \left| p_\mu(\Gamma_t) - \frac{1}{m} \right|. \tag{3.16}$$

The dynamical richness is finally given as $\Theta = \Theta_{CC}\Theta_{GNA}$. The rationale for using the product of two quantities is two maximize the differences between experimental conditions, and to ensure that modules of identical size that fire synchronously within them but that are totally disconnected from one another show low richness. Indeed, let us imagine 4 interconnected modules as in (Yamamoto et al., 2018) that activate randomly in these conditions. One would observe a high $\Theta_{CC}$, portraying a wrongly assessed rich dynamical systems since its forming units are disconnected. The GNA computation will show identical values sizes all modules are similar in size, procuring $\Theta_{GNA} \simeq 0$. Thus, our definition of $\Theta$ is an effort to reduce the impact of totally independent modules.

### 3.3.7 Synchrony index

Here we estimated the synchronization of the system as the 'Synchrony index' *Syn*, defined as the ratio between synchronized neuronal bursts with respect to the total number of events in a time series. We typically considered an event *synchronous* when more than 40% of the active population took part in the bursting ($\alpha = 0.4$), as even in overpopulated bursts the participation rarely exceeds 80%.

From the inferred time–points of spiking activity, we captured $K$ time–windows with 1 second of duration starting at the first frame any activation occurred. Hence, every time window corresponds to an event, either a random spike or a bursting sequence. In this construction there was no overlapping between windows and firing neurons were counted only once per event. The participation or number of neurons involved in every event $P_K$ was normalized by the total number of active neurons to avoid network size variations, i.e. $\tilde{P}_K = P_K/N$. The index was then defined as

$$Syn = \frac{1}{K}\sum \tilde{P}_K \geq \alpha \tag{3.17}$$

As shown in Figure 3.5, this index quantifies how close is the network dynamics to an exclusively synchronous state. The presence of events with low participation reduces synchrony index.

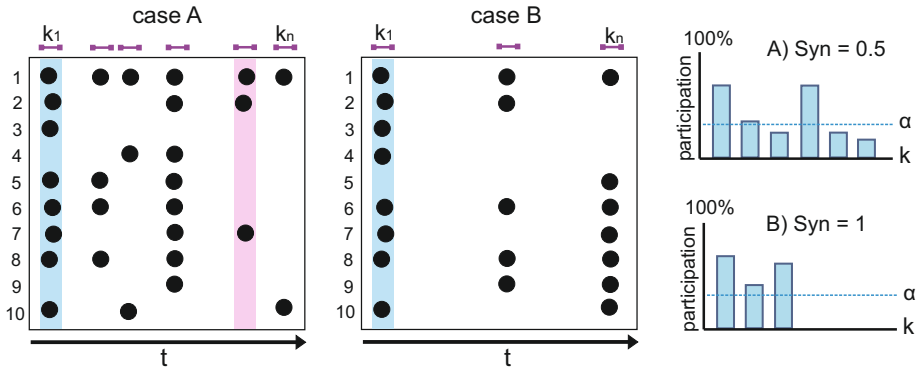


**Fig. 3.5 Synchrony Index illustration** Two sample rasterplots (A,B) display the activations of 10 neurons, represented as dots, within the recording time $t$(s). Time windows of 1–second duration are taken every time an event starts, and the percentage of neurons that participated in each event are calculated. The number of events when the participation exceeded a certain value $\alpha$ in respect to the total number of windows (or events) taken corresponds to the synchrony index.

## 3.4 Data Consistency

In this Thesis we applied two methods to infer effective connectivity, namely 'time delays' and 'transfer entropy'. Both methods provided more consistent results in experiments with higher frame rates or slower functional dynamics (i.e. clustered cultures), in the sense that they rendered similar effective connectivity matrices and that the differences observed between them did not significantly affect the numerical values of network properties such as the modularity index Q or the global efficiency.

An example is provided in Figures 3.6A–B, which corresponds to a typical clustered neuronal culture with 27 clusters. Data was recorded at 100 fps, and analyzed with both methods. As the figure shows, the module–ordered effective connectivity matrices exhibit a similar structure, rendering the same modules. The strongest connections practically coincided in both cases. 'Time delays' showed more connections beyond these top scores, but they were low ranked. The graphical representation of the network is shown in Figure 3.6C.

We repeated this test several times with different networks, and observed that both methods were consisted only for experiments with high acquisition rate, typically in the range $50 - 100$ fps. Below 50 fps, only transfer entropy procured significant connections. Additionally, in all our explorations, we observed that the variability among culture preparations caused much more dispersion in the data than the use of one method for inference or the other.

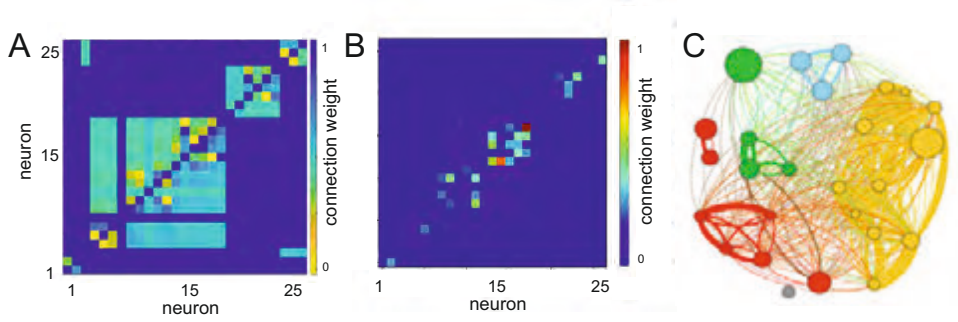


**Fig. 3.6 Comparing 'time delays' and 'transfer entropy'.** (**A**) Adjacency matrix obtained with time delays. (**B**) Adjacency matrix obtained with transfer entropy. The brighter the colors, the stronger the connection. (**C**) Graphical representation of the 'time delays' network Transfer entropy procured a similar map, but the weakest connections were not present. Colors indicate modules. Links' thickness are proportional to connectivity weight.

## 3.5 Conditioning of data and z–score

An important number of experiments contained synchronous events (Figure 3.7A, left) that could mask the inner effective connectivity structure of

the networks. By removing those events (Figure 3.7A, right) we could unveil rich details of the network.

To carry out this analysis without manipulating the raster plots we observed, during the analysis of data using transfer entropy on the whole raster, that by adjusting the significance threshold for the accepted effective links we could render different networks. This threshold actually corresponded to the z–score $z$ for significance. For a low value $z = 1$ we observed that the procured effective networks were very similar to the ones obtained with cross–correlation (Figure 3.7A–B). This was advantageous in the context of data that contained synchronous events. In such a situation, cross–correlation and transfer entropy with $z = 1$ provided a functional network in which all neurons were strongly linked. However, synchrony fully masked the inner structure of neuronal cross–talking. By using $z = 2$ this structure emerged (Figure 3.7C).

Thus, we observed that by combining the two z–scores we could obtain complementary data. With $z_1 = 1$ (and corresponding modularity index $Q_1$) we could pinpoint the contribution of bursts on network effective traits, and with $z_2 = 2$ ($Q_2$) we could bring to the surface precious inner, neuron–to–neuron interactions that were masked by the bursts.

## 3.6 Significance: t-test

Data was usually expressed as mean and standard deviation. Statistical analysis was performed using the unpaired Student's t-test or two-way ANOVA. The p-value significance p was indicated as * for $p < 0.1$, ** for $p < 0.01$ and *** for $p < 0.001$.

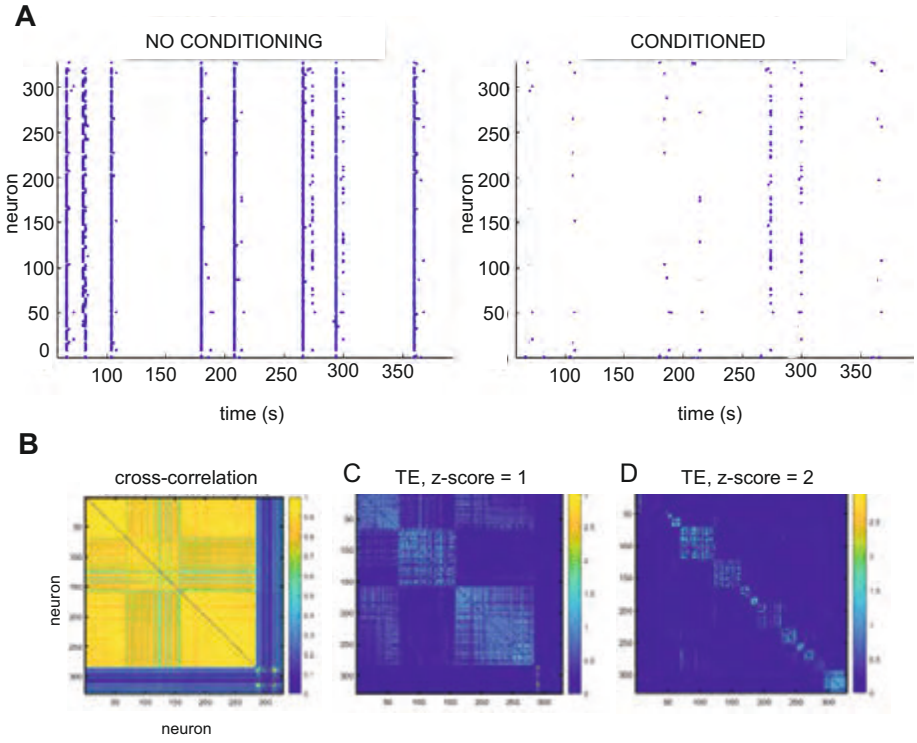


**Fig. 3.7 Impact of z–score.** (**A**) Left, Raster plots of a typical 2D culture exhibiting strong bursting (full synchronous events). Right, The same raster after eliminated the synchronous events, thus emphasizing single activations or small structured coactivations. (**B**) Adjacency matrix obtained with cross–correlation of the full raster plot. All neurons are highly connected, but a small inner structure can be discern. (**C**) Corresponding analysis using transfer entropy and a z–score $z_1 = 1$, providing very similar results. (**D**) Same transfer entropy analysis with $z_2 = 2$, showing details of the rich inner structure of the network masked by the global synchrony. The latter analysis is very similar to compute transfer entropy to the conditioned, bursts–free raster plot.

# Chapter 4

# Results I: Resilience Mechanisms upon Connectivity Breakdown

Modeling damage in living neuronal circuits is a central yet unresolved problem in neuroscience. Intuitively, the loss of connections should precipitate a progressive failure of network activity and compromise the functionality of the circuit. However, the complex interplay between the physical architecture of the network, neuronal dynamics, noise and plastic mechanisms, shapes yet unpredictable scenarios of response, adaptation and recovery that cannot be disregarded. Indeed, as we will see in this Chapter, these scenarios challenge expected results in neuronal circuits and call into question the validity of excessively simple models.

The analysis of the network resilience and the assessment of its self-healing potential is helping us to develop models to measure damage upon disturbance, with promising applications for the study of neuronal disorders *in vitro*. In this regard, the aim of this Chapter is to shed light on resilience that emerge in the presence of malfunction–like events, to investigate the impact of –the often ignored– plasticity, and to quantify functional alterations in the system from the network perspective.

In a nutshell, we investigated experimentally and numerically the action of a chemical perturbation on the functional connectivity of *clustered* neuronal networks. The monitoring of spontaneous activity, upon progressive weakening of the excitatory connectivity, revealed that their global efficiency exhibited an initial phase of transient strengthening followed by a second phase of steady deterioration. Numerical models of connectivity deterioration on the same, experimentally–measured functional networks suggested that *synaptic scaling*, a synaptic plasticity mechanism, was a central at shaping the transient increase of the global efficiency upon failure. Notably, we observed that simple numerical models lacking plasticity failed at reproducing the experimental behavior.

The Chapter is organized as follows. We first introduce the basics of synaptic plasticity (Section 4.1) and then describe the experiments performed on primary clustered cultures (Section 4.2). Next, we describe data analysis aspects specific of this study and that were excluded in Chapter 3. These analyses include the computation of different network measures and the quantification of resilience. Finally, we briefly discuss the implications of plasticity mechanisms in the study of networks and degenerative models.

## 4.1 Neuronal homeostatic plasticity

Neuronal circuits, and by extension the brain, exhibit homeostatic mechanisms to regain stability in the presence of perturbations (Costa et al., 2017; Marder, 2011). Proper performance conditions are reliant on neuronal plasticity and adaptable functional connectivity. Indeed, these mechanisms are believed to be the cornerstone for information storage, and thus they are involved in learning and memory (Zenke et al., 2015) but they are also fundamental for development and recovery from injury (Murphy and Corbett, 2009).

To date, neuronal plasticity is classified in two groups: Hebbian plasticity and homeostatic plasticity. Hebbian plasticity is a positive feedback

that occurs when repeated activations between pairs of neurons facilitate following activations, increasing synaptic strength. Conversely, homeostatic plasticity is a negative feedback mechanism that compensates changes in activity to restore basal firing rates (Lisman, 2017), increasing or decreasing strength accordingly. Hebbian plasticity includes 'short–term' and 'long–term' potentiation (STP, LTP), a series of local mechanisms that may cause function destabilization. On the other hand, homeostatic plasticity includes 'distance–dependent scaling' and 'synaptic scaling', both considered global compensatory mechanisms.

Distance–dependent scaling compensates the attenuation of signal propagation through long dendrites (Menon et al., 2013; Nicholson et al., 2006), so spatially distant neurons can be strongly coupled, even more than neurons that are near each other. This property hinders the study of homeostatic mechanisms in a crowded system from the structural point of view. Finally, synaptic scaling takes place at post–synaptic neurons when channels are chemically blocked and post–synaptic firing is altered (Turrigiano, 2008), and consists on adjusting the strength of excitatory synapses to compensate functional activity variations. The work described in this Chapter is centered on the presumed effect of synaptic scaling in the functional output strength of the network.

### 4.1.1 The role of synaptic scaling

The term synaptic scaling was coined in 1999 as a regulation mechanism of cortical neurons in response to changes in activity (Desai et al., 1999). Ten years later, it was clear that neurons could detect firing rate alterations through calcium-dependent sensors and synaptic scaling was demonstrated both *in vivo* and *in vitro* for different pyramidal neurons (Burgoyne, 2007; Turrigiano, 2008). Since then, it has been studied thoroughly by the physiological field to deeply understand its chemical pipeline and homeostatic role. It is currently a controversial matter whether upward synaptic scaling is a reaction to the suppression of glutamatergic neurotransmission release or directly an attempt

of spiking rate stabilization (fai Fong et al., 2015; Schaukowitch et al., 2017). Nevertheless, it has become clear that is an essential plasticity resource, as it is thought to be closely related with learning and memory access (Zenke et al., 2015), and thus it may be involved in neurological diseases (Borge-Holthoefer et al., 2011; Keck et al., 2013).

Despite the importance of synaptic scaling, a detailed characterization of its functional consequences on a living neuronal network is missing. Therefore, we took advantage of *in vitro* neuronal networks and our capacity to act on them by chemical means, to advance in this quest. The work described in this Chapter is centered on exploring whether synaptic scaling suffices to explain the observed activity–compensatory mechanisms in experiments in which we gradually weakened synaptic communication, compromised activity flow, and altered global network activity.

## 4.2 Activity modulation in clustered cultures

In the following experiments, we analyzed the dynamics of *clustered* neuronal networks while the connectivity strength among clusters was being reduced. The procedure was designed to capture dynamical changes and trigger possible homeostatic mechanisms within an enclosed system, where every node in the network is localized and the environmental conditions are attentively supervised.

To reversibly trail off synaptic transmission, we applied well–known pharmacological blockers that potentially evoke synaptic scaling (Wiegert et al., 2017) and examined the transient reaction of the neuronal population. Specifically, as we detail later, we used CNQX, an AMPA–glutamate receptor antagonist of excitatory synapses to progressively reduce excitatory communication. The silencing of activity to target specific roles has to be consistent in terms of timescales and side effects to avoid misleading assumptions.

### 4.2.1 Neuronal activity in clustered cultures

To study in detail the dynamical changes driven by progressive synaptic suppression, we focused on clustered cultures due to their rich repertoire of connectivity patterns, a repertoire that is much more interesting in terms of network functional organization than the simple all–or–none dynamics of homogeneous cultures. Clustered cultures were prepared from rat primary cultures (Figure 4.1A), and emerged as a self–organized process in which the absence of adhesive proteins in the glass substrate favored neuronal mobility and aggregation (Segev et al., 2003; Teller et al., 2015). By *day in vitro* (DIV) 4 upon preparation, aggregation shaped highly compact neuronal islands termed *clusters* that remained stable in position and size.

All samples were studied at DIV 8–12, a developmental stage in which the neuronal clusters exhibited a high rate of spontaneous activity, typically around 5 firings/min. Spontaneous activity was characterized by the coordinated activation of two or more clusters in a short time window (yellow outline in Figure 4.1 B), shaping a modular functionality that was dependent of the biochemical environment (Teller et al., 2014).

Each sample consisted of two twin cultures containing about 150 neuronal clusters each, isolated within two areas of 6 mm diameter, that is the maximum field of view of our current setup (Figures 4.1A–B). Spontaneous activity was monitored at high frame rates (50fps) through fluorescence calcium imaging using the Fluo–8 probe, as described in Section 2.5.2. Active clusters appeared as bright objects whose fluorescence intensity ramped up upon activation and decayed slowly afterwards.

### 4.2.2 Experimental pipeline

Since spontaneous coordinated activity is mostly mediated by the excitatory drive of AMPA–glutamate receptors, and synaptic scaling is displayed by central glutamatergic neurons (Turrigiano, 2008), we first fully

blocked NMDA and $GABA_A$ inhibitory receptors (with APV and bicuculine, respectively) to reduce activity modulations and simplify excitation parameters. Then, we chose the best looking isolated culture and conducted a 20 min recording to capture the initial state of the network. Next, the AMPA-glutamate excitatory connectivity was weakened through six increasing concentrations of the antagonist CNQX, with preset concentrations of [CNQX] (nM) $= 30, 60, 120, 300, 600, 1000$. CNQX was diluted in the recording solution (RS), the medium in which the culture is kept outside the incubator. For each concentration, activity was recorded for 15 minutes. Each step amplified the previous dose in a quasi–logarithmic manner, covering a wide range of dosages while keeping the total duration of the experiment short. Control experiments, consisting of identical manipulations but without the addition of CNQX, served to verify that the handling and duration of the experiment did not affect network stability. Finally, to investigate whether the neuronal cultures were able to recover basal activity, samples were washed off with fresh RS at the end of the recording session, NMDA receptors and $GABA_A$ inhibitory receptors blockers applied again, and activity monitored for additional 20 min.

The clusters were easily identified in the fluorescence image as ROIs and the changes in the gray–scale intensity within the delimited areas were registered as fluorescence signals. As described in the methodology, these fluorescence traces served to determine the onset activation times of each cluster. The capability of this experimental setup to access the entire system made it unique to investigate the action of perturbations, their impact on network functional organization and whether they are reversible or not.

An example of the impact of CNQX on network spontaneous activity is shown in Fig. 4.1C. Here, the fluorescence traces of four representative clusters are depicted for gradually higher CNQX levels. Without blockade, all four clusters exhibited a rich activity with strong coordination (yellow band). As CNQX was applied, the level of activity and coordination swiftly decreased,

and for strong dosages the clusters either fired weakly and independently or became silent.

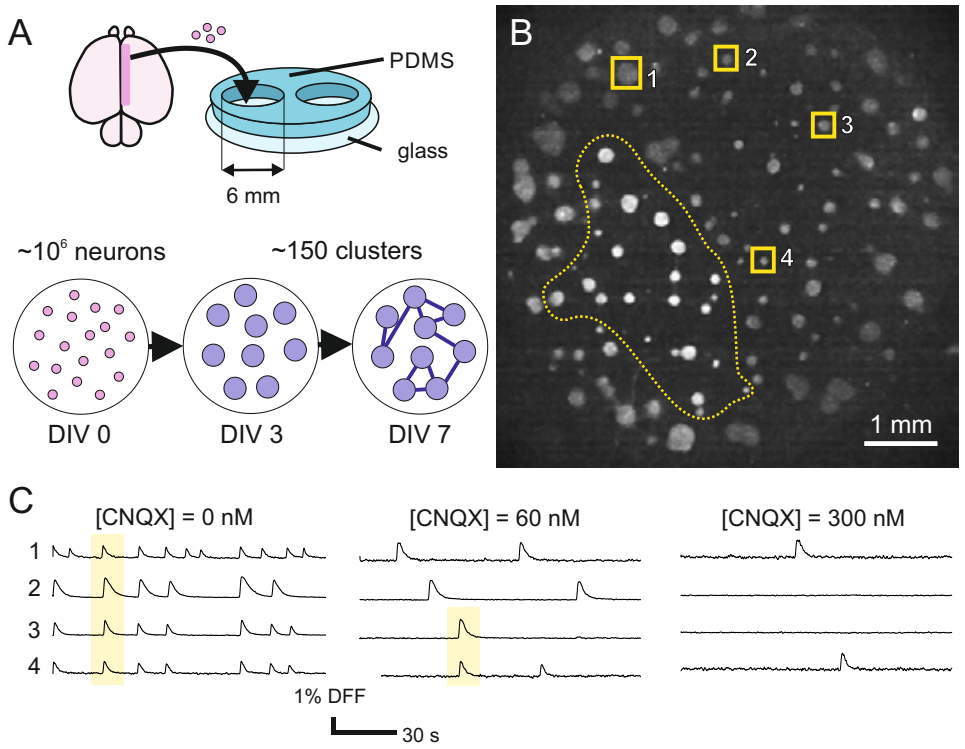


**Fig. 4.1 Clustered neuronal cultures.** (A) Schematic preparation of clustered neuronal networks. Dissociated rat cortical neurons were plated on a 6 mm diameter PDMS wells. The absence of adhesive proteins facilitated neuronal aggregation, giving rise to an assembly of neuronal islands (*clusters*) by *day in vitro* 7 that exhibited rich spontaneous activity. (B) Fluorescence image of a typical neuronal culture. Circular objects are neuronal clusters. Labels highlight the location of 4 clusters whose fluorescence traces are shown later. (C) Representative fluorescence traces for 4 clusters for gradually higher levels of the AMPA–glutamate receptor antagonist CNQX. Sharp increases of the signal correspond to activity events.Yellow boxes illustrate episodes of coordinated activity. The overall activity of the clusters decreases with CNQX as a result of the reduced excitatory drive.

## 4.3 Synaptic weakening alters functional organization

Activity data was analyzed to compute the effective connectivity of the networks, using the time–delays method as a measure of inter–cluster functional coupling (see Section 3.2.1), an approach that we showed appropriate in previous studies (Teller et al., 2014, 2015). These effective networks, weighted and directed, allowed us to quantify the degree of whole–network alterations upon CNQX action in terms of network properties (see Section 3.3). For this study, we investigated a total of 14 cultures. Of them, and after analysis, we selected 8 cultures matching initial conditions of network size $N = 133 \pm 15$ and link density $D = 0.27 \pm 0.04$ and another 4 control samples.

### 4.3.1 The widespread impact of global blockade

To get started, we observed how the fall of spontaneous activity and the rupture of coordinated activity between clusters impacted the entire network. This process is shown in Figure 4.2 for representative control and perturbed cultures. For the latter, he emergence of smaller functional communities for [CNQX] = 60 nM appeared as an increase in modularity that progressed until the clusters became isolated. The network at [CNQX] = 1000 nM is not shown since, for this concentration, every node in the network was disconnected from the others.

The inferred effective networks echoed the reduction of activity and inter–clusters communication. Figure 4.3 compares the raster plots of activity (top row) with the inferred effective connectivity matrices (bottom row). For the raster plots, we note that each dot marks the activation timing of every cluster, a data that is directly obtained from the analysis of the fluorescence signal. The rasters clearly illustrate the loss of coordinated activity and the gradual emergence of groups of clusters that tend to fire together, shaping small effective communities that are also visible in the effective connectivity

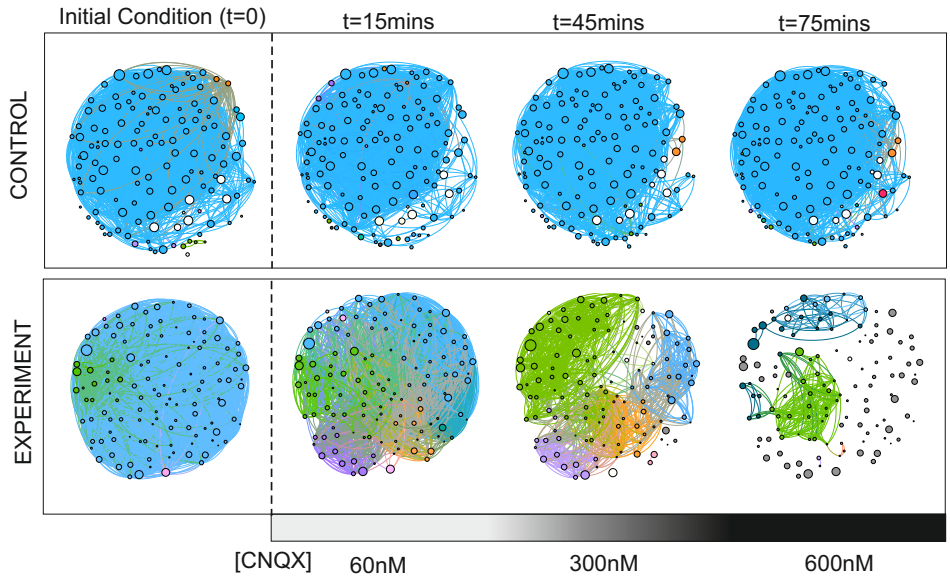


**Fig. 4.2 Effective connectivity maps of control and perturbed experiments.** *Control* samples (top) consisted in the analysis of a given neuronal culture at different time intervals. These controls experienced the same experimental pipeline as perturbed ones, but only $GABA_A$ and NMDA receptors were blocked. Clearly, for controls, the community organization, firing rate and strength between clusters remained virtually constant despite of the long time period. For a perturbed representative *experiment* (bottom), communities clearly emerged as CNQX took action, increasing the overall modularity of the network.

matrices. Communities become smaller as degradation progresses, until they disappear for [CNQX] $= 600$ nM or larger.

To better understand the behavior of the network we note that, according to previous studies (Soriano et al., 2008), the fraction of free receptors $c$ that are not bound to the antagonist CNQX and that are therefore able to activate the synapse is given by $c = 1/(1 + [\text{CNQX}]/K_d)$, where $K_d = 300$ nM is the dissociation constant of CNQX. Thus, in the sequence of raster plots, [CNQX] $= 0$ ($c = 100\%$) shapes a strongly coherent dynamics in which most of the clusters coactivate at unison, a feature that stands for strong synaptic coupling among clusters. Whole network coordination breaks off even for small perturbations with [CNQX] $= 60$ nM ($c = 83\%$), shaping a dynamics that is characterized by the coactivation in small groups of strongly

bound clusters. Coactivation sizes reduce as CNQX increases, although some groups still maintain coordinated activity even for relatively large doses of [CNQX] = 600 nM ($c = 33\%$). We typically observed that activity fully stopped at [CNQX] $\gtrsim$ 1000 nM ($c \lesssim 23\%$ free synapses). Every network exhibited a similar qualitative trend, although the structure of coordinated activity and its changes upon degradation depended on the cluster–to–cluster wiring details in each realization.

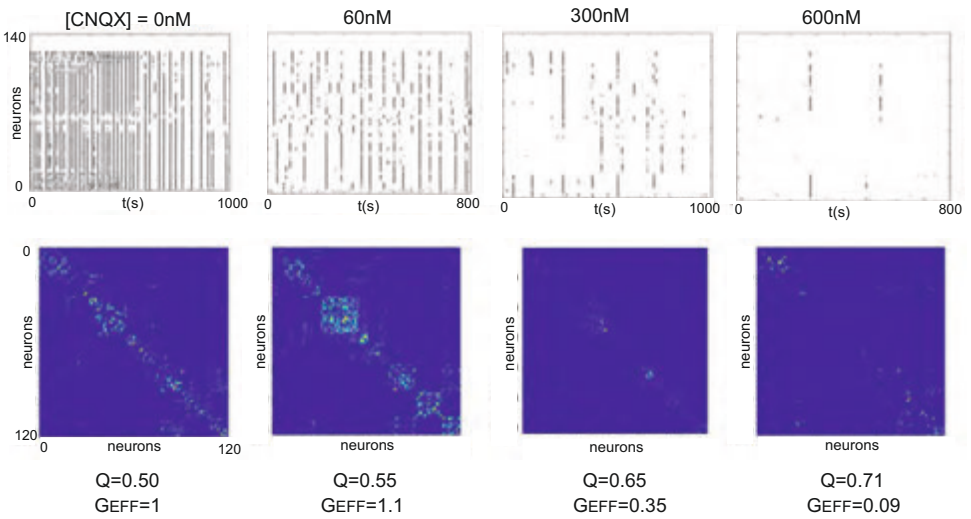


**Fig. 4.3 Network activity and functional connectivity upon degradation.** The top plots show the raster plots of spontaneous activity for a representative network. The bottom color maps show the effective connectivity matrices, weighted and directed. The brighter the color, the higher the connectivity weight among two clusters. Matrices are ordered according to the functional communities at [CNQX] = 60 nM. $Q$ provides the community index, and $G_{EFF}$ the global efficiency normalized with respect to the value at [CNQX] = 0. For this representative sample, the $G_{EFF}$ increased by 10% at [CNQX] = 60 nM, to steadily decrease afterwards.

From the inferred effective networks we extracted two major measures, namely the *community statistic* $Q$ (see Section 3.3.5), which informs about the degree of fragmentation of the network into functional communities, and the *global efficiency* $G_{\mathrm{EFF}}$ (see Section 3.3.2), which represents the capacity of the network to operate as a whole. For clarity, the global efficiency was

always normalized with respect to the value of the unperturbed network at [CNQX] = 0. As a global trend (Figure 4.3, bottom values), $Q$ progressively increased as CNQX grew, signaling the gradual fragmentation of the network until activity ceased. Such a fragmentation was expected to be translated into a gradual decrease of $G_{\mathrm{EFF}}$, since intercommunication between clusters at a network level dropped. However, $G_{\mathrm{EFF}}$ increased by $10-80\%$ with respect to the initial condition for moderate CNQX concentrations, to later fall as expected. This abrupt increase in $G_{\mathrm{EFF}}$ was termed *hyper–efficiency* (HE) and signaled a non–intuitive scenario in which damage enhanced broad network communication.

The data of the representative experiment of Figures 4.2 and 4.3 was a general trend that was qualitatively repeated across cultures. In all cases, CNQX caused a fragmentation of the network into communities together with a sudden increase of $G_{\mathrm{EFF}}$ for moderate CNQX levels.

### 4.3.2 Degradation level *d* and global efficiency curves

The global efficiency of the network reflects, on average, the optimization of signal spreading for fast transmissions throughout the system. Therefore, the follow–up of its evolution during activity suppression serves as a resilience measure to quantify failure, in the sense that an extremely low global efficiency turns the system inoperative.

Although all cultures shared common initial traits in terms of firing rate, number of nodes and basic network properties, the dose of CNQX at which the networks started to react slightly differed from one another. Indeed, the onset of functional alterations never occurred at the first CNQX dosage, but after a minimum concentration was reached, and that varied from experiment to experiment. The same occurred with the CNQX concentration at which activity ceased. Thus, for the experiments to be comparable, we considered a *reference* value $[\mathrm{CNQX}]_{\mathrm{ref}}$ above which dynamic alterations were detectable, and a *maximum* $[\mathrm{CNQX}]_{\mathrm{max}}$ at which activity fully ceased (Figure 4.4A).

Data was rescaled according to these points to obtain the global efficiency as a function of the *degradation level d* (Figure 4.4B). Despite the different sensitivity to CNQX across realizations (i.e. different $[\mathrm{CNQX}]_{\mathrm{ref}}$ and $[\mathrm{CNQX}]_{\mathrm{max}}$), practically all experiments showed a consistent and clear peak in global efficiency at $d \simeq 0.15$ that was nonexistent in controls.

In short, the experimental curves for the evolution of the global efficiency as a function of CNQX were normalized and aligned to facilitate the average over network realizations. For each experiment $n$, the *degradation level* at step $k$, $d_k^{(n)}$, was defined as

$$d_k^{(n)} = \frac{[\mathrm{CNQX}]_k^{(n)} - [\mathrm{CNQX}]_{\mathrm{ref}}^{(n)}}{[\mathrm{CNQX}]_{\mathrm{max}}^{(n)}}, \tag{4.1}$$

where $[\mathrm{CNQX}]_{\mathrm{ref}}$ is the CNQX concentration just before observing any alteration in the network, and $[\mathrm{CNQX}]_{\mathrm{max}}$ is the maximum concentration before full silencing of the network. With this normalization, the degradation level $d$ varied between 0 (no alteration to the network) to 1 (full silencing of activity and complete effective network breakdown). Data outside these bounds was disregarded.

The global efficiency $G_{\mathrm{EFF}}$ computed from a given effective network of an experimental realization $n$ was denoted as $\tilde{G}^{(n)}$. For the sake of contrasting samples, each global efficiency curve $\tilde{G}^{(n)}(d)$ was scaled as $G^{(n)}(d) = \tilde{G}^{(n)}(d)/\tilde{G}_{\mathrm{ref}}^{(n)}$, where $\tilde{G}_{\mathrm{ref}}^{(n)}$ is the global efficiency measured at the reference step $[\mathrm{CNQX}]_{\mathrm{ref}}$. Such a scaling was adequate to better appreciate the changes of the global efficiency with respect to the unperturbed scenario. The set of resulting experimental curves were then interpolated as 100 equidistant points using a cubic interpolation that preserved the shape of the curves as well as the local and global extrema. Data was later averaged among the $n = 8$ experimental realizations (Figure 4.4B).

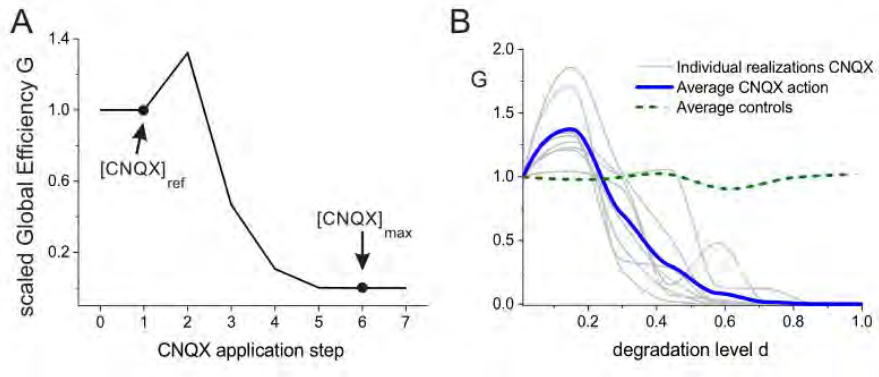


**Fig. 4.4 Experimental data analysis and degradation level $d$.** (**A**) Definition of $[\mathrm{CNQX}]_{\mathrm{ref}}$ (CNQX step before any damage occurs) and $[\mathrm{CNQX}]_{\max}$ (step at which activity fully ceases). (**B**) Alignment of the 8 experimental realizations (gray curves), their average (thick blue curve), and its comparison with 4 averaged controls (dotted green curve). The global efficiency $G$ is shown scaled, so $G = 1$ corresponds to no damage. Hyper–efficiency occurs by $d \simeq 0.15$ and leads to an increase of $G$ by 30%.

## 4.4 Numerical models for network degradation.

We carried out numerical simulations to understand the origin of hyper–efficiency in the CNQX–perturbed experiments. In the simulations, the networks used for degradation were the experimental effective networks just before any alteration occurred, i.e. the ones obtained at $[\mathrm{CNQX}]_{\mathrm{ref}}$ ($d = 0$). The corresponding connectivity matrices, denoted $\mathbf{A} = \{a_{ij}\}$, were by construction directed and weighted, with weights in the range $[0,1]$. For each network, two connectivity degradation schemes were compared, namely *percolative degradation* (PD) and *synaptic scaling degradation* (SSD). As sketched in Figure 4.5, the two models are:

**Percolative degradation** (PD). This model progressively deletes the effective links whose weights are below a threshold $t_H \in [0,1]$. Thus, for each simulation step $k$, the deleted nodes are those that fulfill $a_{ij} < t_H^{(k)}$, with $t_H^{(k)} = \{1/N, 2/N, ..., k/N\}$ and $N = 100$ steps.

**Synaptic scaling degradation** (SSD). his model is based on the percolative degradation but with the crucial additional rule that, upon removal of an output link from a node, all weights of the surviving output links of the node are locally rescaled by its output strength. Thus, if the initial network is given by $a_{ij}^{(0)} \equiv a_{ij}$, each degradation step $k$ consists in the deletion of the links fulfilling $\left\{ \exists\, a_{i,j}^{(k-1)} \mid 0 < a_{i,j}^{(k-1)} < t_H^{(k)} \right\}$ followed by a renormalization of locally surviving links, so that $\sum_j a_{ij}^{(k)} = 1$. As in the previous model, $t_H \in [0,1]$ with $t_H^{(k)} = \{1/N, 2/N, ..., k/N\}$ and $N = 100$ steps.

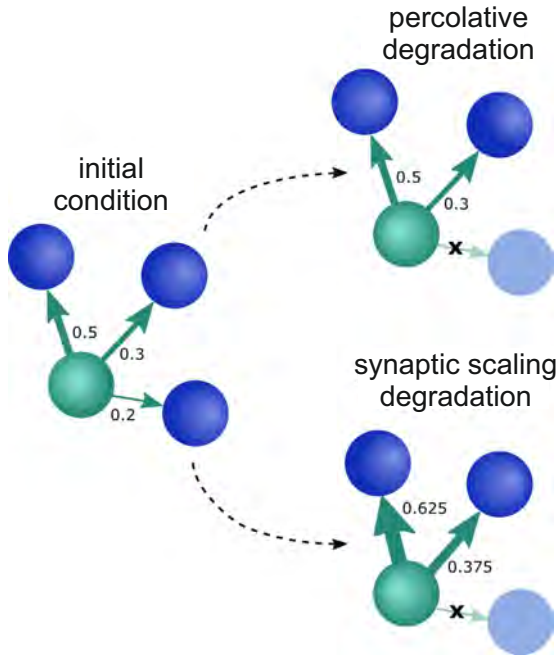


**Fig. 4.5 Schematic representation of the two degradation models.** Both models operate on the same network (**left**), but behave differently. In the examples, the applied threshold for removal is $t_H = 0.25$. (**Top**) Percolative Degradation (PD): the bottom connection is removed, disconnecting the corresponding neuron. Surviving connections remain unaffected. (**Bottom**) Synaptic Scaling Degradation (SSD): the same connection is removed, but the surviving out–going connections are rescaled so that the total out–strength of the node is 1. Thus, surviving links become stronger.

## 4.5 Numerical models and experimental data

In the above models, PD just reflects a percolation transition where the link blockade spreads through the system. Since our effective networks are weighted, links are not equally susceptible of being targeted, instead weaker links are more vulnerable while the strongest remain unmolested. This PD scenario is simple and inspiring, but does not capture the reality of biological networks, in which dynamical adjustments immediately come forth when perturbations appear. Therefore, the SSD model is the simplest scenario we could think of that takes into account this dynamically–induced effects, considering synaptic scaling as a major drive of this plasticity. To accurately compare both models with the experimental data, we needed an additional ingredient, namely the link between the *experimental* degradation level $d$ and the *numerical* iteration threshold $t_H$.

### 4.5.1 Relation between degradation and iterative thresholds

We emphasize again that both models acted on the same initial, unperturbed networks derived from the experimental recordings at $[\mathrm{CNQX}]_{\mathrm{ref}}$, and applied a series of rules for the deletion of links. PD consisted in the gradual removal of effective links from weaker to stronger according to a threshold $t_H$, while SSD consisted in the same link removal but adding the strengthening of surviving links.

In order to compare the experiments with the models, it was necessary to set up an adequate relation between degradation $d$ and threshold $t_H$. Two relations for $d(t_H)$ were considered, termed *linear* and *biologically realistic*. The linear approach just considered $d = t_H$. The biologically realistic approach assumed that $t_H$ was proportional to the fraction of free receptors $c$, which in turn depended on [CNQX]. The relation between $t_H$ and $d$ was obtained in two steps. First, the relation $t_H([\mathrm{CNQX}]) = (1 + [\mathrm{CNQX}]/K_d)$,

where $K_d = 300$ nM, was used to transform drug concentration to the capacity of a neuron to pass the signal to other neurons, as described by Soriano et al. (2008). And, second, $t_H(d)$ was constructed following Equation (4.1), i.e. according to the reference points observed experimentally.

### 4.5.2 Degradation model with synaptic scaling explains hyper–efficiency

The outcome of the two models, and their comparison with experimental data, is shown in Figure 4.6A. Percolative degradation led to a fast decay of the global efficiency $G$ and a total loss of connectivity for $d \simeq 0.18$, a relatively low degradation level that is clearly not presented in the experiments. On the contrary, synaptic scaling degradation not only captured the experimental hyper–efficiency for low $d$, but also portrayed a much slower decay of $G$ on $d$ for strong damage.

Although the SSD model quantitatively matched the experimental hyper–efficiency and the $G(d)$ decay shortly thereafter(Figure 4.6B), it could not reproduce the entire experimental behavior. We provide two reasons for this mismatch. The first reason is grounded on the neuronal dynamics perspective: as the capability of the biological network to fire spontaneously is reduced, i.e. as the firing rate decays, the effective coupling between clusters is rendered as weaker links. This property is not incorporated in the model, and would require a substantial investigation of the relation between cluster–to–cluster firing occurrences and the strength of the effectively links to reliably incorporate it. The second reason is that, from the SSD model construction perspective, the surviving links in each degradation step are gradually stronger until all surviving links are of weight 1, shaping a network that will effectually remain stable –with $G$ approximately constant– for large $d$, only collapsing at $d = 1$. Thus, based on these considerations, we argue that synaptic scaling suffices to explain hyper–efficiency *only* in the context of small perturbations, not for strong blockades.

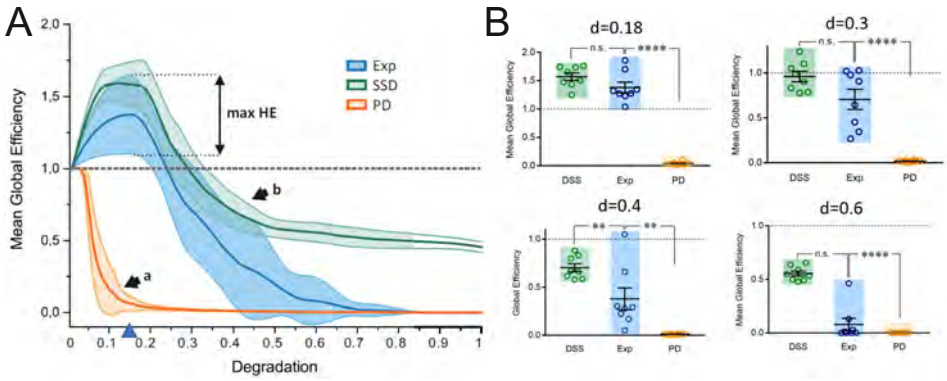


**Fig. 4.6 Comparison of degradation models and experiments.** (**A**) The evolution of the global efficiency $G$ (scaled and averaged among realizations) as a function of $d$ is compared between experiments (blue) and numerical models (PD, orange; SSD, green). PD portrays a fast–decaying behavior that fails at capturing any experimental trend, approaching $G \simeq 0$ at a value of $d$ in which the experimental behavior corresponds to hyper-efficency ('a' point). SSD, on the contrary, captures the observed hyper–efficiency at $d \simeq 0.15$ (blue arrowhead) and renders a $G(d)$ that decays gently and similar to the experiments up to $d \simeq 0.5$ ('b' point) . (**B**) Comparison of datasets at representative $d$ values, showing the incapacity of PD to approach the experiments, and the good behavior of SSD for weak damage, where the difference between experiment and model are non–significant. Each dot corresponds to a network realization. ** indicates p<0.005, and *** indicates p<0.001 (Student's t–test).

To verify that the existence of synaptic scaling was not an experimental artifact, we compared the evolution of CNQX–dosed networks with control ones that were prepared and manipulated identically. Figure 4.2 compares the connectivity maps of a control and a perturbed network. The latter corresponds to the data of Figure 4.3. Along the degradation experiment, which lasted 75 min, the control culture retained the same functional traits across the network with small variations, while the degraded one significantly changed, portraying the functional communities outlined above and that varied in size and structure as blockade progressed.

The functional maps of Figure 4.2 also helped picturing the CNQX degradation process in terms of the spatial arrangement of the clusters. The maps showed that the functional communities were physically compact, i.e. they were constituted by groups of adjacent clusters. This indicates that the clusters

typically connected to their immediate neighbors upon network formation, and that the physical location of the functional communities was preserved but reduced in size.

## 4.6 Altered connectivity after CNQX washout

As a final analysis, we investigated the network functional connectivity after recovering the biochemical conditions of the initial network, i.e. after washing off CNQX. As shown in Figure 4.7A, all clusters regained activity and rebuilt functional communities, indicating that no irreversible damage was caused in the network upon CNQX application. However, we note that the functional connectivity maps were, in general, slightly different from the initial condition –prior to the degradation process–.

To quantify the extend of functional changes after washing off CNQX, we computed the density of links $D$, defined as the links that a network contains with respect to all possible links that can be formed. $D$ was computed for each analyzed culture, and then the distribution of $D$ values for the 8 cultures was plotted to compare the initial and recovered (washout) scenarios. As shown in Figue 4.7B, the recovered networks exhibited broader and smaller values of $D$, indicating an overall reduction of inter–cluster interactions. We conjecture that the incapacity of the network to fire for high CNQX values accentuated plastic mechanisms in an attempt to recover activity, which translate into altered functional organization at wash off.

Based on these results, we humbly hypothesize that the effective tuning of the network requires longer periods of time to recover a configuration previously achieved during several days *in vitro*. Additionally, the inner hyperactivity of neurons trying to compensate the blockade of transmission for extensive intervals could cause a fatigue phenomenon, carrying a decrease in the probability of neurotransmitter release. Comparing with the unaffected controls, the exhaustion of the neuronal culture may be also responsible

of a weaker recovered network. To corroborate this it would be necessary the use of genetically encoded calcium indicators to follow the functional configuration of the same culture during several days after the end of CNQX action and wash off. Although these experiments are planned, they could not be completed at the moment of writing this thesis.

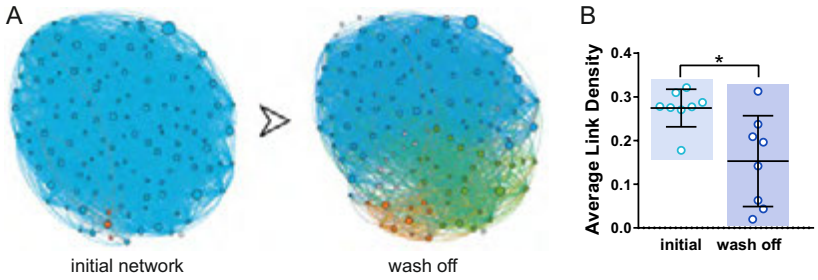


**Fig. 4.7 Network after washing off CNQX** (**A**) Illustrative effective networks at the beginning of the experiment (left) and after after washout (right). A new community appeared at the bottom for the latter. (**B**) Corresponding comparison of link density $D$, showing a significant decrease, though weak, of $D$ after wash out. Each point is an experimental realization, and * indicates $p<0.05$ (Student's t–test).

## 4.7 Discussion

In this study we investigated the action of CNQX, an antagonist of excitatory receptors, on the activity and functional organization of clustered neuronal cultures. In our approach, the connectivity among clusters was gradually weakened, affecting dynamics (and in turn effective connectivity) but the physical connections were left intact.

Progressive application of CNQX induced a gradual reduction of inter–cluster coupling that, surprisingly, was not accompanied by a fall of network functionality and information flow, but by a sudden increase of it. We used the Global Efficiency $G$ as a measure of information flow capacity across the network for different degradation levels $d$. The *hyper–efficiency* of $G$ was transient, but significantly strong and reproducible among experimental

realizations. Indeed, some experiments reported an increases of about 180% upon degradation, suggesting the advent of a highly optimal network communication scenario. By analyzing the data in the context of degradation models, we concluded that synaptic scaling mechanisms were at play, in which the loss of weak communication pathways reinforced already existing strong ones, leading to an overall sudden facilitation of network communication.

Our study shows that plastic mechanisms are continuously at play in neuronal networks. Different experimental investigations have pinpointed the tendency of neuronal circuits to maintain a target level of activity, and our study illustrates that the response to a perturbation may trigger substantial changes at functional levels. This is important in the context of studies that model approach perturbations and damage purely in the context of the distribution of connections. Models of degradation and damage in neuronal networks often disregard this plasticity, which we prove is central to predict an accentuation or a decay in the dynamics and communicability traits of the network.

The brain can react to pathological perturbations using compensation mechanisms, striving to maintain a homeostasis performance. Our observed hyper–efficiency shares similarities with the hyper–priming phenomena observed in cognitive studies in Alzheimer's patients (Borge-Holthoefer et al., 2011). The consequences of damaging the system and its subsequent recovery serve to simulate pathological scenarios. Our work is thus an attempt to study experimentally and numerically the emergence of alterations when a controlled and reproducible disturbance is applied. It also aims to find patterns amidst a given event and the reaction it causes, to determine vulnerabilities and strengths with respect to disease and dysfunction. We believe that our work will be a motivating scenario to study network changes (beyond hyper–efficiency) upon dynamic alterations, including hyper–priming, superexcitablilty, or epileptic states.

# Chapter 5

# Results II: MESOBRAIN Challenges and Strategies

MESOBRAIN is a Future Emergent Technologies project (FET) under the Horizon2020, one of a set of high–tech high–risk research plans that aimed to make great technological leaps before the year 2020. The core of the MESOBRAIN project is to build tunable 3D neuronal networks derived from human iPSCs, to ultimately construct custom human-derived cortical columns *in vitro*, that could be applied for regeneration in disease and trauma.

The capacity to tune the physical organization of a neuronal network requires to position neurons in predefined locations and to direct their activity propagation along specific paths. In this Chapter, we first recapitulate the line of action that we implemented to select the best biomaterial to shape 3D networks, to later describe the different manipulation strategies to convert basic polymer structures into structural supports for neurons.

## 5.1 MESOBRAIN overview

Although the idea of building tunable 3D networks seemed an elegant an promising proposal for the biomedical community, its actual implementation turned out to be a Pandora's box; A source of unforeseen difficulties. One has to take into account not only the physiological needs of neurons, but also the constraints of a structural platform (*scaffold*) that must provide proper guidance and attachment.

Lastly, the medium that engulfs the entire system can be either liquid culture medium or semi–solid hydrogels that grant additional support. Indeed, 3D block cultures on solely hydrogels have been widely studied (Caliari and Burdick, 2016), but the nature of these materials is such that their architecture and points of interaction with seeded neurons cannot be predicted or controlled, leading to essentially randomly assembled neuronal networks. Therefore, the goal of the MESOBRAIN initiative was to develop new technological concepts to control both neuronal positioning and directionality through scaffolds of manifold shapes.

The MESOBRAIN endeavor was focused on two main aspects: the optimal material for building scaffolds and a reproducible design for culturing iPSCs on engineered 3D substrates. The former implied the exploration of available materials to evaluate their physical properties and biocompatibility. The latter required a well-established protocol for the culture of hiPSC and the mass–production of scaffolds, carefully designed to accomplish healthy neuronal networks.

The construction of the 3D platforms was devised by two approaches: (i) a stackable set of 2D scaffold layers combined with soft hydrogels in between and (ii) vertical single–piece scaffolds. Scaffolds provided an skeletal support where neurons could be placed and guided to connect to one another, while hydrogels are porous materials that facilitate the arrival of nutrients, $CO_2$ and $O_2$, acting as the extracellular matrix (ECM) in actual brain tissue.

The targeted breakthrough was the production of 3D neural networks comprised of neurons growing at specific points on high–tech fabricated 3D scaffolds, manufactured using a relatively new technique known as two-photon polymerization (2PP). Ultimately, the desired structure should emulate a cortical column with different layers, incorporating excitatory and inhibitory neurons as well as astrocytes derived from human neural progenitor cells.

## 5.2 Proposed biomaterials for printing structures

Initially, four synthetic materials, extensively detailed in the literature, were chosen based on their applications in biomedicine and nanoengineering, named PEDOT (Wang et al., 2018), Ormosil (Sima et al., 2013), PLA (Radakisnin et al., 2015) and PEG–DA (Cha et al., 2014). Conversely, D–CLEAR was a late addition to the list due to its promising features. The five materials are described below.

1. Poly(3,4-ethylenedioxythiophene) (PEDOT).
2. Organically modified silicon (Ormosil).
3. Polylactic acid (PLA).
4. Polyethylene Glycol Diacrilate (PEG–DA).
5. Dental–L–Clear (D–CLEAR).

PEDOT film is a dark–colored conductive polymer, easily combined with electrodes, that can take advantage of the electrically active nature of neurons to promote cell growth through electrical stimulation. However, its opacity and brittleness made it unfeasible for calcium imaging and long-term culture.

An organically modified silicon (Ormosil), a degradable polylactic acid (PLA) and a common hydrophilic crosslinking monomer, polyethylene Glycol Diacrilate (PEG-DA), showed good transparency in bright field, but displayed different levels of autofluorescence due to their intrinsic photo-initiators.

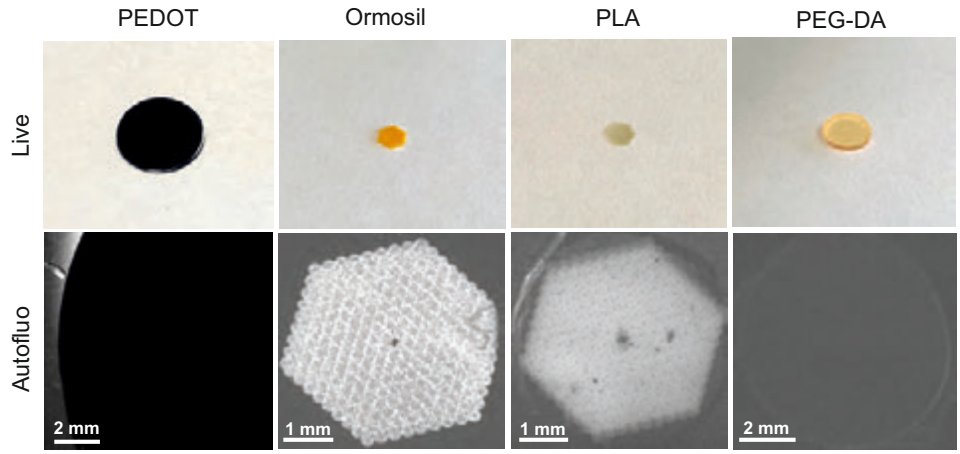


**Fig. 5.1 The four initially considered biomaterials.** (**Top row**). Representative live images of the different samples. PEDOT samples were 10 mm in dimameter, Ormosil and PLA were constructed as two layers of cylinders fitted on an hexagon 4 mm in diameter, and PEG-DA pellets were a flat surface 6 mm in diameter. (**Bottom row**). Fluorescence view under blue light excitation, green light emission. Although exposure times were varied to avoid image saturation, PEDOT was totally opaque, PLA and Ormosil showed large autofluorescence, and PEG-DA showed moderate autofluorescence levels.

Excluding PEDOT, PEG-DA was the least autofluorescent (Figure 5.1), but its brightness was sufficient to mask the spontaneous activity of neurons on typical experimental settings of light intensity and exposure times. Thus, we centered our efforts on eliminating this effect. We first attempted to photo–bleach the material, i.e. to irreversible silence its fluorescence molecules, by using a laser scanning microscope, but the idea proved inadequate due to the collateral damage caused on the material, which became brittle and unusable. Then, we tried the use of different photoinitiators for curing the material, being IR1959 the one with best transmittance at short wavelengths and lowest fluorescence emission.

The improvement of PEG-DA IR1959 was noteworthy but still not optimal for blue excitation light, and prominent at other wavelengths, which could totally alter immunostaining images. For these reasons, and after 6 months of abundant tests, the MESOBRAIN consortium jumped into the aforementioned

D-CLEAR (Dental LT Clear Resin, Formlabs), a biocompatible resin for long–term applications with good fracture and wear resistance, commonly used for printed orthodontic appliances, but never before for cell culture. It has excellent optical transparency and not known autofluorecence (Figure 5.2). Testing neuronal compatibility was the next big step.

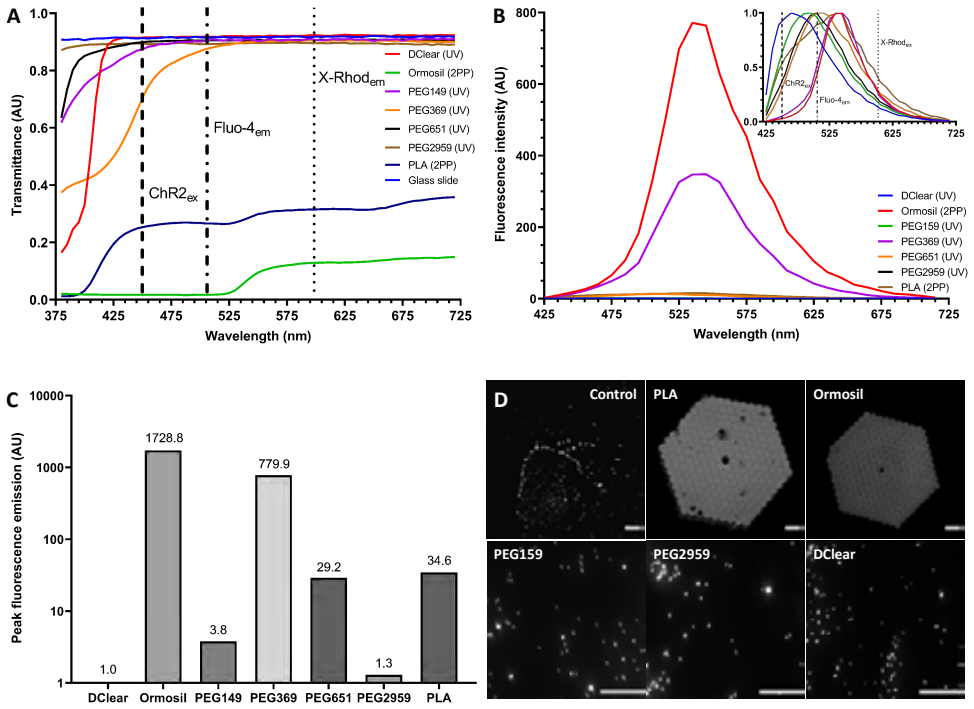


**Fig. 5.2 Optical characteristics of candidate materials.** **(A)** Transmission spectra of candidate biomaterials over 380 – 720 nm in 5 nm steps. ChannelRhodopsin Chr2/H134 excitation wavelength (450 nm) and calcium indicators Fluo-8 AM (506 nm) and X-Rhod-1 AM (602nm) emission wavelengths are marked to represent widely used examples of optical interrogation tools for neuronal function. **(B)** Interpolated spectra of fluorescence emission intensity from 405 nm laser–excited candidate materials, recorded from 425 – 705 nm, with a spectral bandwidth of 10 nm. Inset, normalized graph highlighting emission peaks. **(C)** A normalized comparison between candidate materials to determine relative auto-fluorescence emission using maximal values. **(D)** Images of candidate material structures placed over green fluorescent beads and imaged using 405 nm laser excitation. Scale bars are 50 $\mu$m.

## 5.3 Scaffolds viability with hiPSCs

Two materials, PEG-DA and D-CLEAR, were used to analyze the development of hiPSC cells on scaffolds and study the formation of functional networks. Holed pellets made by UV projection lithography served to test the different materials as potential scaffold components. PEG-DA and D-CLEAR pellets (ø = 6 mm, 150 $\mu$m thick) with 16 holes (ø = 200 $\mu$m) were fitted on top of glass coverslips using PDMS molds with ø = 6–6.5 mm pierced cavities (Figure 5.3 A).

We performed biocompatibility tests at our sister facilities at Hospital Clinic (Barcelona) with the cell line 33Qn1, extensively used hiPSCs for experiments in medicine with a well established protocol (Telezhkin et al., 2016). Neurons grew healthy in both materials during 5 weeks, forming connections on top on the scaffold, on the walls of the holes and on the bottom glass (Figure 5.3 C). Unfortunately, we observed that the surface of PEG-DA ended textured after fabrication, i.e. with abundant wrinkles, that hindered the focus and detection of cells in bright field. Later on, by comparing these results with the cell line AX-0015 from our MESOBRAIN consortium partner Axol Bioscience, we observed similar results.

The wrinkled surface of PEG-DA IR5969 and its residual autofluorescence, still too high for fluorescence calcium imaging, left D-CLEAR as the best and final candidate for scaffold construction. We recorded activity on cells growing on flat D-CLEAR discs (Figure 5.3B), verified their healthy maturation (Figure 5.3D) and extracted their fluorescence traces.

Data was acquired at Hospital Clinic using the fluorescence probe Fluo-8-AM to detect activity with the same protocol as at Soriano's Lab at the Physics Faculty. As illustrated in Figure 5.3E, calcium transients characteristic of neuronal activity were clear, proving the biocompatibility of the material.

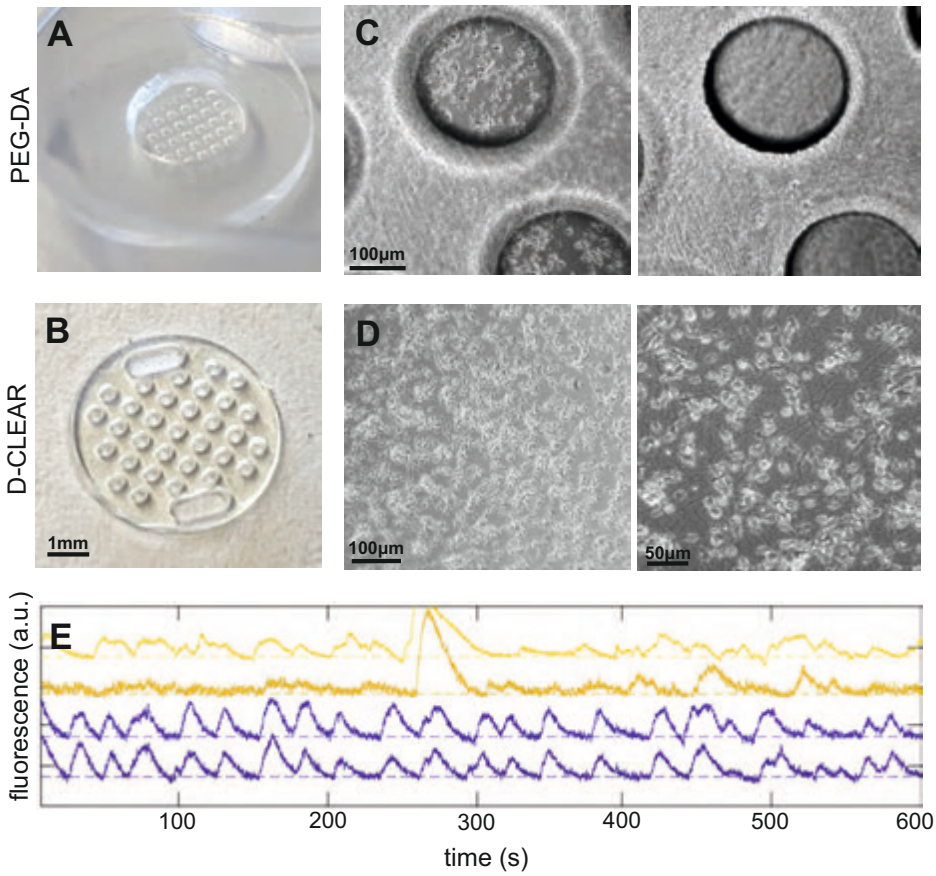


**Fig. 5.3 Biocompatibilty of 'short–list' candidate materials.** **(A)** PEG-DA IR2959 scaffold encapsulated on PDMS and attached to a glass coverslip. **(B)** D-CLEAR scaffold with handles to build stacks. **(C)** Detail of hiPSCs growing on glass (left) and on the top of PEG-DA (right). **(D)** Detail of hiPSCs growing on D-CLEAR scaffold pellets. It can be appreciated that D-CLEAR surface is smooth without the roughness seen in PEG-DA samples. **(E)** Calcium activity recordings of individual cells with Fluo-8 on D-CLEAR scaffolds, from four representative regions of interest.

## 5.4 3D designs: one step closer to cortical columns

As stated before, the progress within the MESOBRAIN project resulted in two parallel strategies for the construction of 3D tunable neuronal networks: (i) a vertical assemblage of scaffolds, separated by hydrogel stratum or rigid pillars; and (ii) a printed single–piece construction that served as a structural frame.

For the stackable design, two strategies were implemented. The first one considered the combination of two or more holey pellets, such as those in Figure 5.3B, to shape a vertical 3D platform (Figure 5.4A). The pellets themselves represented the rigid polymeric part of the composite structure, yielding the stability of the 3D platform and enabling vertical, level–to–level interconnection in a controlled manner. Hydrogel inserts, placed between the hollowed pellets, took the role of an ECM–like soft millieu to allow cell interconnectivity between pellets.

An updated version of the stackable design disregarded the use of hydrogels by incorporating tiny 2PP step pyramid–like spacers (not shown), that served as basic staircases for neuronal projections to connect in 3D through the different layers (Figure 5.4B). By using this method, the height of the finished stack is minimized, thus the vertical connectivity is shorter, ruling out the use of hydrogels and fitting the space limitations of the light–sheet microscopy setup at ICFO. Additionally, the used of holders allowed us to orientate the samples at 45 degrees, in accordance to the scanning direction of the setup (Figure 5.4C). Another fundamental piece, the ‘stopper’, is responsible to keep the scaffolds from detaching during handling and media exchanges.

After defining the final design of the stackable system, it was necessary to carry out various parameter investigations in order to achieve the optimum structural geometry and establish the build–up process. The inclusion of electrodes (Figure 5.4D) is a preview of future experiments based on recording simultaneously calcium transients and electrical activity.

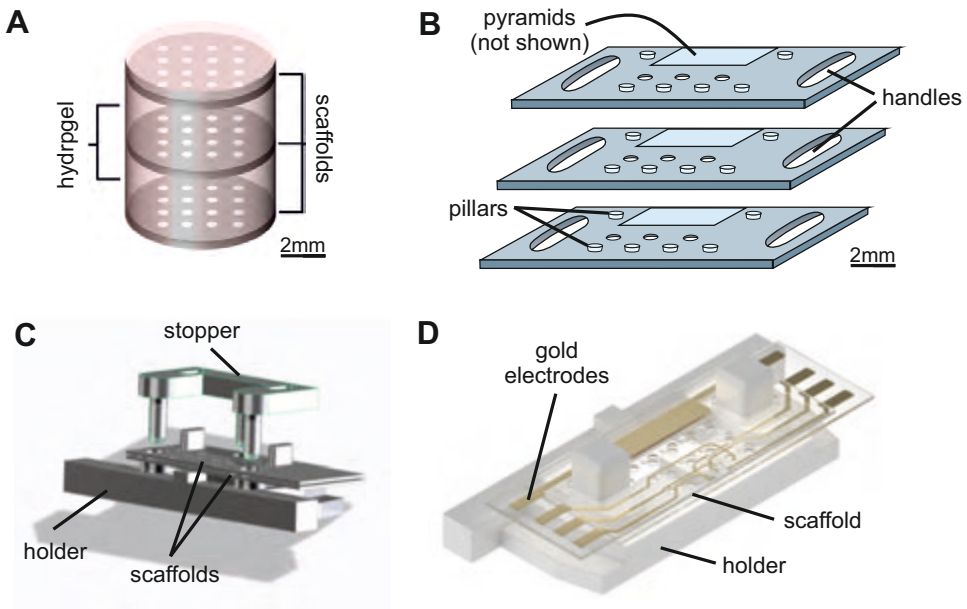


**Fig. 5.4 Stackable scaffolds designs.** (**A**) First concept of holed pellets separated by hydrogel. (**B**) Upgraded version with handles, increased working surface and minimized scaffold area for light-sheet microscopy setup. We also added columns for stability without hydrogel and a combination of pyramids and holes for axonal growth through layers. (**C**) Upgraded scaffolds attached to a holder and locked to avoid floating and minimize movement during handling and media exchanges. (**D**) The 2D polymer platforms with dipole electrodes were produced for stimulation tests.

Finally, for the single–structure strategy, we designed two different prototypes of 3D polymeric scaffold structures, produced from D-CLEAR using 2PP technique. The first design consisted a 2-level pattern of circles 300 $\mu$m in diameter allocated as a honeycomb (Figure 5.5). During 2PP fabrication, each hexagonal layer was shifted in X and Y directions by half of the cylinder diameter in respect to the previous layer, with $x$ and $y$ directions being the principal directions of the hexagonal lattice (forrming an angle of 60 degrees). The circles were 20 $\mu$m thick and were separated also by 20 $\mu$m.

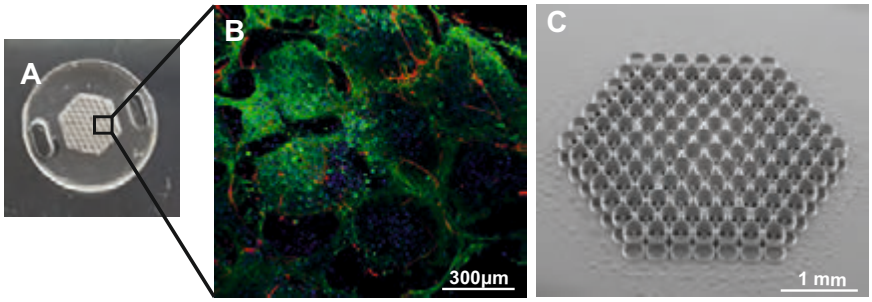


**Fig. 5.5 Single–structure scaffolds designs and printed versions.** (**A**) Live picture of a 'honeycomb' scaffold in the center of a D–CLEAR pellet with handles for stack. (**B**) hiPSC–derived neurons cultured and differentiated on 2PP fabricated D-CLEAR scaffold. The immunostaining was conducted at DIV83, marking the presence of astrocytes (GFAP, red) and neurons ($\beta$–tubulin, green). The total lateral size is 1 mm. (**C**) Detail of the honeycomb structure.

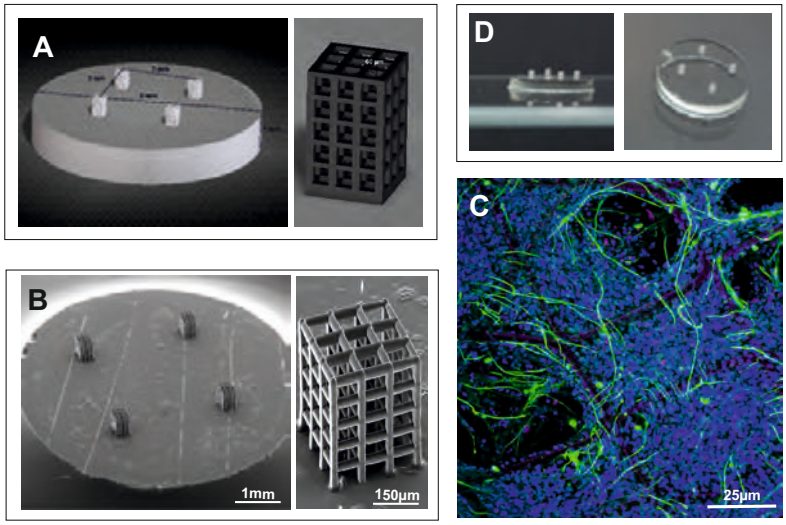


**Fig. 5.6 Single–structure scaffolds designs and printed versions.** (**A**) The design of four equidistant tower scaffolds on top of a D–CLEAR pellet. (**B**) Detail of the 2PP printed towers. (**C**) Projected Z–stack of confocal imaging (20x magnification) of human iPSC-derived neurons (Axol Bioscience line AX–0016) and astrocytes (Axol Bioscience line AX–0001) co–cultured on 2PP-printed D-CLEAR suspended 3D scaffold for 32 days in vitro. Astrocytes were typically positive for GFAP marker (green) and S100B marker (magenta). Both neurons and astrocytes are DAPI positive (blue). (**D**) Live picture of the samples.

The second design was a grid–like structure composed of 5 layers, arranged one above the other with a 100 $\mu$m distance, so that the whole scaffold structure had a size of $300 \times 300 \times 500$ $\mu$m$^3$ (Figure 5.6), resembling a skyscraper skeleton or 'tower'. The samples were so delicate that a subsequent design with less 'floors' was proposed for onward experiments.

## 5.5 Discussion

Despite our efforts, none of the scaffold designs reached the final stage. When possible, neurons preferred to attach to the bottom glass surface rather than embracing the scaffold structure or climbing obstacles to the next level. An additional problem was the conformation of the samples, since their small size made difficult hand manipulation without damaging the culture, and their thinness often resulted in the material experiencing bending or a tendency to float in the medium.

As no instrumentation for the allocation and precise alignment of the scaffolds were provided within the MESOBRAIN consortium, it was virtually impossible to build reproducible structures. Thus, when writing these words, all we could prove is that neurons were compatible with the scaffolds and that different designs could be explored, but sadly no actual 'scaffolded 3D network' could be brought to light.

Subjectively speaking, the MESOBRAIN proposal should eventually succeed as new neuroengineering techniques develop, but it still requires adjustments and new technological tools, such as precise robotics or cell printers, to assemble the different partial successes.

All in all, as shown in the following chapters, simpler 2D scaffolds and 3D networks solely on hydrogel gave uplifting results and allowed us to explore the rich connectivity patterns of different network constructions.

# Chapter 6

# Results III: Dynamics and Effective connectivity in hiPSCs cultures

The limited availability of human brain tissue for research purposes has required the use in many different models to mimic physiological and pathological conditions of the central nervous system (CNS). Animal models have been useful to learn about brain disease mechanisms and potential treatments, but quite often failed during translation into humans, probably due to the considerable differences in complexity between the brain of the human beings and rodents (most used animal model in the laboratory).

The advent of human induced pluripotent stem cells (hiPSCs) has revolutionized the possibilities of in vitro models to study human brain, presenting enormous potential for disease modeling and drug screening (Bellin et al., 2012). During the last 10 years, many studies using this technology have established *in vitro* model systems that more reliably identify molecular pathways and predict effective drug targets for neurological disorders. Exhaustive morphological, biochemical and functional characterization is needed in order to detect phenotypical differences between health and diseased cells. Up to

this point, some limitations of these *in vitro* models have been tied to the lack of tools to study complex systems and extract reliable neuronal functional features.

In this chapter, we evaluate whether hiPSCs-derived neuronal cultures can reach important levels of neuronal activity, with processes that resemble brain development and network establishment. Results show that these cultures behave completely different from rat brain neuronal primary cultures. We also present several characteristics of the networks that are specific of human neurons and can be used to evaluate possible defects in neuronal function derived from neurological diseases.

## 6.1 Human–derived cortical neurons from iPSCs

Since the breakthrough of generating hiPSC (Takahashi et al., 2007), *in vitro* studies jumped into the task of differentiate specific cell types, such as glutamatergic pyramidal neurons and GABAergic interneurons (Shi et al., 2012), also co-cultured with the presence of astrocytes (Kuijlaars et al., 2016). The scientific community has also made a tremendous effort evaluating the electrophysiological properties of these cell lines (Odawara et al., 2014), diminish the risk of genetic mutations or instability (Shi et al., 2017) and examine whether there is persistence of aging cellular markers that represent late–onset conditions (Mertens et al., 2015). While direct conversion of hPSC maintain age–equivalency, differentiated hiPSC are rejuvenated and allow follow–up of neurodevelopmental stages (Mertens et al., 2016).

In this Chapter, we used hiPSC of healthy patients, treated to obtain neuronal precursors (NSC) and differentiated them into juvenile cortical neurons and glia. With that in mind, the first step in a hiPSC study is to optimized culture conditions and characterize the cell subtypes of the population.

### 6.1.1 hiPSC characterization

Human iPSC-derived cultures presented good density and homogeneous distribution with approximately 80% of the cells identified as neurons with the cytoplasmic marker MAP2 (microtubule associated protein 2), and 10% of reactive astrocytes immunopositive for GFAP (Glial fibrillary acidic protein) at DIV55-60 (Figure 6.1). Astrocytes presented bigger size and more complex ramifications as compared to rat primary cultures (Figure 7.1).

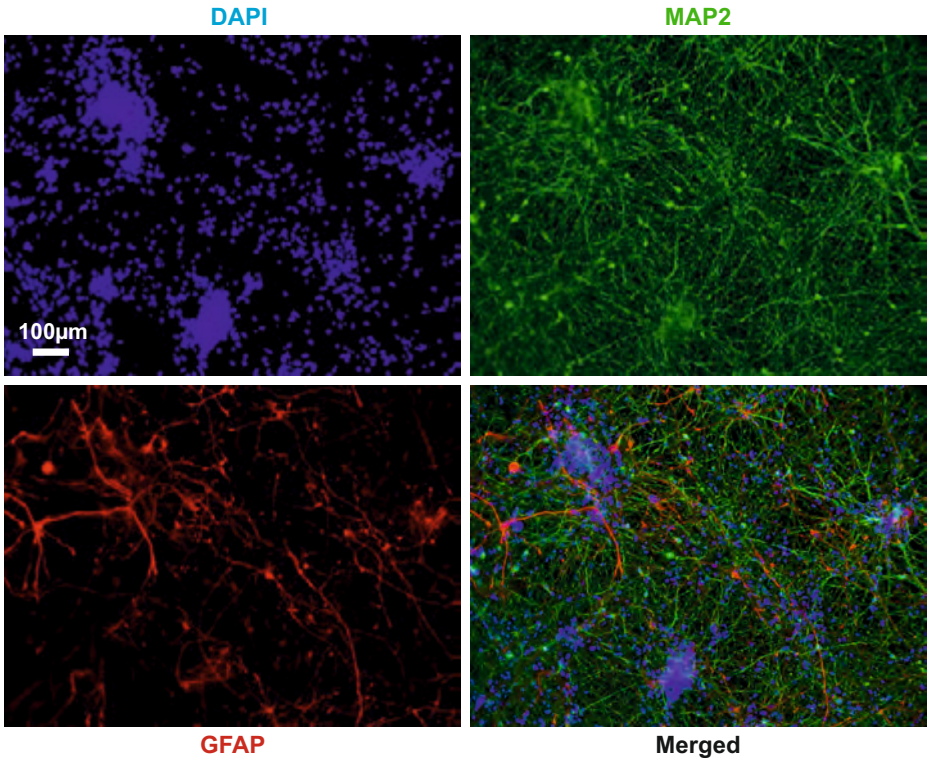


**Fig. 6.1 Expression of neuronal and astrocytic markers.** The four panels correspond to the same representative sample under different channels. The fluorescent photomicrograph shows the expression of MAP2 (in green) and GFAP (in red) in a representative field of hiPSCs-derived neuronal culture at DIV55-60. Cell nuclei were counterstained with DAPI (in blue).

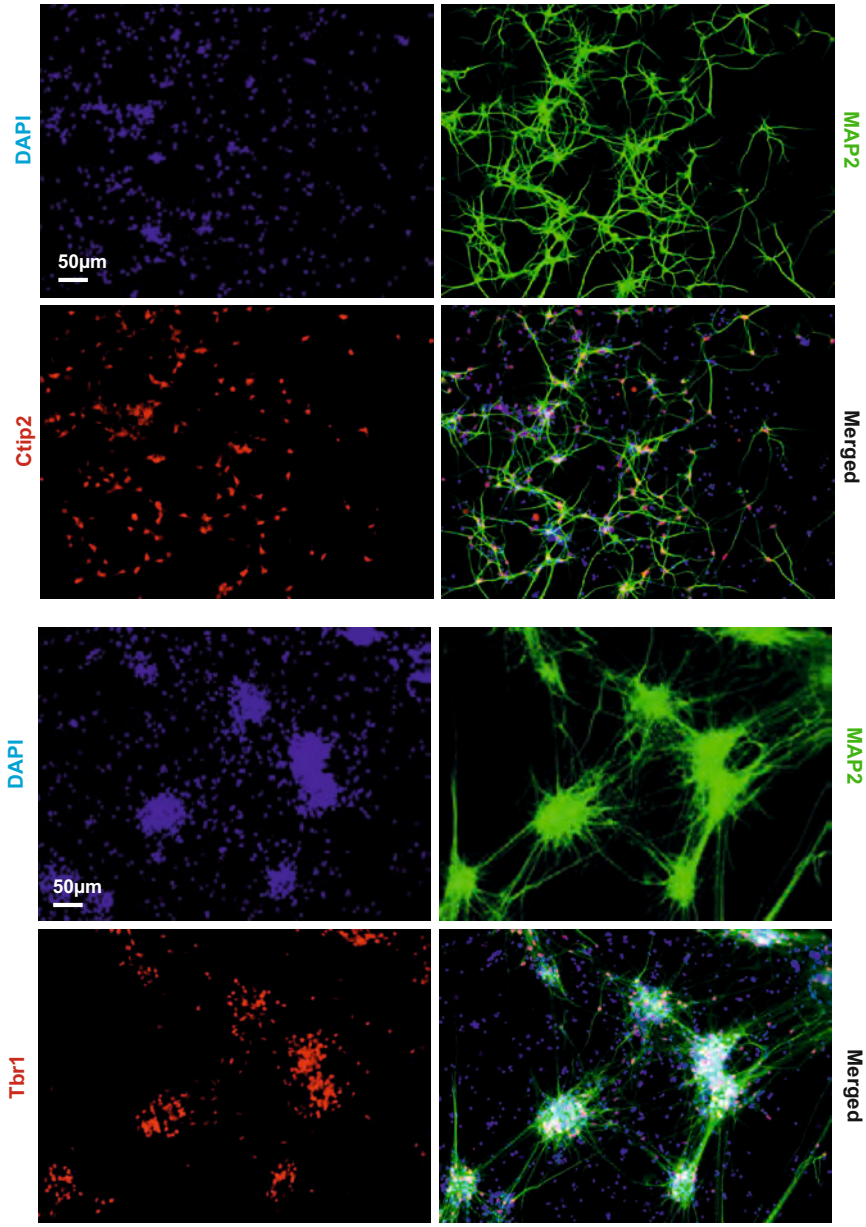


**Fig. 6.2 Expression of specific neuronal cortical markers.** Fluorescent photomicrograph showing the expression of MAP2 (in green) in a representative field of hiPSCs-derived neuronal culture at DIV55-60, where cell nuclei were counterstained with DAPI (in blue) for both collages. (**A**) Ctip2 (in red) (**B**) Tbr1 (in red).

The majority of mature neurons (positive for MAP2) were also immunoreactive for cortical specific markers (Figure 6.2), including Tbr1 (38.5% of the neurons), Ctip2 (26.25% of the neurons) and Satb2 (33.75% of the neurons). After infection with AAV carrying GCaMP6s indicator, around 50% of the neurons expressed the protein at DIV55-60 (Figure 6.3).

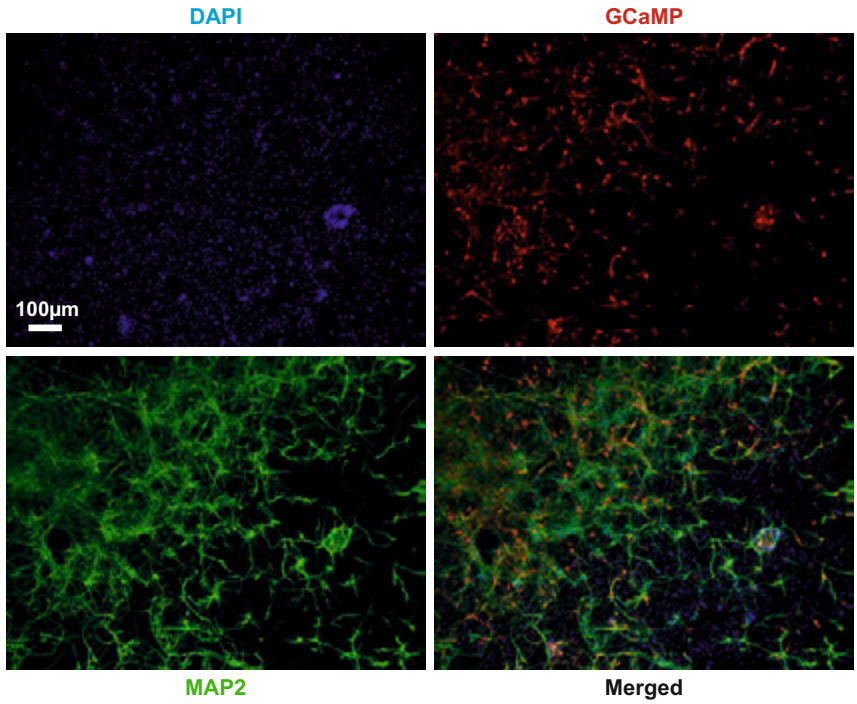


**Fig. 6.3 Efficacy of infection with AAV-GCaMP6s.** Fluorescent photomicrograph showing the expression of GCaMP6s (in red) in the neurons, immunoreactive for MAP2 (in green), generated from hiPSCs and infected with AAV carrying this calcium indicator. Infection was performed at DIV7 and cultures were fixed and stained at DIV55-60. Nuclei were counterstained with DAPI (in blue).

Morphological features of human iPSC-derived cultures were very stable between replicates, and we did not observed particular dissimilarities in cultures with higher levels of aggregation. Indeed, it is worth mentioning that, as the culture ages, aggregation appears more frequently.

## 6.2 Tracking effective connectivity

For these experiments we analyzed 8 cultured samples from NSCs, obtained from two different batches. Cells were maintained in proliferative conditions for 2 weeks to reach nominal density, then we started the differentiation process (DIV0) and followed the neuronal network development until the culture deteriorated ($\sim$DIV60). Neurons were infected with the fluorescence indicator GCaMP6s at DIV7 and started showing spontaneous activity around DIV16. We compared the developmental trend and distinctive timepoints with 8 primary rat neuronal cultures from three different batches (dissections), infected with GCaMP6s at the second day after seeding (DIV2). Spontaneous activity in these primary cultures arose at DIV6 and ceased around DIV21. All samples, either hiPSCs or primary, shared same experimental conditions and were recorded at 33fps during 10 minutes, every 2–3 days. Although there were more than 2,000 neurons in the FoV, to speed up the computational pipeline, we worked with subsets of 200–400 ROIs easily discernible. Every hiPSC sample was cultured in an individual 'grid–glass' bottom petri dish, so every recording was performed within the same area and most likely the same population of neurons.

### 6.2.1 Image registration

Image registration is a computational process that aligns geometrically two images taken at different times (Brown, 1992; Zitova and Flusser, 2003). It is a crucial technique in medical imaging for diagnosis and follow–up care, specially to track anatomical changes throughout the course of therapies. Here, we applied these concepts to align fluorescence images of the same neuronal culture recorded at consecutive DIVs, in order to recognize cell bodies within a population and perform cell–personalized analysis.

The technique of 'image registration' can be carried out by different methods. One of them is the 'Similarity Transform', which estimates the geometric changes between two multimodal images, i.e. with different grayscale intensity distributions, by a recursive matching procedure that maximizes intensity similarity. The result is a transformation matrix $T$ given by

$$\begin{pmatrix} \cos\theta & \sin\theta & t_x \\ -\sin\theta & \cos\theta & t_y \\ 0 & 0 & 1, \end{pmatrix} \tag{6.1}$$

where $\theta$ is the rotating angle and $t_x$, $t_y$ are the translation parameters. As illustrated in Figure 6.4, we applied the transformation to every ROI vector $A$ with initial coordinates $(x,y)$ such that $A' = T \cdot A$, described as

$$\begin{pmatrix} x' \\ y' \\ 1 \end{pmatrix} = \begin{pmatrix} \cos\theta & \sin\theta & t_x \\ -\sin\theta & \cos\theta & t_y \\ 0 & 0 & 1 \end{pmatrix} \begin{pmatrix} x \\ y \\ 1 \end{pmatrix} \tag{6.2}$$

We called the second method 'Consecutive Pairs'. It is based on the same principle but, instead of setting always the first image as the reference for all the following DIVs, the reference image is updated in each iteration to be the one immediately before the one to be transformed. This methodology performs better pairwise predictions but every mistake is carried and worsened through iterations. The outcome is exemplified in Figure 6.4, however, the two results are identical because A and B are the first pair of images.

Finally, the 'Point Mapping' method requires manual intervention using the control point selection tool of Matlab, a user interface that allows to assign equivalent pairs of points in two images and return the pixel coordinates. With this methodology we can accurately align the grids, but as shown in Figure 6.4 the matching is less optimal.

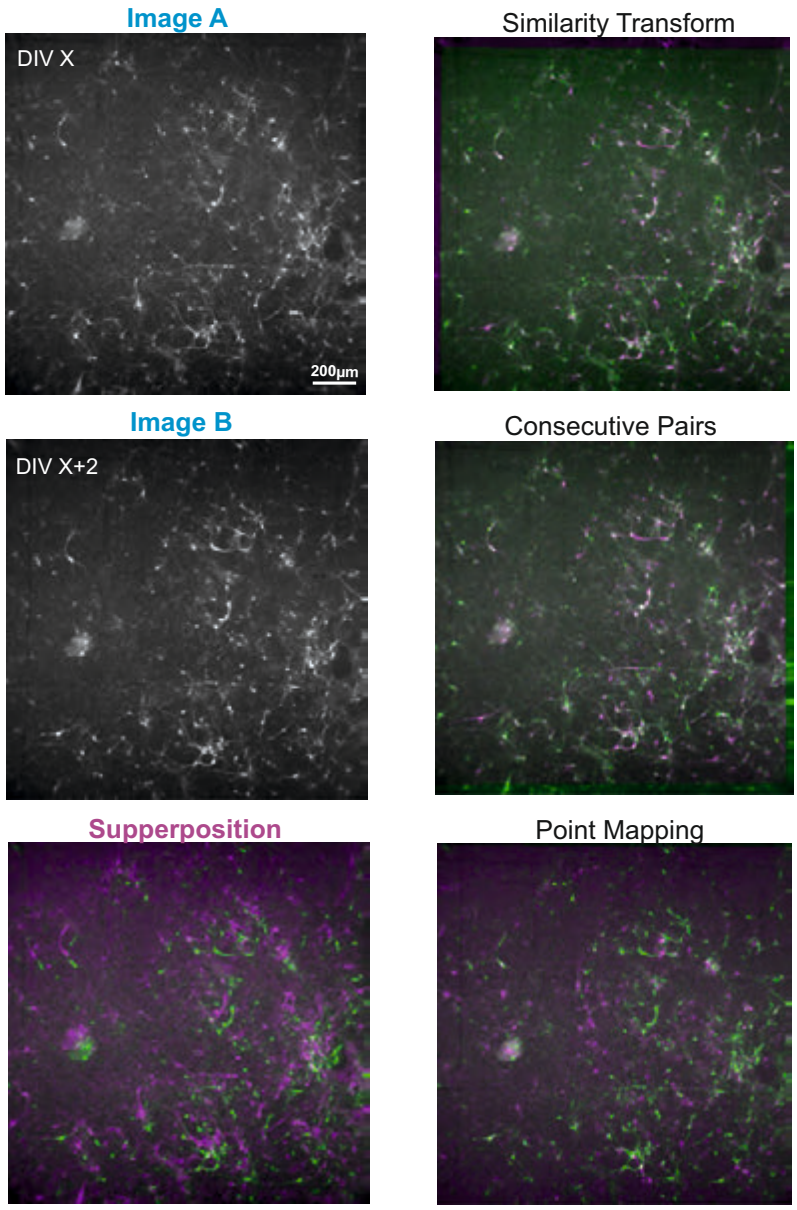


**Fig. 6.4 Image Registration strategies**. The left column shows two consecutive images (A and B) of the same culture, obtained with a difference of 2 days *in vitro*. The bottom image displays A and B superposed in green and purple, and when there is a match the colors are merged as white. The right column shows the result of the three different strategies applied.

In general, and despite the reasonable performance of the different methods, working with neuronal cultures entrails a challenging problem: the substrate from one day to the other in seemingly random directions. Cell matching then becomes a problem similar to *Where's Wally?* game.

Advanced combination of registration techniques and object recognition is needed to address this problem (Cheraghi and Sheikh, 2012). First the placement mismatch between images is estimated and compensated as described before to stabilize the background, then detection algorithms are applied to follow the moved objects in the foreground, i.e. the neurons migrating. This future work will allow longitudinal analysis not based on different population statistics but on same individual cells, extremely enhancing the quality of the data (Harris et al., 2016; Sheintuch et al., 2017).

### 6.2.2 Neuronal activity in hiPSCs

Tracking the effective connectivity on a network population, where neurons are delimited within the same grid area, allowed the study of the individual neuronal maturation process in hiPSCs-derived cultures. Analysis of neuronal activity showed that spike trains start uncorrelated and evolve into synchronized, refined coactivations. From here onwards we will use the term 'synchrony' to refer to these simultaneous coativations of several neurons within a time window, that correspond to *network burst* from a neuroscience perspective. Although these synchronous events may actually correspond to super fast propagating waves or spatiotemporal patterns, we did not have sufficient time resolution to resolve such inner structure.

As an example of how activity evolved along maturation, we manually tracked 10 representative neurons randomly distributed from DIV16 to DIV55 to illustrate the potential of this methodology (Figure 6.5). We emphasize that, in following sections, ROIs do not necessarily match the same cells among the different timepoints and the number of neurons considered may vary among recordings.

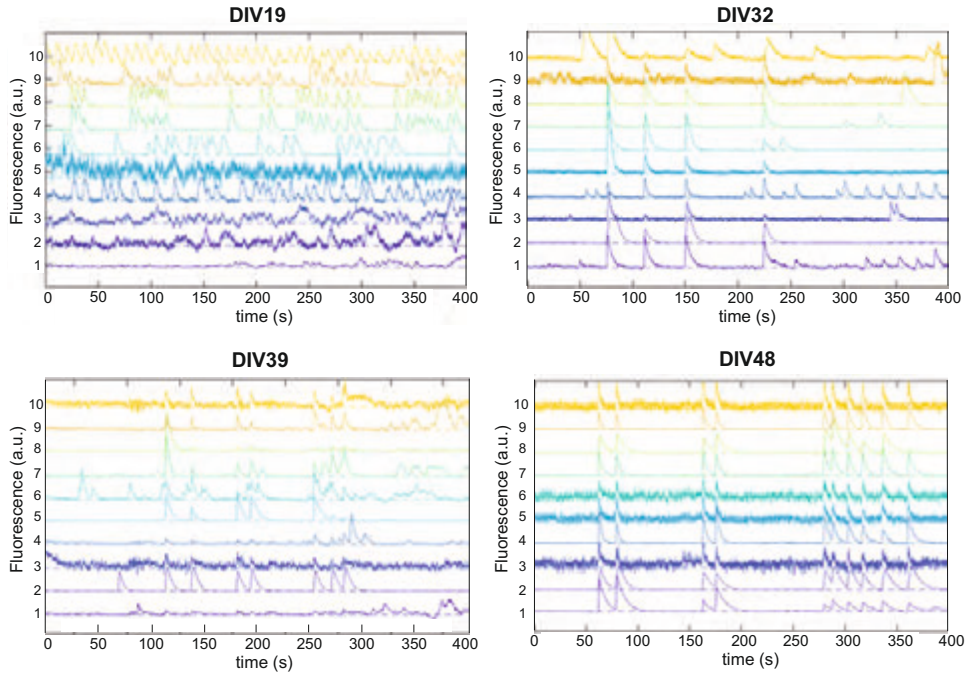


**Fig. 6.5 Tracking activity of specific cells.** The same 10 neurons from a hiPSCs–derived neuronal culture were manually recognized in 14 different recordings spaced along 40 days. Four representative timepoints (depicted at the top of each graph) are shown, each containing the 10 fluorescence traces. The panels illustrate the dynamic evolution of the neurons along maturation. Traces were individually normalized as $\Delta\text{FF} \equiv (F - F_0)/F_0$, where $F$ is the raw fluorescence (gray-scale level) on the images) and $F_0$ is the corresponding baseline. Normalized data is represented as fluorescence arbitrary units (a.u).

Cultures from hiPSC–derived neurons started to show activity around DIV16. The fluorescence traces of a representative sample exemplifies how at early stages as DIV19, 6 out of 10 neurons showed neat activations (Figure 6.5). The fluorescence variations in the apparently silent neurons could be distinguished from noise. At this timepoint, the spikes of the different cells were uncorrelated. As the culture matured, neurons started to display some simultaneous coactivations (DIV32-39) while by DIV48 almost all activations were fully synchronous.

### 6.2.3 Effective connectivity and network evolution

Onset of neuronal activations was determined from extracted traces of hiPSC-derived cultures using the Schmitt Trigger method (Section 3.1.2) and displayed as temporal raster plots. Effective connectivity was then calculated through GTE (Section 3.2.2), using a binning of 100 ms, a z–score (confidence interval) of 1, and final data inspected to detect functional modules. The utilized z–score retains those connections that derive from synchronous events, and therefore allows to detected whether the culture contains well–defined functional modules or it is essentially a synchronous system with poor internal structure.

Representative effective connectivity matrices comparing the results of hiPSC and primary rat cultures are shown in Figure 6.6. For sake of clarity, we must note that rat primary and hiPSC–derived cultures evolved with different time–scales. Taking into account he onset of spontaneous activity and the lifespan of the both systems, we defined for each culture corresponding timepoints at 10%, 40% and 75% of their lifespan. Since hiPSC–derived cultures were monitored during 40 consecutive days and rat primary cultures for 21 days, we selected DIV21, DIV32 and DIV46 as key timepoints for hiPSC–derived cultures, and DIV8, DIV14 and DIV17 for rat primary cultures.

Looking to hiPSCs in detail, the absence of network bursts at early stages (DIV21) rendered effective networks with neat functional modules (Figure 6.6A, left). These modules grew in size as development progressed and exhibited more inter–modular links, signaling the onset of a dominant synchronous behavior (Figure 6.6A, right). In primary rat neuronal cultures, modules at DIV8 were relatively bigger and certainly more linked ((Figure 6.6B left), indicating that these cultures emerged highly synchronized. This behavior was maintained at later stages, indicating that synchronization was strongly retained (Figure 6.6B, right). Spatial plots of the effective networks are plotted in Figure 6.7A. They show that connections are abundant

and that the network cohesion is strong, with several effective connections crossing the entire system.

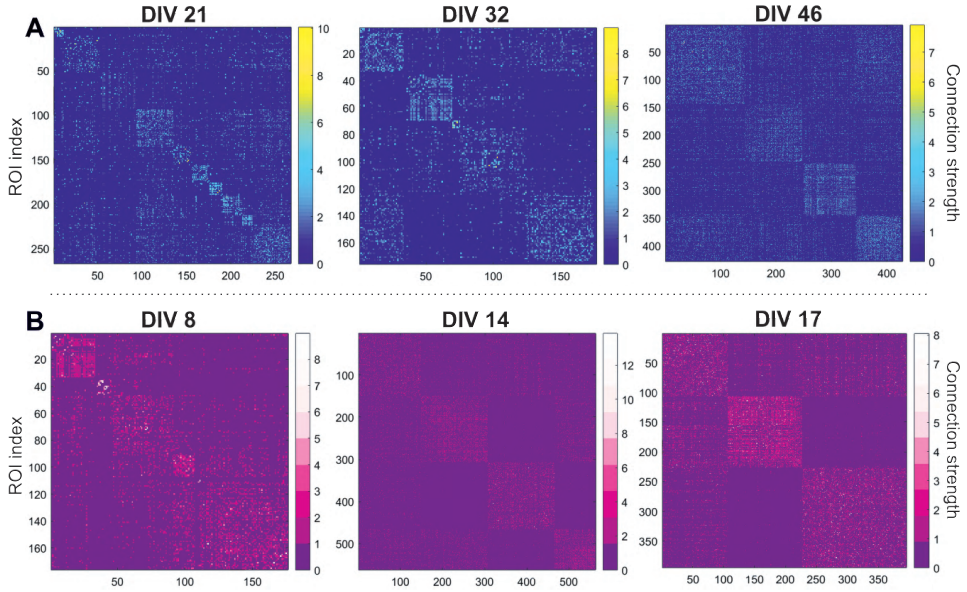


**Fig. 6.6 Effective connectivity matrices in hiPSC.** (**A**) Effective connectivity matrices of a representative hiPSC sample at gradually higher timepoints. The connectivity strength among pairs of nodes is ordered by modules. (**B**) Equivalent representation for a representative primary rat neuronal culture.

To further study network evolution, we took a step backward and analyzed neuronal activations as displayed in temporal raster plots (Figure 6.7B). As seen before for few traces, the data of the rasters neatly depict a gradual increase of activity and synchronization degree. Indeed, activity evolved from scattered firings (DIV21) to a strong network bursting (DIV48) passing through a period of mixed individual and collective events (DIV32). An alternative representation of such an evolution is shown in Figure 6.7C, which portrays the cross–correlation values of the fluorescence traces. At young stages only a small group of neurons correlated (bright yellow area). As the culture matured, more and more neurons coordinated, until finally the entire culture lighted up at unison.

We repeated these analyses for rat primary cultures to quantify the differences between these two *in vitro* models. In contrast to hiPSC-derived neurons, rat primary neuronal cultures showed high levels of synchronization coinciding with the appearance of spontaneous activity by DIV6–8, with highly connected maps (Figure 6.8A) and very few events outside network bursts (Figure 6.8B left). No significant changes occurred upon aging (Figure 6.8B, middle and right). Cultures started to degrade by the end of the third week (DIV18–19), leading to a decay of bursting rates and gradually lower active neurons that signaled the end of the culture tracking. The analysis of similarity among traces did not provide any further information, and just reflected high levels of synchrony from the beginning to the end.

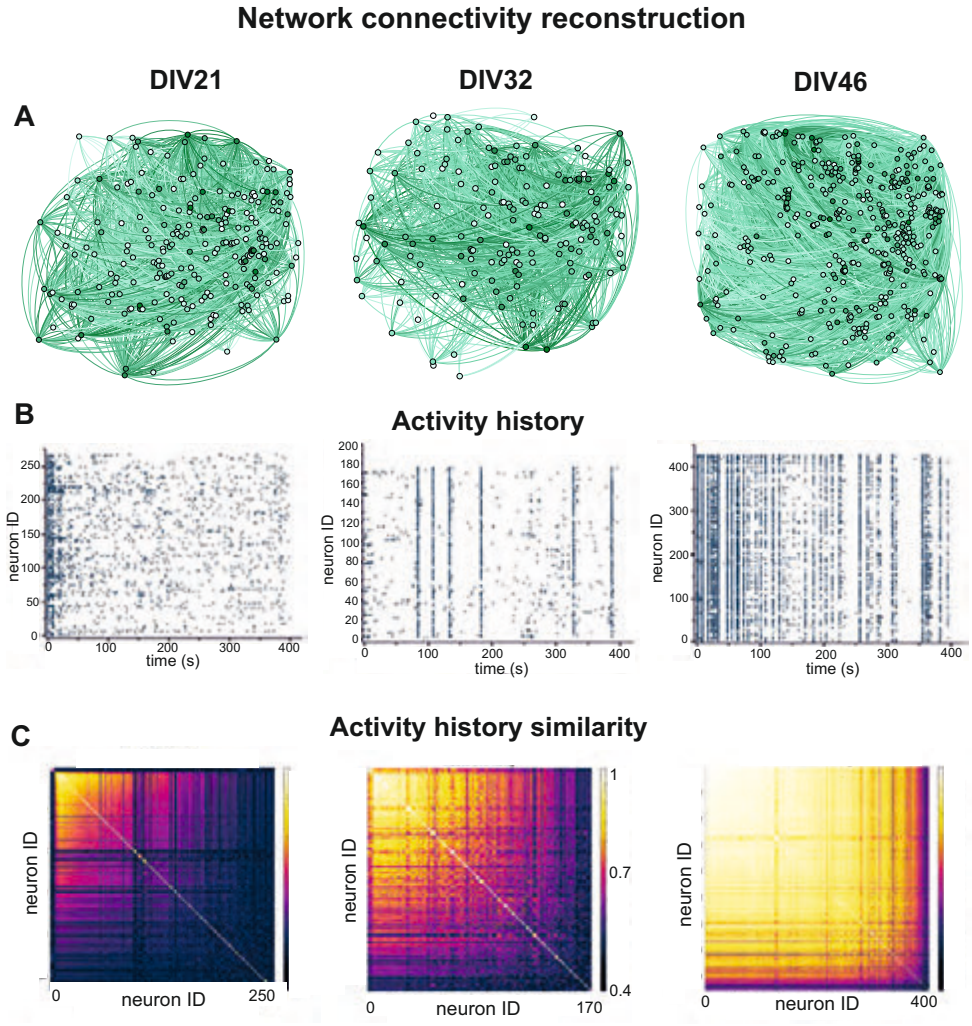


**Fig. 6.7 Network connectivity evolution of hiPSC cultures** (**A**) Spatial representation of the effective connections, obtained from GTE analysis at the different timepoints. The darker the color of the node (neurons) the higher its degree. The width of the connections is also proportional to its weight. (**B**) Activity history displayed as temporal raster plots of spikes detected for every neuron (y–axis) within the time of the recording (x–axis). (**C**) Similarity analysis of neuronal activity, obtained from the cross–correlation computation among neuronal fluorescence traces.

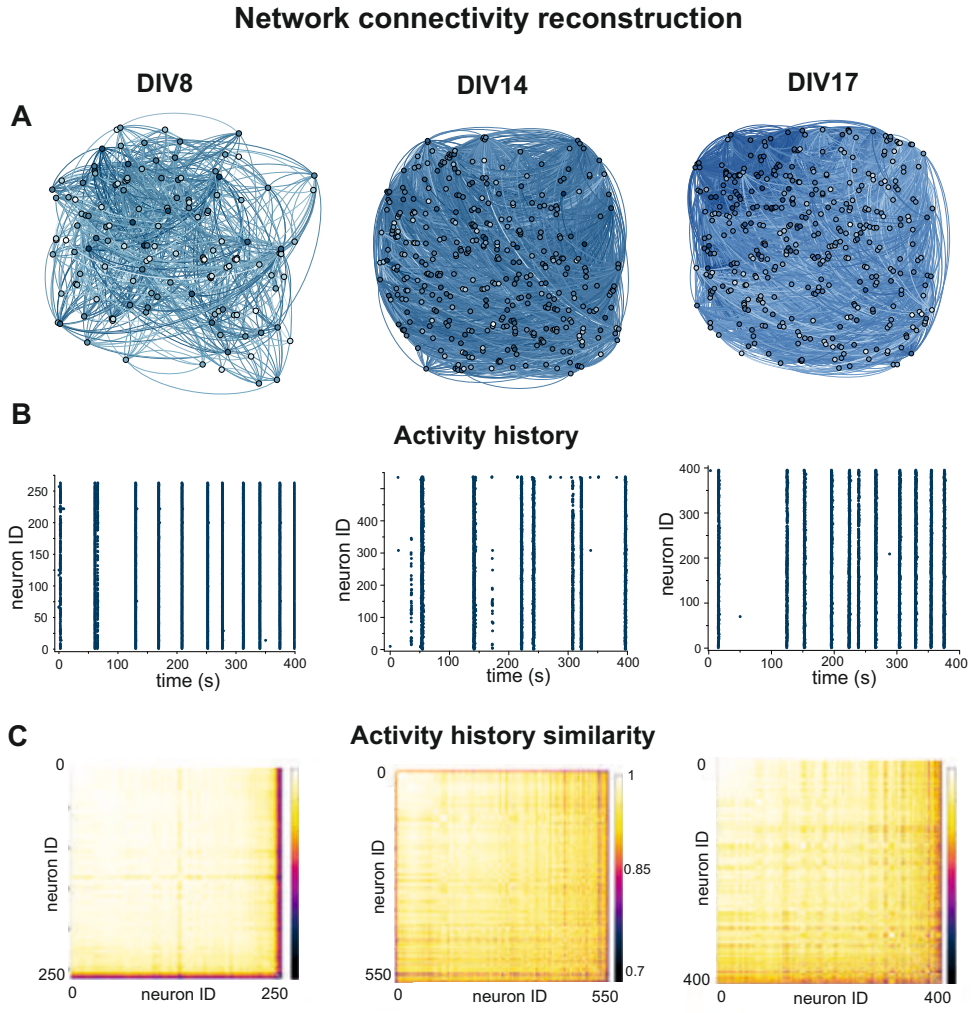


**Fig. 6.8 Network connectivity evolution of primary rat cultures** (**A**) Spatial map of effective connections obtained from GTE analysis at different timepoints. The darker the color of the node (neurons) the higher its degree. The width of the connections is proportional to its weight. (**B**) Activity history displayed as temporal raster plots of spikes trains. (**C**) Similarity analysis of neuronal activity, obtained from the cross–correlation computation among neuronal fluorescence traces.

## 6.3 Behind the scenes: Network development

Based either on the activity history (raster plot) or the inferred effective connectivity (Section 3.3), we computed several features to characterize the dynamics and maturation of the networks originated from hiPSCs, and compared them with primary rat cultures. First, we evaluated the network synchrony and the complexity of dynamical patterns, then we computed the global efficiency of the network and the Louvain modularity Q to better quantify the structure of functional modules.

### 6.3.1 The turning point in synchrony

We considered interesting to quantify the degree of synchrony in the cultures. For hiPSCs cultures, the maximum participation of active neurons in a burst reached approximately 90% only at late stages of maturation, being the global average during the maturation process about 60%. This means that even at late stages of maturation there is still noticeable modularity, while in primary rat cultures the participation often includes 100% of the active population since very early stages of development (Figure 6.9).

We also observed that, in hiPSC cultures, synchrony suddenly started to dominate from DIV40 onwards. This is clear by analyzing the Synchrony Index (Figure 6.10A). By DIV50-55, around 15% of the events were synchronous bursts with at least 40% participation of active neurons. The reason for this low level of participation is grounded on the fact that the frequency of synchronous events gradually decreased along maturation, but that those that occurred actually had a much higher presence of neurons. Interestingly, in the range DIV45–55, we observed a boost in the variability among cultures (shaded area in Figure 6.10A). This result is an important warning to researchers investigating hiPSC as it stresses that results cannot be interpreted carelessly, because the variability between samples at different DIVs may mask entirely a property under study.

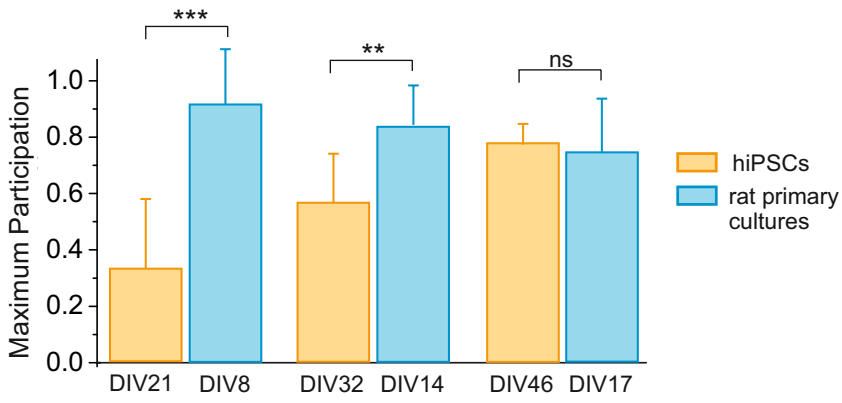


**Fig. 6.9 Maximum neuronal participation in synchronous events** Comparison between hiPSC (orange bars) and primary rat cultures (blue bars) participation in firing events, at corresponding indicated timepoints (x–axis). Bars show mean values ± STD. $n = 8$ samples for both types of cultures were used for statistics.

### 6.3.2 Effective connectivity network details

Since synchronization clearly dominates the culture dynamics, we carried out the analysis of modules excluding synchronous events, allowing for a characterization of the inner structure of the network along maturation. To carry such analysis, we considered a large z–score of $z = 2$ in the GTE significance threshold, which effectually eliminated weak effective links associated to synchronous events.

With this selection in mind, we tracked the evolution of the modularity Q (Section 3.3.5) and observed that it constantly increased with two particularly high slopes at DIV22 and DIV40 (Figure 6.11 A). The latest slope coincides with the change into synchronous dynamics. We ascribe these increases to network crosstalk outside bursts, which becomes more sparse and isolated, and with individual freelance neurons possibly being assigned as single modules. The maximum peak is $Q = 0.5$, which concurs with the data obtained from primary rat cells, which show since the beginning a high value of $Q = 0.48 \pm 0.09$.

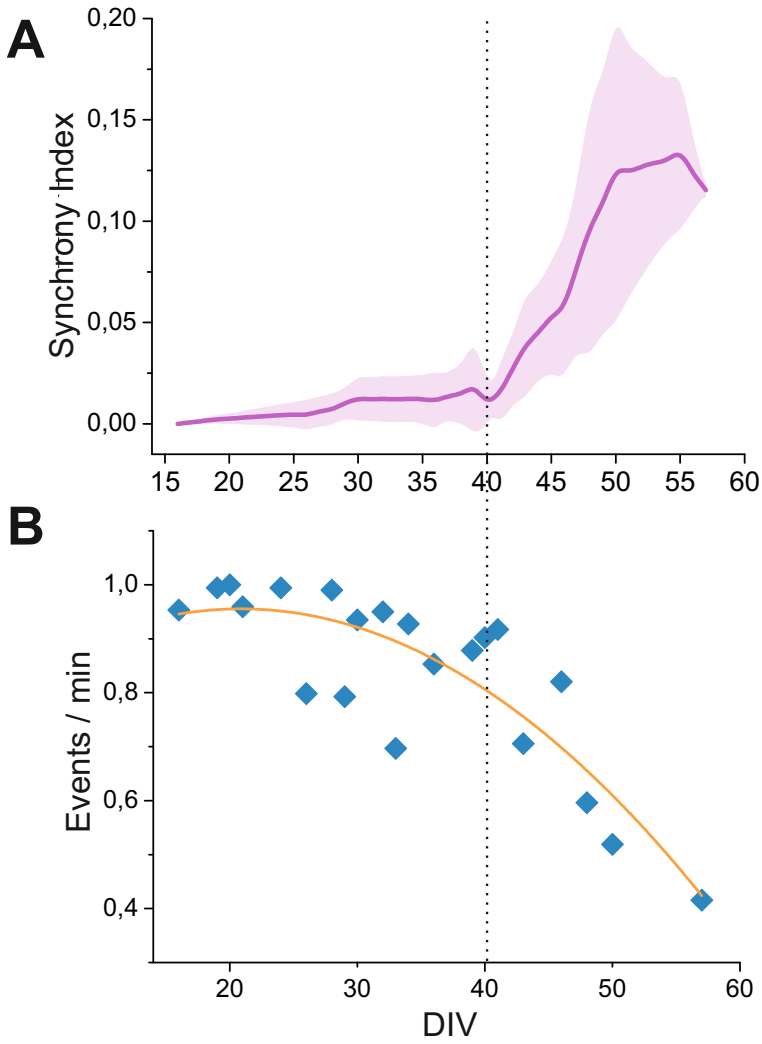


**Fig. 6.10 Synchrony evolution during development** (**A**) The synchrony index represents the ratio between events with more than 40% of their maximum participation score (big bursts) and firing events with less than 40% participation along maturation. (**B**) The rate of events shows the number of non–overlapping time windows when neuronal activity appeared. It is represented as the mean of events per minute and normalized by the total count of active neurons for $n = 8$ samples. The curve is a guide to the eye.

We determine that full network activations (100% participation) in the form of network bursts cannot provide additional information, since they would correspond to a persistent on–off state close to a random network. In that case we could only compute the average pathway of information by analyzing the propagation of activity in detail from its imitation point towards the rest of the network, an analysis that was beyond the scope of this Thesis.

The evolution of the global efficiency was also tracked. Here, iPSCs showed a gradual decay consistent with the increment of Q. In other words, the increased number of tiny or singleton communities outside bursting events implied a lower capacity to efficiently propagation information through this outer network, thus the global efficiency fell, reaching $G_{\mathrm{EFF}} \sim 0.3$ by the end of its lifespan. Again, this result concurs with the primary rat data, where the efficiency remained stable as $G_{\mathrm{EFF}} = 0.30 \pm 0.08$.

We note that fluctuations are expected since the number of neurons detected varies and these two properties are sensitive to the size of the network. Moreover, to fully understand these changes along development it would be necessary to also track changes in structural connectivity that may appear during that time and evaluate how they affect the effective connectivity.

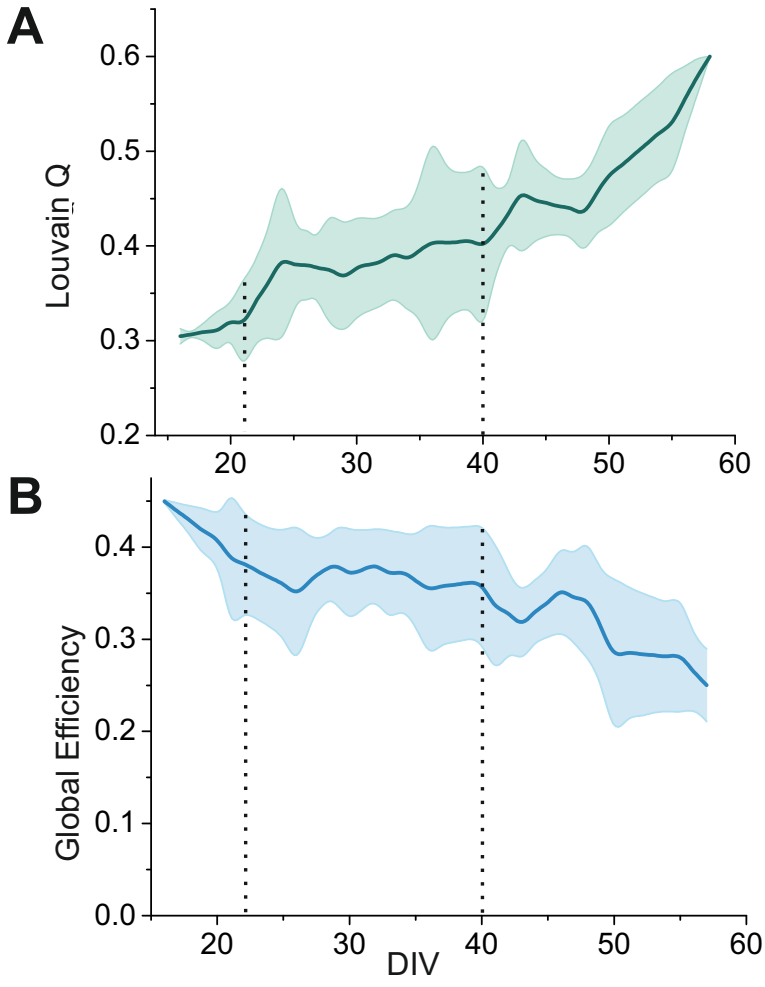


**Fig. 6.11 Network properties evolution in hiPSC cultures** (**A**) The mean Louvain modularity Q was averaged among 8 experiments and the standard deviation is shown in shaded color. Two particular ramps at DIV22 and DIV40 are depicted with dotted vertical lines. (**B**) The mean Global efficiency was also averaged among 8 experiments and the standard deviation is shown in shaded color. Vertical lines correlate with the ramps depicted in A.

## 6.4 Discussion

Cortical neurons from human–derived induced pluripotent stem cells (hiPSC) settle high–order networks and undergo a maturation process with clear turning points and defined activity patterns for different stages. At week 5 after starting final differentiation, synchrony firing was predominant in the network and reached an extended population during the following weeks. This synchronous behavior has been observed in neuronal networks at different scales and species, but was not pinpointed in the developmental timespan of the same neuronal population. The capture of neuronal activity at high temporal resolution (33 Hz), allowed us to infer the effective connectivity, characterize network properties and provide reliable descriptors of neuronal network maturation.

The understanding of healthy human neuronal development is crucial to assess neuronal pathologies, either derived from trauma, deterioration or maturation deficits. In a lineage-specific context, hiPSC are particularly relevant to study neuronal disorders with complex backgrounds that are difficult to mimic genetically through animal models. Currently, several studies have presented interesting results in modeling Parkinson Disease (PD) (di Domenico et al., 2019) and Alzheimer Disease (AD) (Liao et al., 2016), among others. Localizing effective abnormalities in comparison to healthy networks will help us comprehend the pathways of neurodegenerative processes and eventually find specific treatments.

In addition to their utility for *in vitro* research, the promising therapeutic applications of hiPSCs are mainly founded on autologous transplantation (i.e. transplantation of cells from the same patient). Some studies have already explored their capability to reestablish axonal pathways in the injured adult cortex (Espuny-Camacho et al., 2018), maintain physiological activity (Yin et al., 2019) and reported improvements in neurological disorders in rodents once grafted iPSCs were functionally integrated (Tatarishvili et al., 2014; Wernig et al., 2008). But it is crucial that the transplanted cells are area–

specific and displaying healthy functional dynamics when applying them into clinical trials (Tornero et al., 2013, 2017).

Previous clinical transplants of dopamine neuroblasts showed benefits in PD patients, reaching full impact after 3–5 years (Björklund and Lindvall, 2017). The first clinical trial in humans using hPSC was performed in 2014 to correct a degenerative eye condition (Mandai et al., 2017), but the finding of some small genetic changes put them on hold. Now new projects are taking the leap to resume trials in a limited spectrum of diseases (Trounson and DeWitt, 2016). Although large–scale availability of hiPSC treatments is still far away, advances in the validation of specific neurons derived from hiPSC, physiologically healthy and mature, is an exciting and fundamental step to ensure future safety transplants.

Finally, it is worth to recall that the cerebral cortex of primates (humans) and rodents (rats) share basic physiological properties but also have some fundamental dissimilarities that difficult the translation of results across species. We showed a comparison in maturation paces and activity dynamics during development, that also highlight the importance of using hiPSC to unlock new approaches towards drug screening and overcome current barriers in the study of neuronal networks for therapeutic treatments..

# Chapter 7

# Results IV: Activity in 3D Neuronal Cultures

Three–dimensional neuronal cultures resemble more accurately the *in vivo* cytoarchitecture while maintaining the advantages of *in vitro* models: highly controlled environment, reproducibility and real–time imaging at single–cell resolution. Here, we take advantage of soft semi–synthetic hydrogels to provide a stable, biocompatible and biodegradable structure for neurons to grow in three dimensions. Our objective is to visualize and analyze neuronal activity using calcium imaging techniques and decipher their effective interactions as a complex 3D network.

In this Chapter, we first describe the principal aspects of culturing neurons in an ECM–like environment, then describe the characteristics of our 3D neuronal cultures, and finally present the main results of the conducted experiments. We applied two completely different yet complementary imaging setups: (i) a wide–field fluorescence microscope with high temporal resolution but single–plane focusing, and (ii) a light–sheet microscope with lower temporal resolution but able to scan the 3D volume sequentially.

## 7.1 The role of an extracellular environment

General efforts to comprehend the complex functioning of neuronal networks are based mostly on two–dimensional studies, but the natural environment of neurons is a complex 3D extracellular matrix (ECM) where they can project connections in all directions. How ECM influences the organization and functionality of cells is a matter of intense investigation and has motivated the search of optimal bio–mimetic constructions.

Neurons cultured *in vitro* on glass or plastic surfaces display flattered shapes, sometimes leading to abnormal physiological phenotypes (Caliari and Burdick, 2016), unnatural cell function and dedifferentiation (Baker and Chen, 2012). Additionally, the adhesive proteins keeping them attached to the surface highly restrict migration of the somas and limit neurite extension (Previtera et al., 2010). Conversely, 3D neuronal cultures enhance cell growth and differentiation, improve cell–to–cell and cell–to–matrix interactions, and ultimately neurons exhibit richer functional dynamics and an extensive repertoire of activity patterns (Frega et al., 2014).

As briefly reviewed in Chapter 2.3.1, in recent years hydrogels have emerged as very popular materials for tissue engineering and regeneration, with special interest in their applications for vascular tissue (Arulmoli et al., 2016; Koroleva et al., 2016), muscle (Dikovsky et al., 2006), bone (Lutolf et al., 2003), and neuronal milieu (Aregueta Robles, 2018). Hydrogel designs allow neurons to migrate freely and be homogeneously distributed in a bio–mimetic tissue.

Among the variety of materials available we chose a semi–synthetic hydrogel named PEGylated Fibrinogen (Dikovsky et al., 2006) and adapted it to cortical neurons following previous studies in vascular tissue (Koroleva et al., 2016). The fundamental advantage of hybrid hydrogels is the combination of a biocompatible and biodegradable material with the customization possibilities offered by synthetic polymer chains, such as control over stiffness, mesh size and permeability (Caliari and Burdick, 2016; Drury and Mooney, 2003).

Contrary to other ECM materials like collagen or laminin, fibrin gels are assembled very fast (Janmey et al., 2008), in accordance to their usual role in homeostasis and tissue repair, forming a soft elastic mesh of fibers even at low volumes. Moreover, by regulating all the components in the fibrin polymerization process, one can fine–tune the hydrogel structural properties. Besides, it can be difficult to find an ECM–like material that makes compatible cell growth and cell imaging. Precisely, PEGylated Fibrinogen is transparent and does not cause noticeable optical aberrations. All these reasons positioned PEGylated Fibrinogen as our best candidate for culturing neurons in a 3D environment.

## 7.2 Characterization of 3D primary cultures

3D primary cultures were prepared at Soriano's Lab from dissociated rat cortical cells infected with GCAMP6s and mixed in PEGylated Fibrinogen (see Chapter 2.3 for details). First, we characterized cell types in 2D cultures through immunostaining (Figure 7.1) and we determined that our 2D primary cultures presented, at DIV 12, 70% of mature neurons identified with the neuronal marker MAP2/$\beta$3tub and 30% of astrocytes, marked with GFAP. We quantified a high percentage of neurons from deep cortical layers, being 17% Ctip2 and 63% Tbr1 immunoreactive, probably due to the early developmental stage of the cells.

The adequate density in 3D cultures to enable comparable networks was explored in the literature and based on our experience with 2D cultures. Figure 7.2 depicts two preparations: sample A had the same seeding quantity of neurons as in our 2D cultures, while sample B had twice that density per ml. The latest exhibited better survival rates and procured networks that covered the space more uniformly, possibly also enhancing network connectivity in every direction. Cell counting in 3D cultures revealed 80% of neurons and 20% of astrocytes.

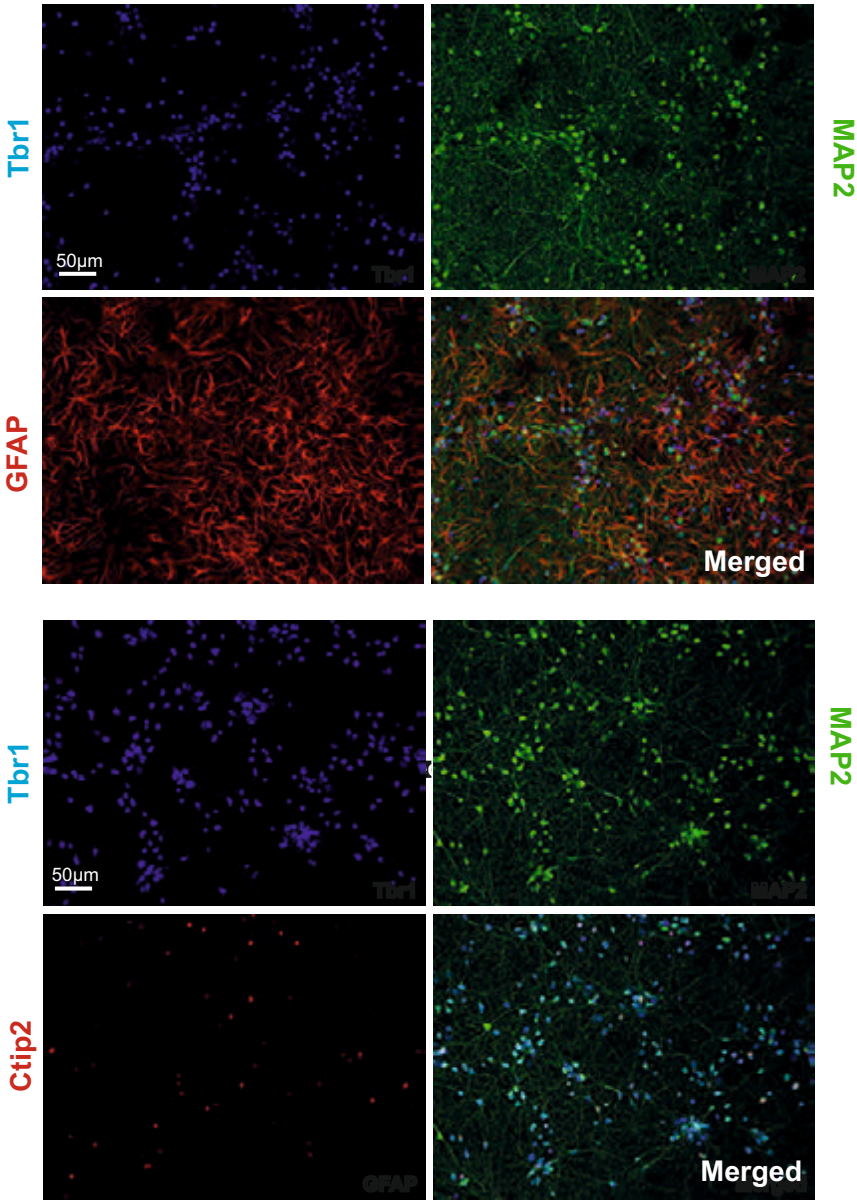


**Fig. 7.1 Expression of neuronal and astrocytic markers in 2D cultures.** The four panels correspond to the same representative sample under different channels. The fluorescent photomicrograph shows the expression of MAP2 (in green) and GFAP (in red) in a representative field of a primary neuronal culture at DIV12. Cell nuclei were counterstained with DAPI (in blue).

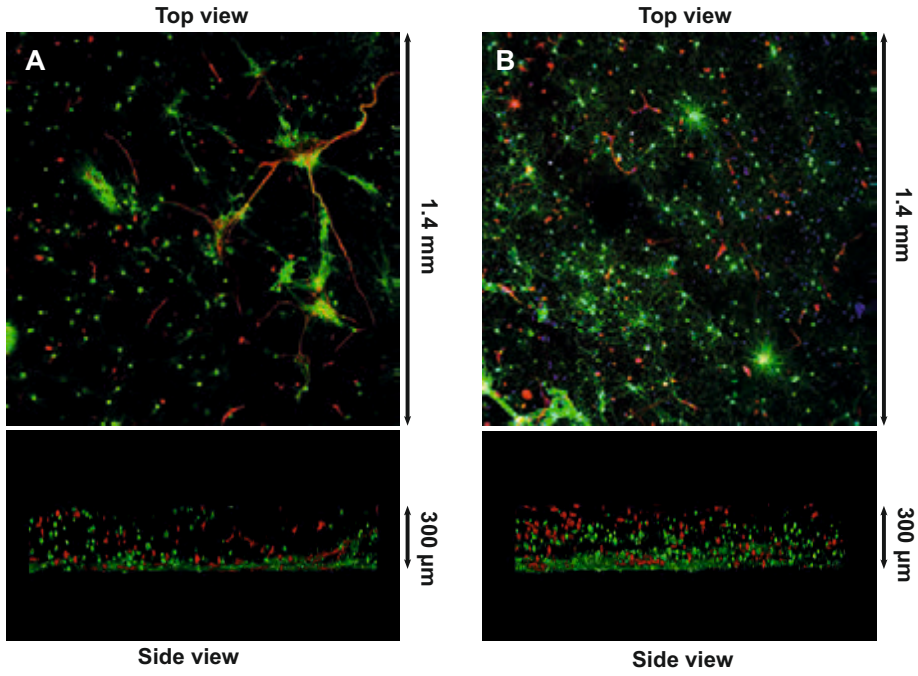


**Fig. 7.2 Expression of neuronal and astrocytic markers in 3D cultures.** The fluorescent photomicrograph shows the expression of MAP2 (in green) and GFAP (in red) at DIV12 in hydrogels with a lateral length of 1.4mm and width 300 $\mu m$. Two different cell densities are shown, being $B = 2xA$ for $A \approx 100,000$ cells/ml when seeding.

## 7.3 3D dynamics with wide–field microscopy

Using the inverted microscope in Soriano's Lab, we investigated the dynamics in prepared 3D hydrogel cultures. As sketch in Figure 7.3, the microscope could only focus in a single plane during imaging, and thus the actual vertical depth of the culture was compromised by the out of focus neurons. Despite the difficulty in capturing with precision all neurons in the volume, this setup and analysis pipeline provided interesting results, as we present later.

The reason for using such a relatively outdated setup for 3D imaging was to test 3D networks feasibility and gather preliminary data that would provide insights for the MESOBRAIN project course.

When focused on a single layer, the density of cells in the field of view (FoV $= 4.5 \times 4.5$ mm$^2$) was comparable to 2D experiments. This large field of view was obtained by combining a 5X objective with a 0.32X optical zoom. The infection efficacy of GCaMP6s was around 40%, a bit lower than 2D because the infection had to be performed during the plating procedure the same day of the dissection, and could not be increased afterwards without a perfusion system. The use of a high–sensitive GECI as GCaMP6s in combination with a high performance camera (ORCA–Flash 4.0) allowed us to record neuronal activity at 50 fps with maximum image size ($1024 \times 1024$ pixels). In combination with the large field of view, our system offered sufficient resolution (4.4 $\mu$m/pixel and a cell size of about 15 $\mu$m diameter) to track single cell bodies. Neurons stayed healthy and active during $3-4$ weeks, with peaks of activity after the second week. Astrocytes were also present, as shown before in Figure 7.2, an indicative of a good culture's viability.

### 7.3.1 Extracting traces from several layers at once

When working with 3D cultures with an inverted microscope, we could only perform recordings at one focused plane at a time. However, the out–of–focus neurons residing in different layers could be analyzed simultaneously with sufficiently good singal–to–noise ratio (SNR). The trick was to pinpoint the exact $x-y$ position of the neuronal somas in close layers and include those as Regions of Interest in the analysis pipeline, being $z$ the corresponding plane. The pipeline is exemplified in Figure 7.3. We typically worked with 3 layers and, when possible, 4.

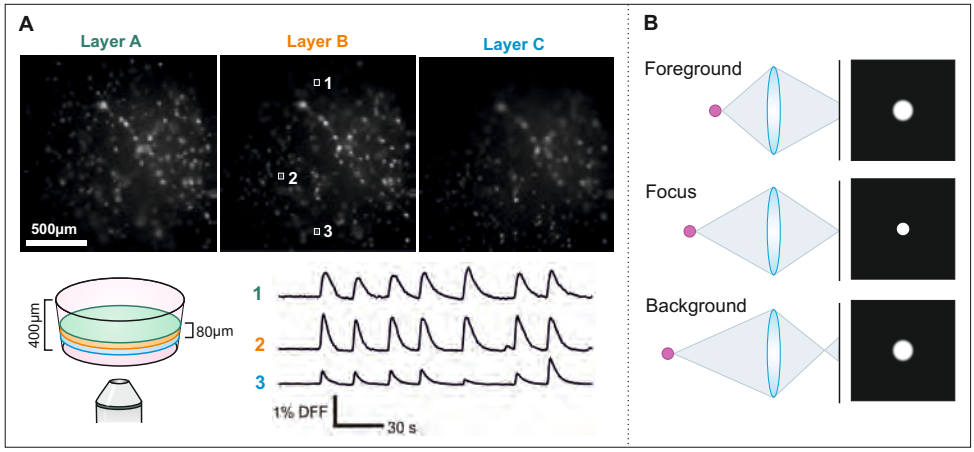


**Fig. 7.3 Imaging and data analysis on different focusing planes.** (**A**) *Upper row.* Three different layers (focusing planes) of a representative culture within a hydrogel, to select the exact $x-y$ coordinates of the somas as ROIs. *Lower row.* The images are taken with an inverted microscope with an approximate accessible depth of 80 $\mu$m. If the layers are close enough, the recorded signals have good signal to noise ratio even when the neurons are out–of–focus. (**B**) An illustration of the blur effect of neurons in the background and foreground.

We note that this 3D analysis method only worked when the blur of out–of–focus neurons did not mask the neuronal activations of neighboring cells. This *bokeh* effect was more prominent when the highlights in the background and foreground were farther away. To avoid blurring, it would have been necessary to increase the depth of field of the image, by reducing the lens aperture, but it would have resulted in higher exposure times and loss of time resolution. Clearly, the best alternative to solve all this problems was to develop an imaging technique for sequential scanning of the layers. This was the task of the improved light–sheet system, as described later.

### 7.3.2 Results: Building 3D data as vertically stacked layers

The previous pipeline was applied to a set of 4 hydrogels obtained from three different batches (dissections), that were recorded approximately once a week

during $3-4$ weeks. Since we used GCAMP6s in all experiments, we could track the same hydrogel along several days. Following our standard data analysis, the set of spike trains of the neurons at each layer were extracted from the fluorescence traces using the Schmitt trigger method. The layers were then combined to build the whole 3D population. Figure 7.4 shows the complete raster, on the same hydrogel, along four representative evolutionary stages. For this particular hydrogel we were capable of identifying 4 layers, which are marked for the measurement at DIV 13 with distinct colors.

As a general trend, our 3D primary cultures displayed dynamic patterns with much richer activity and variability with respect to their 2D counterparts. For 2D, we just remind that activity is characterized by an on/off behavior in which all neurons activate at once (network bursts) or remain silence, and with the bursts structured as high–speed ($20-50$ mm/s) circular waves. For 3D, we observed that the propagation waves was slower much slower ($1-10$ mm/s), and bursting events often did not include the whole population. Indeed, neuronal co-activation patterns in 3D changed from one day to another, combining episodes of strong synchronization (DIV 21 in Figure 7.4) with highly fragmented dynamics (DIV 19 and 27). Additionally, individual cells activations were abundant. These results obtained from calcium imaging at single–cell resolution coincide with experimental observations through electrophysiology (Frega et al., 2014) and reinforce the importance of properly characterize 3D neuronal activity *in vitro*.

Along development, neurons at first were characterized by sparse activations that later turned into a combination of eventual synchronous bursts with in–between periods of asynchronous activity. Full synchronization dominated at later stages (DIV 21) to, finally, by DIV 27, both the presence of synchronous events and overall activity substantially decayed possibly due to degradation. This general trend was similar across cultures. We note that the number of active cells progressively diminished along time (from about 600 to 120 in Figure 7.4), accentuating in the fourth week. The important fall of

active neurons confirms the degradation of the network. It is important to be aware that, although neurons seem quite active to the naked eye, activations in the background cause some false positive spikes in the recorded data.

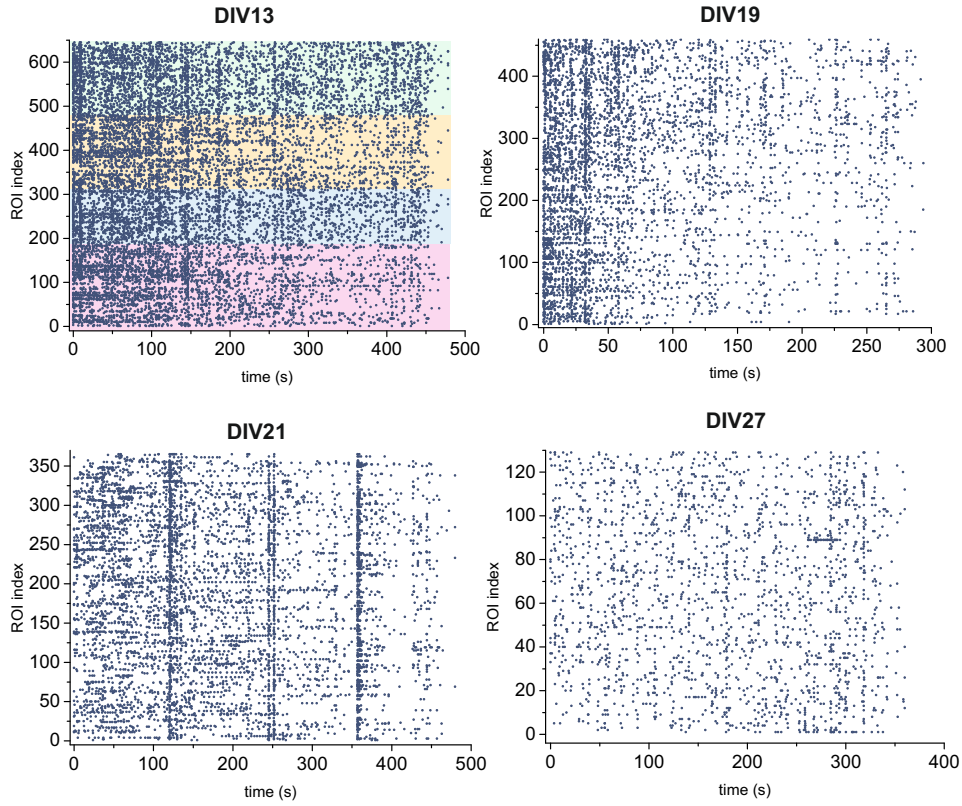


**Fig. 7.4 Evolution of activity history on 3D hydrogel cultures**. Four raster plots represent the activity history of the same hydrogel at different days. Before DIV13 most of the samples showed predominant random activations and extended periods of quiescence. When approaching the third week *in vitro*, spontaneous activity started to tune synchronous waves that included a large proportion of the neuronal population, as seen in this example at DIV13, DIV19 and DIV21. At the fourth week the cultures degraded and activity rates notably decreased, as seen at DIV27. Old samples with very low firing rates were discarded due to the lack of spike statistics. The panel at DIV13 shows the 4 layers of detected ROIs.

To quantify the degree of variability in the activity patterns we computed the dynamical richness $\Theta$ (Section 3.3.6). Conceptually, $\Theta = 0$ when all activations are coherent or neurons fire randomly, and $\Theta \to 1$ when neurons co–activate together in groups of maximal variation in size and timing. Figure 7.5A-C shows an example of the computation of $\Theta$ for the raster plot of Figure 7.4 at DIV 13. Panel A shows the matrix of cross-correlation values among firing neurons, and its corresponding normalized distribution is shown in panel B. The distribution is neither peaked towards 0 (random activity) nor 1 (full synchrony), indicating coordinated activity and of different patterns. Panel C shows the normalized distribution of sizes of 'global network activations' (GNA), i.e. the probability to observe a network co–activation of size $s$, with $s = 1$ corresponding to a network burst. The distribution shows a broad distribution of sizes, although full network activations are not still present. Using these data and the definition of $\Theta$ provided in Chapter 2 we measured a value of $\Theta \simeq 0.23$. This value is high compared to homogeneous 2D cultures, which show a permanent all–or–none behavior and typically provide $\Theta \lesssim 0.05$.

The evolution of $\Theta$ along development averaging for the 4 studied hydrogels is shown in Figure 7.5D. The dynamical richness at DIV9 is high ($\Theta = 0.3$) and reflect the presence of groups of firing neurons at different locations of the hydrogel. As the culture evolves and connections grow, more and more neurons participate in the same events. By DIV 13 full network burst started to appear, becoming dominant by DIV 19-21, leading to gradually smaller values of $\Theta$. For those cultures that remained healthy, we observed that clean, all–or–none activations occurred, and $\Theta$ reached similar values as 2D cultures.

We must emphasize that these results are still preliminary. Fluctuations among identically prepared cultures are noteworthy, and measurements with better sampling intervals (i.e. daily instead of weekly recordings) should be conducted. Also, enhancing the viability of hydrogel cultures up to $4-5$

weeks would enormously improve the quality of the data, and would help verifying the coexistence of synchronous and sparse activity for long periods of time. More experiments should also confirm whether activity in 3D cultures can be tuned and manipulated by using physical constraints, as part of MESOBRAIN project efforts to develop 3D tailored neuronal networks.

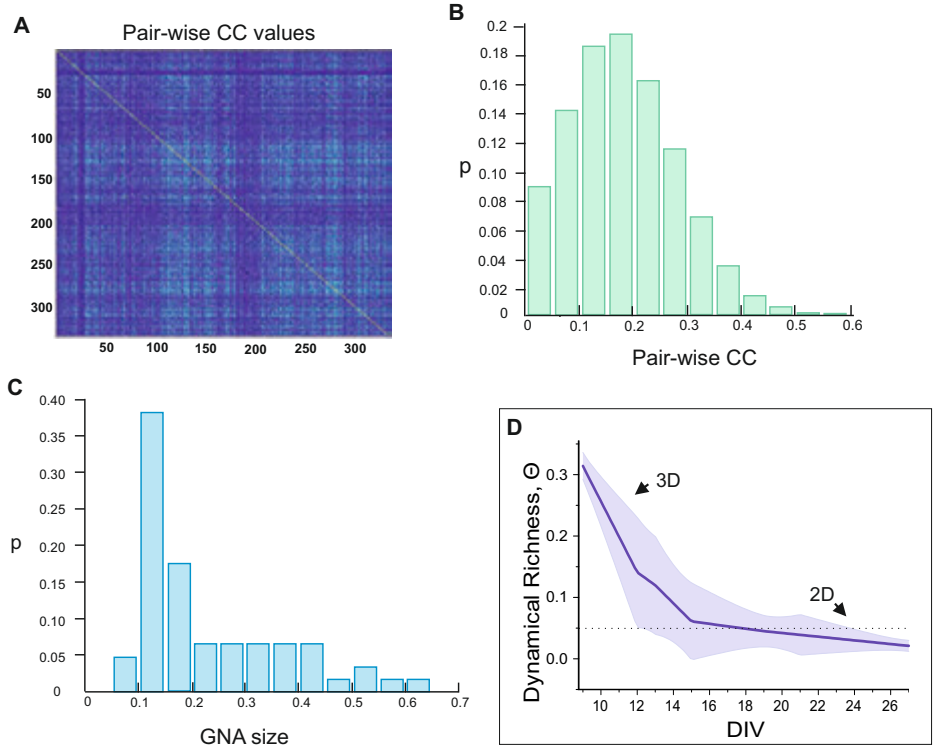


**Fig. 7.5 Dynamical richness in 3D hydrogel cultures** (**A–C**) For a culture at DIV 13, the panels show representative data for the cross-correlation (CC) matrix values among firing neurons, the normalized distribution of CC values, and the normalized distribution of co–activation sizes *s*. A rich system portrays both distributions broad. (**D**) Dynamical Richness Θ along developmental time *in vitro*. Each data point is an average over 4 hydrogels. Data is average among all experiments, starts at very high levels and decays during maturation. Θ is initially high and reduces as whole–network synchronous events emerge and become more important. The standard deviation (shaded area) is high and indicates notable variations between samples, worsened by the gradual decrease of active neurons with time.

As a final remark, we note that 3D primary cultures matured more slowly than 2D ones, with spontaneous activity emerging at DIV9 for 3D instead than at DIV5 for 2D. The functional development thus seems $3-7$ days shifted in time with respect to 2D cultures. 3D networks required a longer time to achieve equivalent firing rates and to reach neat synchronous bursting events.

### 7.3.3 Results: Network effective connectivity

We computed the effective connectivity matrices to get an insight on functional organization of the 3D networks. Effective connectivity was computed through GTE with a time binning of 50 ms. An example of the entire analysis process is shown in Figure 7.6. For clarity, we provide as example a mature hydrogel (DIV23) with neurons identified in 3 layers.

Figure 7.6A shows the raster plot of a 3–layer experiment that exhibited a particularly high synchronous behavior. The effective connectivity matrix derived from GTE is shown in Figure 7.6B. The matrix is ordered to highlight functional communities along the diagonal. Although some communities are visible at a quick glance, there are many connections linking them, indicating that the network is overall strongly connected. Indeed, modularity analysis software essentially portrayed 95% of the network as a single community. This strong cohesion is clear when representing the network in 3D (Figure 7.6C). In this figure, the spatial location of the neurons matches the experiment in $x-y$. The $z$ direction is approximate. Obviously, the neurons should cover the entire volume, but our 'focus plane approach' cannot fine tune the neuron–specific $z$ values. The interest of this 3D representation is that it shows how connections cross the entire system, although there is an abundance of connections linking neighboring layers that suggests strong local connectivity. The analysis also provided the average effective connectivity (mean degree) of the network. Results are shown in Figure 7.6D, compared with the average activity of the network, and grouped by week *in vitro*.

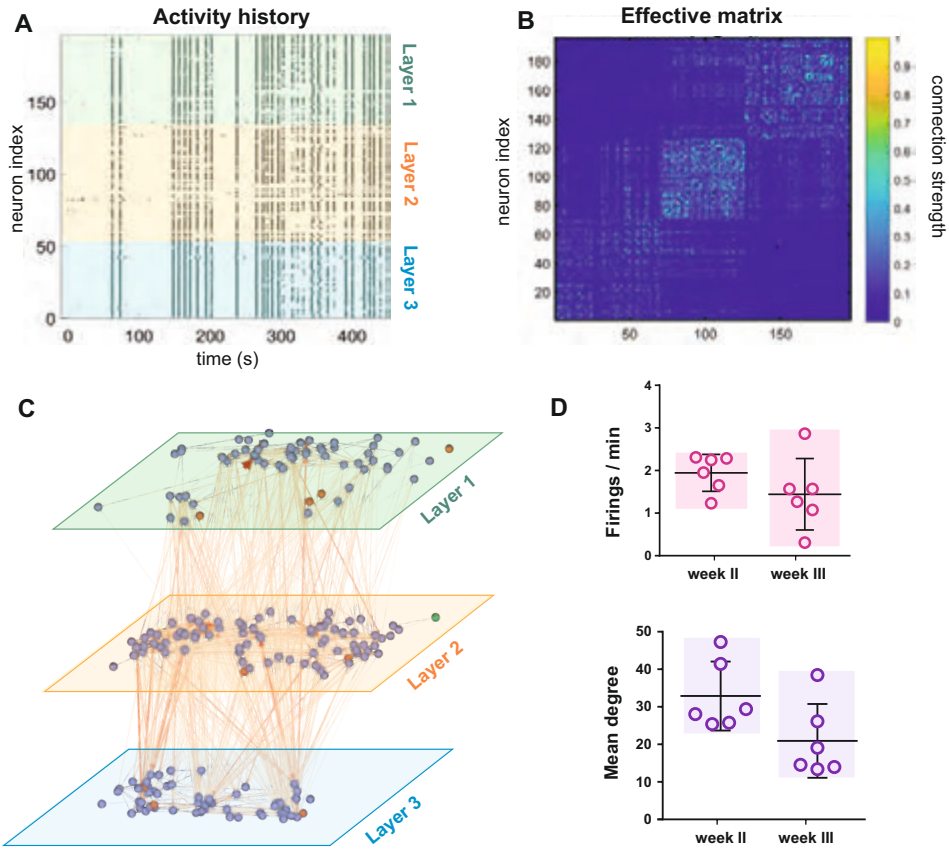


**Fig. 7.6 3D effective connectivity reconstruction pipeline.** (**A**) Raster plot of an experiment at DIV 23 in which neuronal activity was simultaneously recorded in 3 distinct layers while keeping the focus in the middle one. The total recordings lasted 10 minutes. Each layer is shaded with a different color. (**B**) Corresponding GTE–effective connectivity matrix with z–score $z = 1$, which captures interactions from both synchronous network bursts and individual firings. Functional modules can be observed by eye, but the network is highly connected. Modular analysis in MATLAB captured only 1 big functional modules and a number of weakly connected neurons. (**C**) Reconstructed network using Gephi and Corel Draw X6 programs. Nodes are colored according to their assigned module. For this particular experiment most of the neurons belong to same module (purple). (**D**) Network activity and mean neuronal degree for all data (4 hydrogels, 3 recordings each) grouped by week of development. Each circle is a recording.

Activity seems constant within experimental variability across weeks, but the tendency of the mean degree seems to decrease as maturation progresses, possibly indicating the formation of more and more functional communities and, therefore, a lower average connectivity per neuron.

To confirm the above results, from the inferred effective connectivity values we calculated the modularity statistic Q (Section 3.3.5). We computed two Q values, a first one corresponding to effective networks extracted with a z–score $z_1 = 1$ (termed Q1) and that includes both isolated neuronal activations and synchronous events, and a second one obtained with a z–score $z_2 = 2$ (termed Q2) and that includes only non–synchronous events.

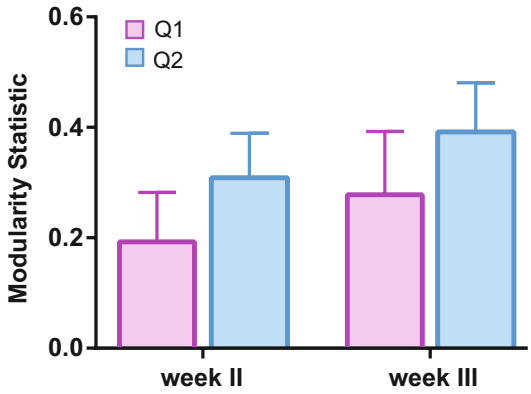


**Fig. 7.7 Modularity statistic in hydrogel cultures** Modularity statistic (Q) in hydrogel cultures increases from the second to the third week, and its also higher when taking into account only individual spikes (Q2) instead of considering both individual and collective activity (Q1).

The Q values in both cases are positive, indicating the presence of modularity traits. Average data, grouped by week of development, is shown in Figure 7.7. The observation that Q2 $\geq$ Q1 indicates that the firings outside bursting events portray the organization of the network in functional microcircuits that seem to increase in strength as the cultures mature. In other words, Q1 indicates those *integrated* activity episodes in which the entire network lights up, while Q2 indicates those *segregated* events in which small groups of

neurons preferentially communicate among themselves.The rise in modularity from the first to the second week, both for Q1 and Q2, may indicate that the cultures evolve towards a more spatially structured networks, although we do not have immunostainings or any other independent measurements to support this idea.

### 7.3.4 Computational simulations of 3D connectivity

Here we describe the basics of a 3D computational model developed in collaboration with Faci Lázaro and Dr. Jesús Gómez-Gardeñes (University of Zaragoza, Spain). We first simulated the random distribution of cells within the same cubic space but with two different densities, namely $\rho = 250$ neurons/$mm^3$ and $\rho = 500$ neurons/$mm^3$ (Figure 7.8). The positioning of the neurons was consistent with previous studies (Orlandi et al., 2013) but adjusted to volumes instead of square surfaces. Hence, the spatial distribution of neurons followed a three–dimensional probability density function, constructed through the summation of $n$ Gaussian functions with same deviation $\sigma = 300\ \mu m$ and random centers. The greatest the $n$, the more homogenous the distribution is. For the simulations we took $n = 10000$. Interestingly, the obtained networks qualitatively concurred with experimental data, and were able to predict that these densities are not enough to cause cell aggregation.

Based on these simulations, we questioned whether the variability of synchronization timing among samples (DIV21–27) and the slower maturation of 3D networks was a direct consequence of a wider spatial distribution rather than the effect of the ECM material in cell interactions and morphology. To clarify this aspect, we compared *in silico* the average connectivity $\langle k \rangle$ of 2D and 3D networks. We thus computed $\langle k \rangle$ as a function of the probability of connection $\alpha$ between two neurons (Figure 7.9). The model was able to ascribe differences in connectivity to the dimensional of the system. Simulations thus serve as a first approach towards understanding effective connectivity dissimilarities between *in vitro* and *in vivo* neuronal networks.

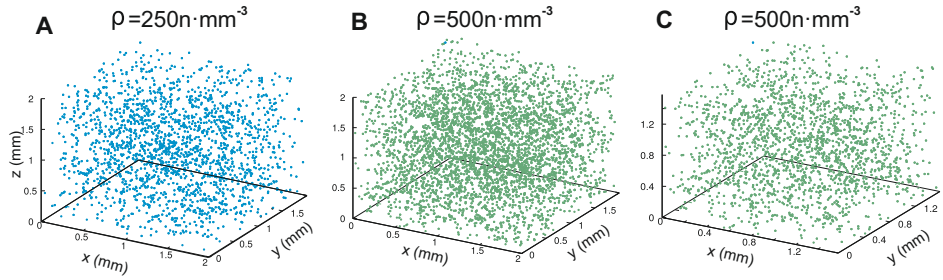


**Fig. 7.8 Cell distribution depending on density per** $mm^3$. Black dots represent neurons of 15 $\mu$m diameter, surrounded by colored circles for clear visualization. (**A**) Random distribution in a cubic space with density $\rho = 250$ neurons / $mm^3$ (**B**) Random distribution in a cubic space with density $\rho = 500$ neurons / $mm^3$ (**C**) This image shows the same density of cells as in figure (B) but taking only a fraction of the 3D culture that contains the same number of neurons as figure (A) to ease the comparison between both densities. These simulations were performed by Sergio Faci (Universidad de Zaragoza) and were edited with permission.

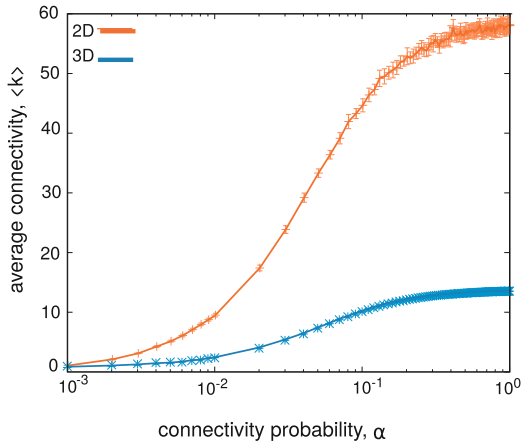


**Fig. 7.9 Average connectivity comparison.** The plot shows the dependence of the average connectivity, $\langle k \rangle$, on the connectivity probability between two neurons, $\alpha$, for 2D and 3D homogeneous cultures built with the model of (Orlandi et al., 2013), and adapted for 3D cultures. The dimensions of the cultures are: $2 \times 2$ mm$^2$ with 500 neurons for 2D cultures, and $2 \times 2 \times 2$ mm$^3$ with 2000 neurons for 3D cultures, such that the density in 3D is roughly twice the density in 2D. The data was then averaged over 50 network realizations. We note that, even at a maximum value of $\alpha = 1.0$, 3D cultures do not show any coherent activity, whereas the 2D cultures are fully synchronized at $\alpha = 0.1$. These simulations were performed by Sergio Faci (Universidad de Zaragoza) and were edited with permission.

## 7.4 Fast volume scanning of hydrogels

This section is centered on the experiments carried out at the Institute of Photonic Sciences (ICFO, Castelldefels), where we carried out dissections and measurements periodically.

Dr. Pablo Loza at ICFO was in charge of building the ligh–sheet microscope (LSM, Figures 7.10A–C) for the MESOBRAIN project (see Chapter 2.5.4). This microscope is capable of scanning the volume of a 3D culture sufficiently fast to capture the functional dynamics of the 3D network, while reducing the optical aberrations of out–of–focus neurons. For the first tests, the cultures were transported in a portable incubator from UB to ICFO. Later, to avoid cellular stress due to the transport itself, the cultures were prepared directly at ICFO's Biology Lab following our experimental procedure. For measurements, a hydrogel culture (DIV12) at a time was moved to a isolated petri dish and placed in the LSM setup over a warm metal platform at 37°C. One drop of media, Phenol–red free, was delivered to the top of the hydrogel and between the two water immersion objectives to maximize image quality.

### 7.4.1 Network reconstruction by sections

As described in Chapter 2.5.4, every volume was scanned at 132 fps, allowing the acquisition of 5 sections at 22 fps each. The small dimensions of the setup limited the scanning to an area of $1000 \times 800$ $\mu$m and a maximum depth of 300 $\mu$m. The system contained two orthogonal 10X lenses that could typically image $N = 80 \pm 20$ neurons in total. Neurons were functionally active, but we discarded all experiments with less than 60 active neurons and finally examined 7 samples at DIV12. The images of the scanned volumes consisted of BTF or TIF–array recordings with a duration of 10 minutes. Every recording was split into 5 individual files, one per section of the volume, and preprocessed independently (Figures 7.10D).

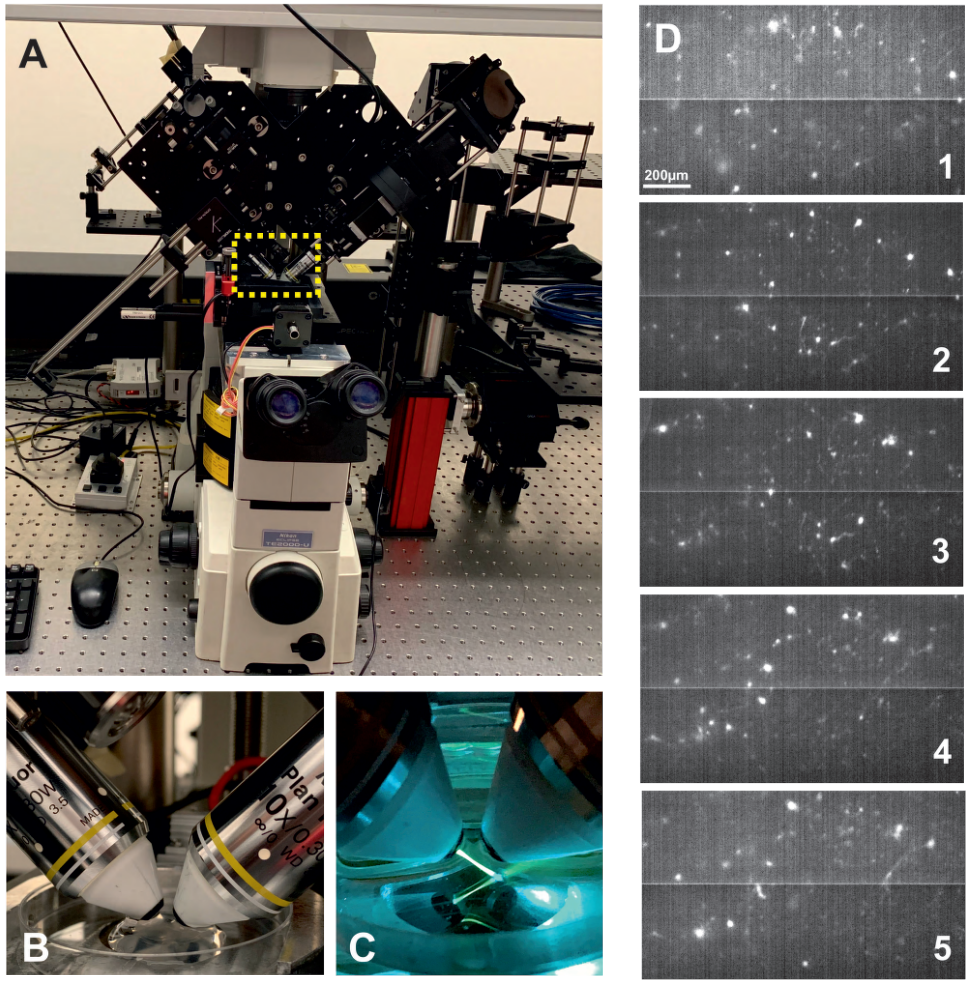


**Fig. 7.10 ICFO's light–sheet microscope setup** (**A**) Picture of the full setup. The dashed square marks the chamber where the culture sits, with temperature and $CO_2$ controlled by external devices. (**B**) Close–up of the orthogonal lenses upon a hydrogel sample. (**C**) All experiments were performed in total darkness. Here we show the illumination path of the light–sheet on water. (**D**) A set of 5 layers (projections of sub–volumes). Every image is the averaged grayscale obtained from all the frames in the recording. Images are obtained by combining two CMOS sensors, the difference in background intensity in each sensor of the camera that has to be adjusted during post–processing.

Every section corresponded with the z–projection of consecutive sub–volumes with depth $\approx 60\ \mu$m. Then, fluorescence traces and spike trains from all sections conforming the whole hydrogel were gathered and concatenated to extract the raster plot (Figure 7.11A) common network. Neuron indexes were adjusted so the first ROI was laid close to the surface and the last one was deposited at the deepest point.

We calculated the effective connectivity matrices using GTE, and again we took into consideration both a z–score $z_1 = 1$ to highlight whole–networks events or $z_2 = 2$ to highlight individual firings or small co–activations. Figure 7.11B shows the results of the analysis. The effective network with $z_2$ is on top; the network with $z_1$ is at the bottom. In this example it is much clearer the existence of small functional communities for $z_2$. The 3D visualization of the network is provided in Figure 7.11C. Thanks to LSM, here we were able to position precisely the neurons. However, the low quantity of cells fitting in the reduced field of view allowed by the LSM setup, and the decreased survival rate of the neurons, caused high variability in the results. Therefore, future work to optimize experimental conditions and the setup design are still needed to improve data acquisition.

## 7.5 Fast volume scanning of scaffolds

Here we just show some experiments performed with the same setup on PDMS patterns (Section 2.3.3) and scaffold structures (Section 2.3.2). Imaging these structures on a true 3D environment was the final goal of MESOBRAIN. In these very preliminary examples we could effectually image 2D networks with heterogeneity in $z$. Results are very promising and, most of all, shows the capacity of the LSM setup to image neurons with good quality.

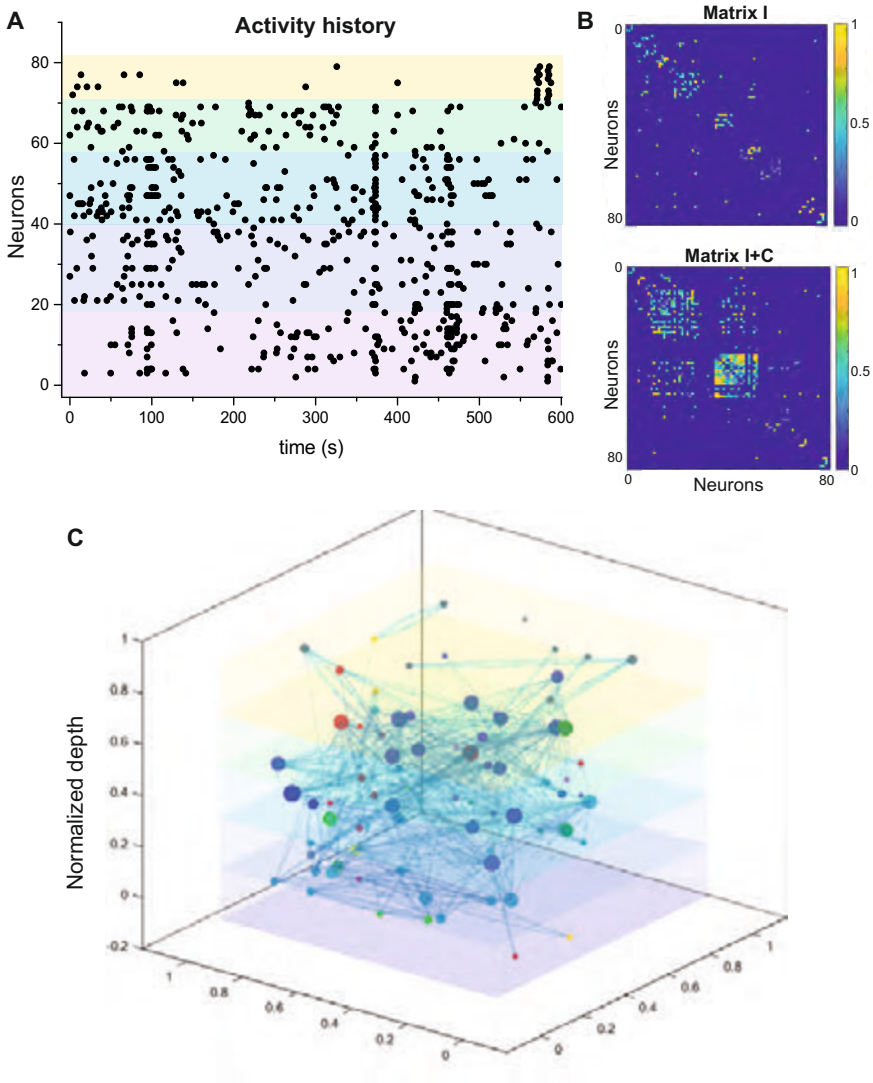


**Fig. 7.11 3D effective connectivity reconstruction with LSM.** (**A**) Raster plot built upon the simultaneous acquisition of 5 volumetric sections of the 3D network, along 10 min. Each section is shaded with a different color. (**B**) The inferred effective connectivity matrices either discarding collective bursting events and centering only on individual episodes (top, 'I' matrix) or including everything (bottom, 'I+C' matrix). (**C**) The graphical reconstruction of the matrix with neurons positioned in the center of their corresponding section ($z$-axis) and with precise $x - y$ matching. The size of the node is proportional to its degree of connectivity and the colors were assigned to different modules or communities.

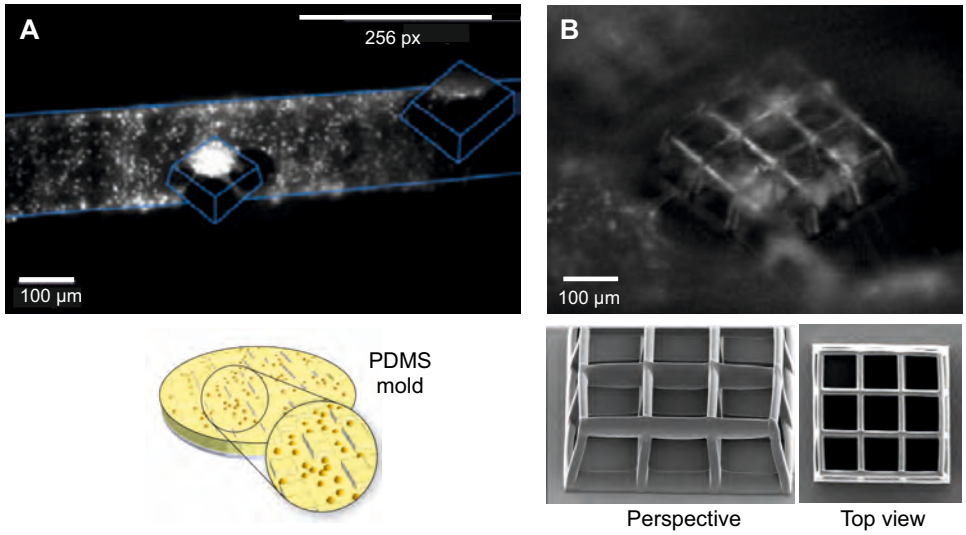


**Fig. 7.12 PDMS molds and scaffolds scanning with light–sheet microscopy.** (**A**) Top, PDMS mold. A unit obstacle (blue) is 70$\mu$ *m* high. Bright objects are neurons or neuronal aggregates. Bottom, sketch of the macroscopic structure of the culture. (**B**) Top, LSM image of single–structure scaffold based on two floor grid–like structure. Bottom, detail of the structures before plating. The laateral size of the unit mesh is 100 $\mu$m.

## 7.6 Discussion

Recent advances in reconstructing native tissue *in vitro* suggest that 3D cultures are more physiologically relevant than conventional 2D cultures regarding responses influenced by cell–cell and cell–ECM interactions. In the current study, we have observed substantial differences in terms of effective connectivity. 2D networks are typically characterized by simple on–off activation states with high participation, while the functional organization of the 3D networks displayed a combination of individual firings, modular activations and occasional synchronous bursts, that was reflected into greater maximized modularity and dynamical richness.

The capacity to evaluate patterns of neuronal activity rather than just firing rates, i.e. the presence or absence of activity and its frequency, offers the appealing opportunity to assess complex neuronal network interactions at the cellular level. Thus, the use of 3D cultures that mimic neuronal tissue are very promising for the study of neurodegenerative diseases, response to injury and homeostatic mechanisms (Tang-Schomer et al., 2014), as they recreate highly variable activity patterns intrinsic of *in vivo* networks. The incorporation of fluorescence imaging with non–toxic encoded indicators such as the GCaMP family, together with robust network analysis, aims to gain insight into the functional relevance of these patterns.

To date, the intricate relationship between all actors that shape the observable functional network remains a black box. This lack of information demands to continue the research in 2D cultures to understand basic concepts yet to be determined. Additionally, state–of–the–art imaging techniques have to be adapted to the new setups. Despite the exciting discoveries around tissue engineering and 3D cultures, much remains to be done both in the 2D and 3D environments.

# Chapter 8

# Conclusions

## 8.1 General conclusions

Here we summarize the general conclusions of this Thesis, listed in the same order as they have been presented in the previous chapters.

- **Resilience mechanisms in clustered cultures**

  Upon progressive connectivity blockade through CNQX, a receptor antagonist of AMPA–glutamate excitatory synapses, we observed in clustered neuronal networks that the global efficiency boosted for small degrees of blockade. This *hyper–efficiency* (HE) was certainly surprising and cannot be ascribed to simple, percolation-like degradation.

  Plasticity mechanisms influence the response of effective connectivity in the presence of perturbations. These compensatory mechanisms, usually disregarded in numerical models, must be included in biological modeling as accurately as possible. Otherwise, episodes of functional rewiring and synaptic strengthening could mask important phenomena during experiments that alter channel communication.

A simple numerical model that included *synaptic scaling*, an important plasticity mechanism, was able to capture the hyper–efficiency state seen in experimental data. Percolation models failed at capturing this phenomenon and just showed a progressive decay of the global efficiency. Despite the complex interplay between structure, function and plasticity in neuronal networks, relatively simple yet crucial adjustments can improve models considerably.

The effective connectivity achieved during several days in culture is not immediately recovered after a total blockade of neuronal communication through CNQX. Presumably, it will require several hours to develop similar levels of functionality even if there was no physical damage to the network. This hypothesis is a work in progress that cannot not be performed without GECIs.

- **MESOBRAIN: Engineered 3D neuronal cultures**

  D–Clear resulted a suitable biomaterial for the construction of scaffolds, both with primary rat cells and hiPSCs, due to its good optical properties, manageability and biocompatibility. To our knowledge, D–Clear was never used before outside the orthodontic field, and could provide a new catalog of interesting designs for support and guidance of neuronal assemblies.

  The design of tailored 3D neuronal networks on biocompatible structures, with conceptual relevance for the positioning of cell somas and guidance of axonal projections, is not a trivial task. Along MESOBRAIN, a large number of structures were proposed to build tailored 3D networks, but failed at confining neurons in preset locations. We concluded that the best approach was to set stackable 2D platforms. Each 2D platform would contain cortical neurons with specific traits, and supports between platforms would assist axonal pathfinding. This design also allowed the inclusion of multi–electrode arrays (MEAs) via

nano–electrodes to register electrical activity simultaneously. Despite of the engineering advances achieved, the construction of user–designed, reproducible 3D cortical network is still a goal in the far horizon.

- **Effective connectivity in 3D neuronal cultures**

  3D cultures in the form of cortical neurons embedded in PEGylated Fibrinogen hydrogels showed that the presence of an extracellular matrix notably conditioned network development. Cultures matured slowler in 3D than 2D by 3–4 days *in vitro*, displayed activity patterns much richer than their 2D equivalents and exhibited close similarities to spontaneous activity seen *in vivo*. Activity could be visualized using different techniques, namely wide–field fluorescence and light–sheet microscopy. The former allowed to access large fields of view and data could be acquired at high speed, rendering rich statistics of network characteristics and development. The latter was much better in terms of optical aberrations and 3D spatial localization of neurons, but could access a very small number of neurons. Both systems, thus, complemented to one another to investigate in detail 3D cultures.

  An *In silico* model show that connectivity is much smaller in 3D than in 2D, explaining the slower development of 3D cultures and their reduced capacity to show bursting behavior. Simulation offer interesting perspectives for the future, for instance to whether functional communities are much more structured and diverse in 3D than in 2D. They will also help framing the MESOBRAIN efforts from a numerical perspectives, by analyzing numerically the potential of obstacles to guide connections and, in turn, shape distinct activity patterns.

- **Effective development of hiPSC–derived neuronal networks**

  The functional maturation and the effective connectivity traits of human–derived neuronal networks could be quantified in detail, producing some

of the most documented iPSC–development data to date. The experimental challenges were high, since cells moved from day to day and therefore tracking the same cells in detail was very difficult. It was also hard from the experimentalist side since tracking and analyzing 8 different cultures along 60 days requires exquisite planning. The procured data, compared with 8 cultures from primary rat cultures, showed that iPSCs are functionally richer, and evolve towards a synchronous behavior more slowly, contrary to primary cultures that show synchrony since the very beginning. Our study offers an important reference point for the medical community. We studied healthy cell lines, but our study can be extended to diseased cells, thus quantifying the progress of the disease and, potentially, explore therapeutic treatments.

## 8.2 List of Publications

- E. Estevez-Priego et al. 2020. Effective connectivity network evolution in human–derived iPSCs cultures. *In preparation*.
- E. Estevez-Priego et al. 2020. Hyper–efficiency and synaptic scaling upon connectivity breakdown in neuronal cultures. *In preparation*.
- J. A Crowe et al. 2019. Development of two-photon polymerised scaffolds for optical interrogation and neurite guidance of human iPSC-derived cortical neuronal networks. *Under review.*
- A. Koroleva et al. 2020. In vitro development of iPSCs derived functional neuronal networks on laser fabricated 3D scaffolds. *In preparation.*
- S. Teller et al. 2019. Spontaneous functional recovery after focal damage in neuronal cultures. *Under review.*

# References


J. An, J. E. M. Teoh, R. Suntornnond, and C. K. Chua. Design and 3d printing of scaffolds and tissues. *Engineering*, 1 (2):261–268, 2015.

U. Aregueta Robles. Tissue engineered hydrogels supporting 3d neural networks. *Acta biomaterialia*, 2018.

J. Arulmoli, H. J. Wright, D. T. Phan, U. Sheth, R. A. Que, G. A. Botten, M. Keating, E. L. Botvinick, M. M. Pathak, T. I. Zarembinski, D. S. Yanni, O. V. Razorenova, C. C. Hughes, and L. A. Flanagan. Combination scaffolds of salmon fibrin, hyaluronic acid, and laminin for human neural stem cell and vascular tissue engineering. *Acta biomaterialia*, 43:122–138, 2016.

G. W. Ashley, J. Henise, R. O. Reid, and D. V. Santi. Hydrogel drug delivery system with predictable and tunable drug release and degradation rates. *Proceedings of the national academy of sciences of the United States of America*, 110 6:2318–23, 2013.

M. Aubry, S. Paris, S. W. Hasinoff, J. Kautz, and F. Durand. Fast local laplacian filters: theory and applications. *ACM transactions on graphics*, 33:167:1–167:14, 2014.

B. M. Baker and C. S. Chen. Deconstructing the third dimension: how 3d culture microenvironments alter cellular cues. *Journal of cell science*, 125 Pt 13:3015–24, 2012.

A.-L. Barabasi. Scale-free networks: A decade and beyond. *Science*, 325: 412–3, 2009.

A.-L. Barabasi and R. Albert. Emergence of scaling in random networks. *Science*, 286:509–12, 1999.

D. S. Bassett and O. Sporns. Network neuroscience. *Nature neuroscience*, 20:353–364, 2017.

J. Beggs and D. Plenz. Neuronal avalanches in neocortical circuits. *The Journal of Neuroscience*, 23:11167–11177, 2003.

A. Belle, H. Enright, A. Sales, K. Kulp, J. Osburn, E. Kuhn, F. Nicholas, and E. Wheeler. Evaluation of in vitro neuronal platforms as surrogates for in vivo whole brain systems. *Scientific Reports*, 8, 2018.

M. Bellin, M. Marchetto, F. Gage, and C. Mummery. Induced pluripotent stem cells: The new patient? *Nature reviews. Molecular cell biology*, 13: 713–26, 2012.

C. Bernard, E. Cherubini, R. Corradetti, and J.-L. Gaiarsa. Giant synaptic potentials in immature rat ca3 hippocampal-neurons. *The Journal of physiology*, 416:303–25, 1989.

M. J. Berridge, P. Lipp, and M. D. Bootman. The versatility and universality of calcium signalling. *Nature reviews molecular cell biology*, 1:11–21, 2000.

A. Björklund and O. Lindvall. Replacing dopamine neurons in parkinson's disease: How did it happen? *Journal of Parkinson's disease*, 2017.

A. Blankenship and M. Feller. Mechanisms underlying spontaneous patterned activity in developing neural circuits. *Nature reviews neuroscience*, 11: 18–29, 2009.

V. D. Blondel, J.-L. Guillaume, R. Lambiotte, and E. Lefebvre. Fast unfolding of communities in large networks. *Journal of statistical mechanics: Theory and experiment*, pages 1–12, 2008.

J. Borge-Holthoefer, Y. Moreno, and A. Arenas. Modeling abnormal priming in alzheimer's patients with a free association network. *PloS one*, 2011.

L. M. Brown. A survey of image registration techniques. *ACM Computing Surveys*, 24:325–376, 1992.

R. D. Burgoyne. Neuronal calcium sensor proteins: generating diversity in neuronal ca2+ signalling. *Nature reviews neuroscience*, 8:182–193, 2007.

S. R. Caliari and J. A. Burdick. A practical guide to hydrogels for cell culture. *Nature methods*, 13:405–414, 2016.

C. Cha, P. Soman, W. Zhu, M. Nikkhah, G. Camci-Unal, S. Chen, and A. Khademhosseini. Structural reinforcement of cell-laden hydrogels with microfabricated three dimensional scaffolds. *Biomaterials science*, 2 5: 703–709, 2014.

T.-W. Chen, T. J. Wardill, Y. Sun, S. R. Pulver, S. Renninger, A. Baohan, E. R. Schreiter, R. A. Kerr, M. B. Orger, V. Jayaraman, L. L. Looger, K. Svoboda, and D. S. Kim. Ultra-sensitive fluorescent proteins for imaging neuronal activity. *Nature*, 2013.

S. A. Cheraghi and U. U. Sheikh. Moving object detection using image registration for a moving camera platform. *2012 IEEE international conference on control system, computing and engineering*, pages 355–359, 2012.

D. T.-Y. Chiu, N. L. Jeon, S. Huang, R. S. Kane, C. J. Wargo, I. S. Choi, D. E. Ingber, and G. M. Whitesides. Patterned deposition of cells and proteins onto surfaces by using three-dimensional microfluidic systems. *Proceedings of the national academy of sciences of the United States of America*, 97 6:2408–13, 2000.

J. R. Cohen and M. D'Esposito. The segregation and integration of distinct brain networks and their relationship to cognition. *The Journal of neuroscience: the official journal of the Society for Neuroscience*, 36 48: 12083–12094, 2016.

A. M. Collins. Physical techniques. *Nanotechnology cookbook*, pages 205–253, 2012.

J. Cooper. Cell biology in neuroscience: Mechanisms of cell migration in the nervous system. *The Journal of cell biology*, 202:725–34, 2013.

R. Corlew, M. M. Bosma, and W. J. Moody. Spontaneous, synchronous electrical activity in neonatal mouse cortical neurones. *The journal of physiology*, 560 Pt 2:377–90, 2004.

R. Costa, B. E. P. Mizusaki, P. Sjöström, and M. van Rossum. Functional consequences of pre- and postsynaptic expression of synaptic plasticity. *Philosophical Transactions of the Royal Society B: Biological Sciences*, 372:20160153, 2017.

L. D'Aiuto, J. Naciri, N. Radio, S. Tekur, D. Clayton, G. Apodaca, R. Di Maio, Y. Zhi, P. Dimitrion, P. Piazza, M. Demers, J. Wood, C. Chu, J. Callio,

L. Mcclain, R. Yolken, J. Mcnulty, P. Kinchington, D. Bloom, and V. Nimgaonkar. Generation of three-dimensional human neuronal cultures: Application to modeling cns viral infections. *Stem Cell Research and Therapy*, 9, 2018.

L.-T. C. Dawson Ted M., Golde Todd E. Animal models of neurodegenerative diseases. *Nature neuroscience*, 21:1370–1379, 2018.

N. de Souza. Stem cells: Organoid variability examined. *Nature methods*, 14: 655–655, 2017.

G. Deco and V. K. Jirsa. Ongoing cortical activity at rest: criticality, multistability, and ghost attractors. *The Journal of neuroscience : the official journal of the Society for Neuroscience*, 32 10:3366–75, 2012.

G. Deco, V. K. Jirsa, P. A. Robinson, M. Breakspear, and K. J. Friston. The dynamic brain: From spiking neurons to neural masses and cortical fields. *PLoS Computational Biology*, 4:861–870, 2008.

G. Deco, V. K. Jirsa, and A. R. McIntosh. Emerging concepts for the dynamical organization of resting-state activity in the brain. *Nature reviews neuroscience*, 12:43–56, 2010.

G. Deco, G. Tononi, M. Boly, and M. Kringelbach. Rethinking segregation and integration: Contributions of whole-brain modelling. *Nature reviews neuroscience*, 16:430–9, 2015.

J. DeFelipe. The evolution of the brain, the human nature of cortical circuits, and intellectual creativity. *Frontiers in Neuroanatomy*, 5:29, 2011.

Y. Deitcher, G. Eyal, L. Kanari, M. B. Verhoog, G. A. A. Kahou, H. D. Mansvelder, C. P. J. de Kock, and I. Segev. Comprehensive morpho-electrotonic analysis shows 2 distinct classes of l2 and l3 pyramidal neurons in human temporal cortex. *Cerebral cortex*, 2017.

T. Deneux, A. Kaszas, G. Szalay, G. Katona, T. Lakner, A. Grinvald, B. J. Rózsa, and I. Vanzetta. Accurate spike estimation from noisy calcium signals for ultrafast three-dimensional imaging of large neuronal populations in vivo. *Nature communications*, 2016.

N. S. Desai, L. C. Rutherford, and G. G. Turrigiano. Plasticity in the intrinsic excitability of cortical pyramidal neurons. *Nature neuroscience*, 2:515–520, 1999.

A. di Domenico, G. Carola, C. Calatayud, M. Pons-Espinal, J. P. Muñoz, Y. Richaud-Patin, I. Fernandez-Carasa, M. Gut, A. Faella, J. Parameswaran, J. Soriano, I. Ferrer, E. S. Tolosa, A. Zorzano, A. M. Cuervo, A. Raya, and A. Consiglio. Patient-specific ipsc-derived astrocytes contribute to non-cell-autonomous neurodegeneration in parkinson's disease. *Stem cell reports*, 2019.

D. Dikovsky, H. Bianco-Peled, and D. Seliktar. The effect of structural alterations of peg-fibrinogen hydrogel scaffolds on 3-d cellular morphology and cellular migration. *Biomaterials*, 27 8:1496–506, 2006.

J. L. Drury and D. J. Mooney. Hydrogels for tissue engineering: scaffold design variables and applications. *Biomaterials*, 24 24:4337–51, 2003.

L. L. Dugan, V. M. Bruno, S. M. Amagasu, and R. G. Giffard. Glia modulate the response of murine cortical neurons to excitotoxicity: glia exacerbate ampa neurotoxicity. *The Journal of neuroscience: the official journal of the Society for Neuroscience*, 15 6:4545–55, 1995.

C. A. Durkee and A. Araque. Diversity and specificity of astrocyte–neuron communication. *Neuroscience*, 396:73–78, 2019.

A. E. F. Eltom, G. Zhong, and A. Muhammad. Scaffold techniques and designs in tissue engineering functions and purposes: A review. *Advances in Materials Science and Engineering*, 2019.

L. Eng, R. Ghirnikar, and Y. L. Lee. Glial fibrillary acidic protein: Gfap-thirty-one years (1969–2000). *Neurochemical research*, 25:1439–51, 2000.

I. Espuny-Camacho, K. A. Michelsen, D. Gall, D. Linaro, A. Hasche, J. Bonnefont, C. Bali, D. A. M. Orduz, A. Bilheu, A. Herpoel, N. Lambert, N. Gaspard, S. Péron, S. N. Schiffmann, M. Giugliano, A. Gaillard, and P. Vanderhaeghen. Pyramidal neurons derived from human pluripotent stem cells integrate efficiently into mouse brain circuits in vivo. *Neuron*, 77:440–456, 2013.

I. Espuny-Camacho, K. A. Michelsen, D. Linaro, A. Bilheu, S. Acosta-Verdugo, A. Herpoel, M. Giugliano, A. Gaillard, and P. Vanderhaeghen. Human pluripotent stem-cell-derived cortical neurons integrate functionally into the lesioned adult murine visual cortex in an area-specific way. *Cell reports*, 2018.

G. Eyal, M. B. Verhoog, G. Testa-Silva, Y. Deitcher, J. C. Lodder, R. Benavides-Piccione, J. I. Morales, J. DeFelipe, C. P. J. de Kock, H. D. Mansvelder, and I. Segev. Unique membrane properties and enhanced signal processing in human neocortical neurons. *eLife*, 2016.

M. fai Fong, J. P. Newman, S. M. Potter, and P. Wenner. Upward synaptic scaling is dependent on neurotransmission rather than spiking. *Nature communications*, 2015.

A. Fornito, A. Zalesky, and M. Breakspear. The connectomics of brain disorders. *Nature reviews neuroscience*, 16:159–172, 2015.

A. Fornito, A. Zalesky, and E. T. Bullmore. Fundamentals of brain network analysis. *Academic press*, pages 303–354, 2016.

S. Fortunato and M. Barthélémy. Resolution limit in community detection. *Proceedings of the national academy of sciences of the United States of America*, 104 1:36–41, 2007.

M. Fox and M. Greicius. Clinical applications of resting state functional connectivity. *Frontiers in systems neuroscience*, 4:19, 2010.

L. C. Freeman. Centrality in social networks conceptual clarification. *Social networks*, 1:215–239, 1978.

M. Frega, M. Tedesco, P. Massobrio, M. Pesce, and S. Martinoia. Network dynamics of 3d engineered neuronal cultures: A new experimental model for in-vitro electrophysiology. *Scientific reports*, 4:5489, 2014.

J. Friedrich, P. Zhou, and L. Paninski. Fast online deconvolution of calcium imaging data. *PLoS computational biology*, 13, 2017.

K. J. Friston. Functional and effective connectivity: A review. *Brain connectivity*, 1 1:13–36, 2011.

K. Ganguly, A. F. Schinder, S. T.-Y. Wong, and M.-M. Poo. Gaba itself promotes the developmental switch of neuronal gabaergic responses from excitation to inhibition. *Cell*, 105:521–532, 2001.

P. Gianfranco and M. V. Francesco. Pegylation of proteins as tailored chemistry for optimized bioconjugates. *Advances in polymer science*, 192: 95–134, 2005.

C. Gonzalez-Islas and P. Wenner. Spontaneous network activity in the embryonic spinal cord regulates ampaergic and gabaergic synaptic strength. *Neuron*, 49:563–575, 2006.

A. Gregor, E. Filova, M. Novak, J. Kronek, H. Chlup, M. Buzgo, V. Blahnova, V. Lukasova, M. Bartovs, A. Necas, and J. Hosek. Designing of pla scaffolds for bone tissue replacement fabricated by ordinary commercial 3d printer. *Journal of biological engineering*, 2017.

L. C. C. Greig, M. B. Woodworth, M. J. Galazo, H. Padmanabhan, and J. D. Macklis. Molecular logic of neocortical projection neuron specification, development and diversity. *Nature Reviews Neuroscience*, 14:755–769, 2013.

B. F. Grewe, D. Langer, H. Kasper, B. M. Kampa, and F. Helmchen. High-speed in vivo calcium imaging reveals neuronal network activity with near-millisecond precision. *Nature methods*, 7:399–405, 2010.

C. M. Grienberger and A. Konnerth. Imaging calcium in neurons. *Neuron*, 73:862–885, 2012.

L. G. Griffith and M. A. Swartz. Capturing complex 3d tissue physiology in vitro. *Nature reviews molecular cell biology*, 7:211–224, 2006.

A. Haimovici, E. Tagliazucchi, P. Balenzuela, and D. Chialvo. Brain organization into resting state networks emerges at criticality on a model of the human connectome. *Physical review letters*, 110:178101, 2013.

K. D. Harris, R. Q. Quiroga, J. Freeman, and S. L. Smith. Improving data quality in neuronal population recordings. *Nature neuroscience*, 19:1165–1174, 2016.

R. G. Harrison. The outgrowth of the nerve fiber as a mode of protoplasmic movement. *The Journal of experimental zoology*, 142:5–73, 1959.

F. M. Hayder Amin, D. D. P. Tonelli, and L. Berdondini. Developmental excitatory-to-inhibitory gaba-polarity switch is disrupted in 22q11.2 deletion syndrome: a potential target for clinical therapeutics. *Scientific reports*, 2017.

L. Hernández-Navarro, J. G. Orlandi, B. Cerruti, E. G. Vives, and J. Soriano. Dominance of metric correlations in two-dimensional neuronal cultures described through a random field ising model. *Physical review letters*, 118 (20):208101, 2017.

C. Honey, O. Sporns, L. Cammoun, X. Gigandet, J. Thiran, R. Meuli, and P. Hagmann. Predicting human resting-state functional connectivity. *Proc. Natl. Acad. Sci. U. S. A.*, 106:1–6, 2009.

P. D. Hsu, E. S. Lander, and F. Zhang. Development and applications of crispr-cas9 for genome engineering. *Cell*, 157:1262–1278, 2014.

D. Hutmacher, T. Schantz, I. Zein, K. Woei Ng, H. Teoh, and K.-C. Tan. Mechanical properties and cell cultural response of polycaprolactone scaffolds designed and fabricated via fused deposition modeling. *Journal of Biomedical Materials Research*, 55:203–216, 2001.

M. Ivenshitz and M. Segal. Neuronal density determines network connectivity and spontaneous activity in cultured hippocampus. *Journal of neurophysiology*, 104 2:1052–60, 2010.

J. G. Izant and J. R. McIntosh. Microtubule-associated proteins: a monoclonal antibody to map2 binds to differentiated neurons. *Proceedings of the national academy of sciences of the United States of America*, 77(8):4741–4745, 1980.

P. A. Janmey, J. P. Winer, and J. W. Weisel. Fibrin gels and their clinical and bioengineering applications. *Journal of the royal society interface*, 6 30: 1–10, 2008.

H. J.M. Introduction to biotechnical and biomedical applications of poly(ethylene glycol) (ch 1). *Poly(ethylene glycol) chemistry: biotechnical and biomedical applications*, pages 1–13, 1992.

B. Karrer, E. Levina, and M. Newman. Robustness of community structure in networks. *Physical review. E, Statistical, nonlinear, and soft matter physics*, 77 4 Pt 2:046119, 2008.

T. Keck, G. B. Keller, R. Jacobsen, U. T. Eysel, T. Bonhoeffer, and M. Hübener. Synaptic scaling and homeostatic plasticity in the mouse visual cortex in vivo. *Neuron*, 80:327–334, 2013.

S. Kim and J. Vellis. Stem cell-based cell therapy in neurological diseases: A review. *Journal of neuroscience research*, 87:2183–200, 2009.

P. Kirwan, B. Turner-Bridger, M. Peter, A. Momoh, D. Arambepola, H. P. C. Robinson, and F. Livesey. Development and function of human cerebral cortex neural networks from pluripotent stem cells in vitro. *Development*, 142, 2015.

D. Kleinfeld, K. H. Kahler, and P. E. Hockberger. Controlled outgrowth of dissociated neurons on patterned substrates. *The Journal of neuroscience: the official journal of the Society for Neuroscience*, 8 11:4098–120, 1988.

K. Ko and J. Frampton. Developments in 3d neural cell culture models: the future of neurotherapeutics testing? *Expert review of neurotherapeutics*, 16, 2016.

A. Koroleva, A. Gill, I. Ortega, J. Haycock, S. Schlie, S. Gittard, B. N Chichkov, and F. Claeyssens. Two-photon polymerization-generated and micromolding-replicated 3d scaffolds for peripheral neural tissue engineering applications. *Biofabrication*, 4:025005, 2012.

A. Koroleva, A. Deiwick, A. Nguyen, J. Narayan, A. Shpichka, O. Kufelt, R. Kiyan, V. Bagratashvili, P. Timashev, T. Scheper, and B. Chichkov. Hydrogel-based microfluidics for vascular tissue engineering. *Bionanomaterials*, 17, 2016.

J. Kuijlaars, T. Oyelami, A. Diels, J. Rohrbacher, S. Versweyveld, G. Meneghello, M. Tuefferd, P. Verstraelen, J. R. Detrez, M. Verschuuren, W. H. D. Vos, T. Meert, P. J. Peeters, M. Cik, R. Nuydens, B. Brône, and A. Verheyen. Sustained synchronized neuronal network activity in a human astrocyte co-culture system. *Scientific reports*, 2016.

S. Kullback and R. A. Leibler. On information and sufficiency. *The annals of mathematical statistics*, 22(1):79–86, 1951.

C. X. F. Lam, X. X. Mo, S. H. Teoh, and D. W. Hutmacher. Scaffold development using 3d printing with a starch-based polymer. *Materials science and engineering C*, 20:49–59, 2002.

R. S. Langer and J. P. Vacanti. Tissue engineering. *Science*, 260 5110:920–6, 1993.

R. Lanza, R. Langer, and J. P. Vacanti. Principles of tissue engineering. *Academic Press*, 2014.

V. Latora and M. Marchiori. Efficient behavior of small-world networks. *Physical review letters*, 87 19:198701, 2001.

X. Leinekugel, R. Khazipov, R. C. Cannon, H. Hirase, Y. Ben-Ari, and G. Buzsáki. Correlated bursts of activity in the neonatal hippocampus in vivo. *Science*, 296 5575:2049–52, 2002.

P. Lennie. The cost of cortical computation. *Current biology*, 13:493–497, 2003.

M.-C. Liao, C. R. Muratore, T. M. Gierahn, S. E. Sullivan, P. Srikanth, P. L. D. Jager, J. C. Love, and T. L. Young-Pearse. Single-cell detection of secreted a$\beta$ and sapp$\alpha$ from human ipsc-derived neurons and astrocytes. *The Journal of neuroscience : the official journal of the Society for Neuroscience*, 36(5):1730–46, 2016.

J. E. Lisman. Glutamatergic synapses are structurally and biochemically complex because of multiple plasticity processes: long-term potentiation, long-term depression, short-term potentiation and scaling. *Philosophical transactions of the Royal Society of London. Series B, Biological sciences*, 372 1715, 2017.

S. Lodato and P. Arlotta. Generating neuronal diversity in the mammalian cerebral cortex. *Annual review of cell and developmental biology*, 31: 699–720, 2015.

D. Lonardoni, H. Amin, S. D. Marco, A. Maccione, L. Berdondini, and T. Nieus. Recurrently connected and localized neuronal communities initiate coordinated spontaneous activity in neuronal networks. *PLoS Computational Biology*, 2017.

H. J. Luhmann, A. Sinning, J.-W. Yang, V. Reyes-Puerta, M. C. Stüttgen, S. Kirischuk, and W. Kilb. Spontaneous neuronal activity in developing neocortical networks: From single cells to large-scale interactions. *Frontiers in neural circuits*, 10:40, 2016.

M. P. Lutolf, J. L. Lauer-Fields, H. G. Schmoekel, A. T. Metters, F. E. Weber, G. B. Fields, and J. A. Hubbell. Synthetic matrix metalloproteinase-sensitive hydrogels for the conduction of tissue regeneration: Engineering cell-invasion characteristics. *Proceedings of the national academy of sciences*, 100(9):5413–5418, 2003.

M. Mandai, A. Watanabe, Y. Kurimoto, Y. Hirami, C. Morinaga, T. Daimon, M. Fujihara, H. Akimaru, N. Sakai, Y. Shibata, M. Terada, Y. Nomiya, S. Tanishima, M. Nakamura, H. Kamao, S. Sugita, A. Onishi, T. Ito, K. Fujita, and M. Takahashi. Autologous induced stem-cell–derived retinal cells for macular degeneration. *New England journal of medicine*, 376: 1038–1046, 2017.

E. Marder. Variability, compensation, and modulation in neurons and circuits. *Proceedings of the national academy of sciences of the United States of America*, 108 Suppl 3:15542–8, 2011.

A. L. K. Martin M. Riccomagno. Sculpting neural circuits by axon and dendrite pruning. *Annual review of cell and developmental biology*, 31: 779–805, 2015.

A. Mazzoni, F. Broccard, E. Garcia Perez, P. Bonifazi, M. Ruaro, and V. Torre. On the dynamics of the spontaneous activity in neuronal networks. *PloS one*, 2:e439, 2007.

V. Menon, T. F. Musial, A. Liu, Y. Katz, W. L. Kath, N. Spruston, and D. A. Nicholson. Balanced synaptic impact via distance-dependent synapse distribution and complementary expression of ampars and nmdars in hippocampal dendrites. *Neuron*, 80:1451–1463, 2013.

J. Mertens, A. C. M. Paquola, M. Ku, E. Hatch, L. Bohnke, S. Ladjevardi, S. McGrath, B. C. Campbell, H. Lee, J. Herdy, J. T. Gonçalves, T. Toda, Y. Kim, J. Winkler, J. Yao, M. W. Hetzer, and F. H. Gage. Directly reprogrammed human neurons retain aging-associated transcriptomic signatures and reveal age-related nucleocytoplasmic defects. *Cell stem cell*, 17 6: 705–718, 2015.

J. Mertens, M. C. Marchetto, C. Bardy, and F. H. Gage. Evaluating cell reprogramming, differentiation and conversion technologies in neuroscience. *Nature reviews neuroscience*, 17:424–437, 2016.

A. Messé, D. Rudrauf, H. Benali, and G. Marrelec. Relating structure and function in the human brain: Relative contributions of anatomy, stationary dynamics, and non-stationarities. *PLoS computational biology*, 10: e1003530, 2014.

D. Meunier, R. Lambiotte, and E. T. Bullmore. Modular and hierarchically modular organization of brain networks. *Frontiers in neuroscience*, 2010.

L. Millet and M. Gillette. Over a century of neuron culture: From the hanging drop to microfluidic devices. *The Yale journal of biology and medicine*, 85: 501–21, 2012.

V. B. Mountcastle. The columnar organization of the neocortex. *Brain: a journal of neurology*, 120:701–22, 1997.

S. Muldoon, P. Bonifazi, and R. Cossart. Dissecting functional connectivity of neuronal microcircuits: Experimental and theoretical insights. *Trends in neurosciences*, 34:225–36, 2011.

T. H. Murphy and D. Corbett. Plasticity during stroke recovery: from synapse to behaviour. *Nature reviews neuroscience*, 10:861–872, 2009.

D. A. Nicholson, R. E. Trana, Y. Katz, W. L. Kath, N. Spruston, and Y. Geinisman. Distance-dependent differences in synapse number and ampa receptor expression in hippocampal ca1 pyramidal neurons. *Neuron*, 50:431–442, 2006.

F. J. O'Brien. Biomaterials and scaffolds for tissue engineering. *Materialstoday*, 14 (3):88–95, 2011.

A. Odawara, Y. hei Saitoh, A. Alhebshi, M. Gotoh, and I. Suzuki. Long-term electrophysiological activity and pharmacological response of a human induced pluripotent stem cell-derived neuron and astrocyte co-culture. *Biochemical and biophysical research communications*, 443(4):1176–81, 2014.

S. Okujeni and U. Egert. Inhomogeneities in network structure and excitability govern initiation and propagation of spontaneous burst activity. *Frontiers in Neuroscience*, 13, 05 2019.

O. Olarte, J. Andilla, E. Gualda, and P. Loza-Alvarez. Light-sheet microscopy: A tutorial. *Advances in optics and photonics*, 10:111, 2018.

J. Orlandi, J. Soriano, E. Alvarez-Lacalle, S. Teller, and J. Casademunt. Noise focusing and the emergence of coherent activity in neuronal cultures. *Nature Physics*, Advance online publication, 2013.

J. G. Orlandi, O. Stetter, J. Soriano, T. Geisel, and D. Battaglia. Transfer entropy reconstruction and labeling of neuronal connections from simulated calcium imaging. *PloS one*, 2014.

A. M. Paşca, S. A. Sloan, L. E. Clarke, Y. Tian, C. D. Makinson, N. Huber, C. H. Kim, J. young Park, N. A. O'Rourke, K. D. Nguyen, S. J. Smith, J. R. Huguenard, D. H. Geschwind, B. A. Barres, and S. P. Pasca. Functional cortical neurons and astrocytes from human pluripotent stem cells in 3d culture. *Nature methods*, 12:671–678, 2015.

J. J. Palop and L. Mucke. Network abnormalities and interneuron dysfunction in alzheimer disease. *Nature Reviews Neuroscience*, 17:777–792, 2016.

G. Perea, M. Navarrete, and A. Araque. Tripartite synapses: astrocytes process and control synaptic information. *Trends in Neurosciences*, 32: 421–431, 2009.

A. S. D. Peter R. Huttenlocher. Regional differences in synaptogenesis in human cerebral cortex. *The Journal of comparative neurology*, 387 2: 167–78, 1997.

D. Poli, V. Pastore, and P. Massobrio. Functional connectivity in in vitro neuronal assemblies. *Frontiers in Neural Circuits*, 9, 2015.

J. Power, A. Cohen, S. Nelson, G. Wig, K. Barnes, J. Church, A. Vogel, T. Laumann, F. Miezin, B. Schlaggar, and S. Petersen. Functional network organization of the human brain. *Neuron*, 72:665–78, 2011.

M. L. Previtera, C. G. Langhammer, and B. L. Firestein. Effects of substrate stiffness and cell density on primary hippocampal cultures. *Journal of bioscience and bioengineering*, 110 4:459–70, 2010.

X. Qian, Q. Shen, S. K. Goderie, W. He, A. Capela, A. A. Davis, and S. Temple. Timing of cns cell generation a programmed sequence of neuron and glial cell production from isolated murine cortical stem cells. *Neuron*, 28:69–80, 2000.

G. Quadrato, T. Nguyen, E. Macosko, J. Sherwood, S. Min Yang, D. Berger, N. Maria, J. Scholvin, M. Goldman, J. Kinney, E. S. Boyden, J. Lichtman, Z. M. Williams, S. Mccarroll, and P. Arlotta. Cell diversity and network dynamics in photosensitive human brain organoids. *Nature*, 545, 2017.

R. Radakisnin, M. Abdul Majid, and N. Mohd nor. Biodegradable poly(lactic acid) scaffold for tissue engineering: A brief review. *Journal of polymer science and technology*, 1, 2015.

S. Ramon y Cajal. Comparative study of the sensory areas of the human cortex. *Book*, page 325, 1899.

M. J. Roberts, M. D. Bentley, and J. M. Harris. Chemistry for peptide and protein pegylation. *Advanced drug delivery reviews*, 54 4:459–76, 2002.

J. Rolston, D. Wagenaar, and S. Potter. Precisely timed spatiotemporal patterns of neural activity in dissociated cortical cultures. *Neuroscience*, 148:294–303, 09 2007.

T. Rose, P. M. Goltstein, R. Portugues, and O. Griesbeck. Putting a finishing touch on gecis. *Frontiers in molecular neuroscience.*, 7:88, 2014.

M. Rubinov and O. Sporns. Complex network measures of brain connectivity: Uses and interpretations. *NeuroImage*, 52:1059–1069, 2010.

C. S. von Bartheld, J. Bahney, and S. Herculano-Houzel. The search for true numbers of neurons and glial cells in the human brain: A review of 150 years of cell counting. *The journal of comparative neurology*, 524: 3865–3895, 2016.

K. Schaukowitch, A. L. Reese, S.-K. Kim, G. K. Kilaru, J.-Y. Joo, E. T. Kavalali, and T. Kim. An intrinsic transcriptional program underlying synaptic scaling during activity suppression. *Cell reports*, 18 6:1512–1526, 2017.

T. Schreiber. Measuring information transfer. *Physical review letters*, 85 2: 461–4, 2000.

M. S. Schröter, O. Paulsen, and E. T. Bullmore. Micro-connectomics: probing the organization of neuronal networks at the cellular scale. *Nature reviews neuroscience*, 18:131–146, 2017.

W. W. Seeley, R. K. Crawford, J. Zhou, B. L. Miller, and M. D. Greicius. Neurodegenerative diseases target large-scale human brain networks. *Neuron*, 62:42–52, 2009.

R. Segev, M. Benveniste, Y. Shapira, and E. Ben-Jacob. Formation of electrically active clusterized neural networks. *Physical review letters*, 90(16): 168101, 2003.

B. D. Semple, K. Blomgren, K. Gimlin, D. M. Ferriero, and L. J. Noble-Haeusslein. Brain development in rodents and humans: Identifying benchmarks of maturation and vulnerability to injury across species. *Progress in Neurobiology*, 106–107:1–16, 2013.

C. E. Shannon. A mathematical theory of communication. *The bell system technical journal*, 27(3):379–423, 1948.

C. J. Shatz. Impulse activity and the patterning of connections during cns development. *Neuron*, 5(6):745–756, 1990.

L. Sheintuch, A. Rubin, N. Brande-Eilat, N. Geva, N. Sadeh, O. Pinchasof, and Y. Ziv. Tracking the same neurons across multiple days in ca2+ imaging data. *Cell reports*, 21:1102–1115, 2017.

Y. Shi, P. Kirwan, J. C. Smith, H. P. C. Robinson, and F. J. Livesey. Human cerebral cortex development from pluripotent stem cells to functional excitatory synapses. *Nature neuroscience*, 15:477–486, 2012.

Y. Shi, H. Inoue, J. C. Wu, and S. Yamanaka. Induced pluripotent stem cell technology: a decade of progress. *Nature reviews drug discovery*, 16: 115–130, 2017.

T. P. Silva, J. P. Cotovio, E. P. Bekman, M. Carmo-Fonseca, J. M. S. Cabral, and T. M. G. Fernandes. Design principles for pluripotent stem cell-derived organoid engineering. *Stem cells international*, 2019.

L. Sima, E. Buruiana, T. Buruiana, A. Matei, G. Epurescu, M. Zamfirescu, A. Moldovan, S. Petrescu, and M. Dinescu. Dermal cells distribution on laser-structured ormosils. *Journal of tissue engineering and regenerative medicine*, 7, 2013.

D. Smetters, A. Majewska, and R. Yuste. Detecting action potentials in neuronal populations with calcium imaging. *Methods*, 18 2:215–21, 1999.

F. Song, X. Li, Q. Wang, L. Liao, and C. Zhang. Nanocomposite hydrogels and their applications in drug delivery and tissue engineering. *Journal of biomedical nanotechnology*, 11 1:40–52, 2015.

J. Soriano, M. Rodríguez Martínez, T. Tlusty, and E. Moses. Development of input connections in neural cultures. *Proceedings of the National Academy of Sciences*, 105(37):13758–13763, 2008.

O. Sporns. The non-random brain: Efficiency, economy, and complex dynamics. *Frontiers in computational neuroscience*, 5:5, 2011.

O. Sporns. Network attributes for segregation and integration in the human brain. *Current opinion in neurobiology*, 23:162–171, 2013.

O. Sporns and R. Betzel. Modular brain networks. *Annual review of psychology*, 67, 2015.

O. Sporns, C. Honey, and R. Kötter. Identification and classification of hubs in brain networks. *PloS one*, 2:e1049, 2007.

O. Stetter, D. Battaglia, J. Soriano, and T. Geisel. Model-free reconstruction of excitatory neuronal connectivity from calcium imaging signals. *PLoS computational biology*, 8(8):e1002653, 2012.

Y. Sun, B. Danila, K. Josić, and K. E. Bassler. Improved community structure detection using a modified fine tuning strategy. *Europhysics letters*, 86 (2): 28004, 2009.

Y. Sun, Z. Huang, W. Liu, K. Yang, K. Sun, S. Xing, D. Wang, W. Zhang, and X. Jiang. Surface coating as a key parameter in engineering neuronal network structures in vitro. *Biointerphases*, 7:1–14, 2012.

K. Takahashi and S. Yamanaka. Induction of pluripotent stem cells from mouse embryonic and adult fibroblast cultures by defined factors. *Cell*, 126:663–76, 2006.

K. Takahashi, K. Tanabe, M. Ohnuki, M. Narita, T. Ichisaka, K. Tomoda, and S. Yamanaka. Induction of pluripotent stem cells from adult human fibroblasts by defined factors. *Cell*, 131:861–72, 2007.

J. Y. Tan, C. K. Chua, and K. F. Leong. Fabrication of channeled scaffolds with ordered array of micro-pores through microsphere leaching and indirect rapid prototyping technique. *Biomedical Microdevices*, 15:83–96, 2013.

M. D. Tang-Schomer, J. D. L. White, L. W. Tien, L. I. Schmitt, T. M. Valentin, D. J. Graziano, A. M. Hopkins, F. G. Omenetto, P. G. Haydon, and D. L. Kaplan. Bioengineered functional brain-like cortical tissue. *Proceedings of the national academy of sciences of the United States of America*, 111 38:13811–6, 2014.

J. Tatarishvili, K. Oki, E. Monni, P. Koch, T. Memanishvili, A.-M. Buga, V. Verma, A. Popa-Wagner, O. Bruestle, O. Lindvall, and Z. Kokaia. Human induced pluripotent stem cells improve recovery in stroke-injured aged rats. *Restorative neurology and neuroscience*, 32 4:547–58, 2014.

V. Telezhkin, C. Schnell, P. L. Yarova, S. K. Yung, E. L. Cope, A. C. Hughes, B. A. N. Thompson, P. J. Sanders, C. Geater, J. M. Hancock, S. Joy, L. Badder, N. Connor-Robson, A. Comella, M. Straccia, G. Bombau, J. T. Brown, J. M. Canals, A. D. Randall, N. D. Allen, and P. J. Kemp. Forced cell cycle exit and modulation of gabaa, creb, and gsk3b signaling promote functional maturation of induced pluripotent stem cell-derived neurons. *American journal of physiology. Cell physiology*, 310 7:C520–41, 2016.

S. Teller, C. Granell, M. De Domenico, J. Soriano, S. Gómez, and A. Arenas. Emergence of assortative mixing between clusters of cultured neurons. *PLoS computational biology*, 10(9):e1003796, 2014.

S. Teller, I. B. Tahirbegi, M. Mir, J. Samitier, and J. Soriano. Magnetite-amyloid-$\beta$ deteriorates activity and functional organization in an in vitro model for alzheimer's disease. *Scientific reports*, 2015.

E. Tibau, M. Valencia, and J. Soriano. Identification of neuronal network properties from the spectral analysis of calcium imaging signals in neuronal cultures. *Front. Neural Circuits*, 2013.

E. Tibau Martorell, A. Alexander Ludl, S. Rudiger, J. Orlandi, and J. Soriano. Neuronal spatial arrangement shapes effective connectivity traits of in vitro cortical networks. *IEEE Transactions on Network Science and Engineering*, PP:1–1, 2018.

D. Tornero, S. Wattananit, M. G. Madsen, P. Koch, J. Wood, J. Tatarishvili, Y. Mine, R. Ge, E. Monni, K. Devaraju, R. F. Hevner, O. Bruestle, O. Lindvall, and Z. Kokaia. Human induced pluripotent stem cell-derived cortical neurons integrate in stroke-injured cortex and improve functional recovery. *Brain : a journal of neurology*, 136 Pt 12:3561–77, 2013.

D. Tornero, O. Tsupykov, M. Granmo, C. Rodriguez, M. Grønning-Hansen, J. Thelin, E. Smozhanik, C. Laterza, S. Wattananit, R. Ge, J. Tatarishvili, S. Grealish, O. Brü, G. Skibo, M. Parmar, J. Schouenborg, O. Lindvall, and Z. Kokaia. Synaptic inputs from stroke-injured brain to grafted human stem cell-derived neurons activated by sensory stimuli. *Brain: a journal of neurology*, 140, 2017.

N. Tritsch, A. Granger, and B. L Sabatini. Mechanisms and functions of gaba co-release. *Nature reviews. Neuroscience*, 17, 2016.

A. Trounson and N. D. DeWitt. Pluripotent stem cells progressing to the clinic. *Nature Reviews Molecular Cell Biology*, 17:194–200, 2016.

G. G. Turrigiano. The self-tuning neuron: Synaptic scaling of excitatory synapses. *Cell*, 135:422–435, 2008.

M. van den Heuvel and O. Sporns. Network hubs in the human brain. *Trends in cognitive sciences*, 17:683–696, 2013.

R. Vicente, M. Wibral, M. Lindner, and G. Pipa. Transfer entropy—a model-free measure of effective connectivity for the neurosciences. *Journal of computational neuroscience*, 30:45–67, 2011.

S. Wang, S. Guan, W. Li, D. Ge, J. Xu, C. Sun, T. Liu, and X. Ma. 3d culture of neural stem cells within conductive pedot layer-assembled chitosan/gelatin scaffolds for neural tissue engineering. *Materials science and engineering: C*, 93, 2018.

D. J. Watts and S. H. Strogatz. Collective dynamics of 'small-world' networks. *Nature*, 393:440–442, 1998.

J. Weisel and R. Litvinov. Mechanisms of fibrin polymerization and clinical implications. *Blood*, 121, 2013.

M. Wernig, J.-P. Zhao, J. Pruszak, E. Hedlund, D. Fu, F. Soldner, V. Broccoli, M. Constantine-Paton, O. Isacson, and R. Jaenisch. Neurons derived from reprogrammed fibroblasts functionally integrate into the fetal brain and improve symptoms of rats with parkinson's disease. *Proceedings of the national academy of sciences*, 105:5856–5861, 2008.

B. Wheeler and G. Brewer. Designing neural networks in culture. *Proceedings of the IEEE. Institute of electrical and electronics engineers*, 98:398–406, 2010.

J. S. Wiegert, M. Mahn, M. Prigge, Y. Printz, and O. Yizhar. Silencing neurons: Tools, applications, and experimental constraints. *Neuron*, 95: 504–529, 2017.

J. Y. Wu, X. Huang, and C. Zhang. Propagating waves of activity in the neocortex: what they are, what they do. *The Neuroscientist: a review journal bringing neurobiology, neurology and psychiatry*, 14 5:487–502, 2008.

H. Yamamoto, S. Moriya, K. Ide, T. Hayakawa, H. Akima, S. Sato, S. Kubota, T. Tanii, M. Niwano, S. Teller, J. Soriano, and A. Hirano-Iwata. Impact of modular organization on dynamical richness in cortical networks. *Science advances*, 2018.

Y. Yang, N. Liu, Y. He, Y. Liu, L. H. Ge, L. Zou, S. Song, W. Xiong, and X. Liu. Improved calcium sensor gcamp-x overcomes the calcium channel perturbations induced by the calmodulin in gcamp. *Nature communications*, 2018.

Y. Yi, J. Park, J. Lim, C. Lee, and S.-H. Lee. Central nervous system and its disease models on a chip. *Trends in biotechnology*, 33 12:762–776, 2015.

X. Yin, J. chong Xu, G. sik Cho, C. Kwon, T. M. Dawson, and V. L. Dawson. Neurons derived from human induced pluripotent stem cells integrate into rat brain circuits and maintain both excitatory and inhibitory synaptic activities. *eNeuro*, 2019.

F. Zenke, E. J. Agnes, and W. Gerstner. Diverse synaptic plasticity mechanisms orchestrated to form and retrieve memories in spiking neural networks. *Nature communications*, 2015.

B. Zitova and J. Flusser. Image registration methods: a survey. *Image vision computing.*, 21:977–1000, 2003.